Angewandte Chemie
Eine Zeitschrift der Gesellschaft Deutscher Chemiker

Supporting Information

Catalytic Oxygenation of Hydrocarbons by Mono-μ-oxo Dicopper(II) Species Resulting from O−O Cleavage of Tetranuclear Cu^{I}/Cu^{II} Peroxo Complexes

Ramona Jurgeleit, Benjamin Grimm-Lebsanft, Benedikt Maria Flöser, Melissa Teubner, Sören Buchenau, Laura Senft, Jonas Hoffmann, Maria Naumova, Christian Näther, Ivana Ivanović-Burmazović, Michael Rübhausen, and Felix Tuczek**

anie_202101035_sm_miscellaneous_information.pdf

SUPPORTING INFORMATION

Table of Contents

1. Instrumentation and Physical Methods

1.1. General Information

Procedures employing oxygen- and/or moisture-sensitive materials were performed with anhydrous solvents (vide infra) and using standard Schlenk techniques (atmosphere of dinitrogen or argon) and a glovebox (O_2 < 1 ppm and H_2O < 1 ppm) filled with dinitrogen atmosphere. The solvents were dried (THF, $C_2H_5OC_2H_5$ using sodium; C_3H_6O with Drierite^{TM}; CH_3CN with CaH_2) and freshly distilled under argon or N_2 prior to use. Anhydrous deuterated solvents were freeze-pump-thaw degassed and dried over 3 Å molecular sieves. Chemicals and solvents were purchased from Sigma-Aldrich, Merck, abcr, Deutero and Fisher Scientific in reagent grade. Unless otherwise noted, commercially available reagents were used without further purification.

Flash Column chromatography was carried out by using an Isolera One Spectra by co. Biotage with UV detector (λ = 200-400 nm) and prepacked SNAP Ultra cartridges (different size). R_f-values were determined by thin-layer chromatography on Polygram Sil G/UV254 (Macherey-Nagel, 0.2 mm particle size) with a UV lamp (λ = 254 nm) by co. Camag. The elemental analyses were performed using a Vario MICRO cube element analyzer by co. Elementar; the samples were prepared in tin vessels were burnt in a stream of oxygen. NMR spectra were recorded at 300 K using a Bruker DRX 500 (^{1}H NMR (500.1 MHz), ^{13}C NMR (125.8 MHz)) and a Bruker AVANCE III HD Pulse Fourier Transform spectrometer operating at frequencies of 400.13 MHz (^{1}H NMR), 100.62 MHz (^{13}C NMR) with TMS as internal standard. Infrared spectra were recorded on a Bruker ALPHA FT-IR Spectrum with a Platinum ATR setup. UV/Vis measurements of the reactivity studies were done by means of an Agilent 8453 spectrometer, using a quartz cell with length l = 1 cm or l = 1 mm. Low Temperature UV/Vis spectroscopy were recorded in acetone on an Agilent Cary 5000 spectral photometer using a CryoVac KONTI cryostat using a quartz cell with length l = 1 cm. The temperature is varied and controlled with the CryoVac temperature measurement control unit TIC304-MA (enables gas flow control of the liquid nitrogen in combination with the CryoVac L-2033 gas lances).

1.2. Single-Crystal Structure analysis of compound 1 and 2

Data collection was performed using an IPDS-2 from Stoe & Cie using Mo-Kα radiation (λ = 0.71073 Å). The structure was solved with SHELXT[1] and structure refinement was performed against F^2 using SHELXL-2018.[2] For both compounds a numerical absorption correction was performed using X-Red and X-Shape of the software package X-Area.[3] Most non-hydrogen atoms were refined with anisotropic displacement parameters. The C-H hydrogen atoms were positioned with idealized geometry and were refined isotropically with U_{iso} (H) = 1.2 U_{eq} (C). The asymmetric unit of **compound 1** contains an additional dichloromethane solvate molecule in a general position, which is disordered in two orientations and its position is not fully occupied. Therefore, it was refined using a split model with restraints (SAME).

The asymmetric unit of **compound 2** contains a trinuclear Cu complex with two crystallographically independent Cu cations, of which one is located on a center of inversion. The asymmetric unit additionally contains two triflate anions and two acetone solvate molecules in general positions. Both triflate anions are disordered in two orientations and were refined using a split model with restraints (SAME, SIMU and DELU) and the S atoms refined anisotropic and the C, F and O atoms refined isotropic. The position of the acetone solvate molecules are not fully occupied, which is in agreement with the observation that the crystals of **compound 2** immediately start to decompose already at room temperature, which is also observed for the crystals of **compound 1**.

Selected crystal data are given in Table S1, ORTEP plots can be found in Figure S1 and S2, selected bond lengths and angles are given in Table S2 and additional drawings for **compound 2** are presented in Figure S3. CCDC-1998203 (**compound 1**) and CCDC-1998204 (**compound 2**), contain the supplementary crystallographic data for this paper. These data can be obtained free of charge from the Cambridge Crystallographic Data Centre via http://www.ccdc.cam.ac.uk/data_request/cif.

Table S1: Selected crystal data and results of the structure refinements for **compound 1** and **2**.

Compound	**1**	**2**
Sum formula	$C_{31.72}H_{25.44}Cl_{3.44}N_6$	$C_{78.20}H_{70.40}Cu_3F_{12}N_{14}O_{15.40}S_4$
Molecular weight/g mol^{-1}	612.61	1999.54
Crystal system	monoclinic	monoclinic
Space group	*C*2/*c*	$P2_1/n$
a / Å	16.9161(5)	14.8752(3)
b / Å	8.3174(3)	21.0553(4)
c / Å	22.0251(6)	15.7216(3)
α / °	90	90
β / °	105.931(2)	117.319(2)
γ / °	90	90
V / Å^3	2979.87(16)	4374.83(16)
T / K	170	200 (2)
Z	4	2
D_{calc}/g cm^{-3}	1.366	1.518
μ / mm^{-1}	0.380	0.915
T_{min}, T_{max}	0.8609, 0.9673	0.8175, 0.9147
Crystal size / mm	0.08 x 0.14 x 0.25	0.15 x 0.12 x 0.07
Absorption correction	numerical	numerical
θ_{max} / °	27.0	27.0
Refl. collected	16796	47897
Unique refl.	3217	9484
R_{int}	0.0191	0.0263
Refl. [$F_o > 4\sigma(F_o)$]	2768	8114
parameters	219	628
$R_1[F_o > 4\sigma(F_o)]$	0.0540	0.0758
wR_2 (for all data)	0.1520	0.2371
GOF	1.044	1.070
$\Delta\rho_{max}$, $\Delta\rho_{min}$ / eÅ^{-3}	0.656, -0.312	0.820, -0.625

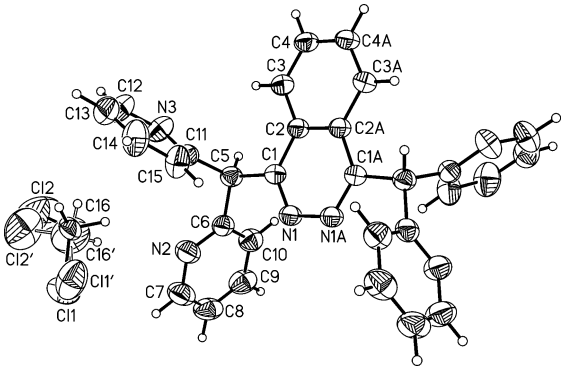

Figure S1: View of the asymmetric unit of **compound 1** with labeling and displacement ellipsoids drawn at the 50 % probability level.

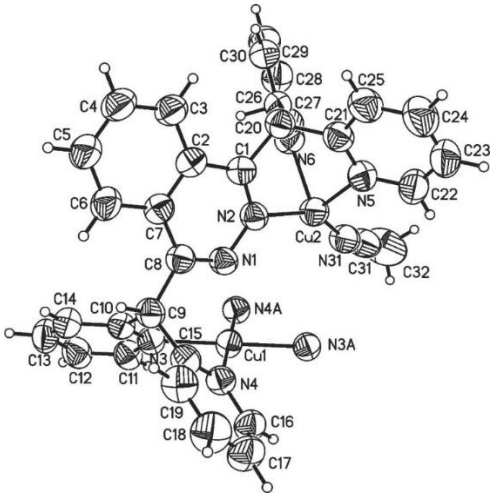

Figure S2: View of a part of the asymmetric unit of **compound 2** with labeling and displacement ellipsoids drawn at the 50 % probability level. The triflate anions and the acetone solvate molecules are omitted for clarity.

Table S2: Selected bond lengths (Å) and angles (°) of **compound 2**. Symmetry transformations used to generate equivalent atoms: A: -x+3,-y+1,-z+3.

Cu(1)-N(4A)	2.007(3)	Cu(1)-N(3)	2.020(3)
Cu(1)-N(4)	2.007(3)	Cu(1)-N(3A)	2.020(3)
Cu(1)-N(1)	2.491(3)	Cu(1)-N(1A)	2.491(3)
N(4A)-Cu(1)-N(4)	180.00(16)	N(4A)-Cu(1)-N(3A)	86.93(12)
N(4A)-Cu(1)-N(3)	93.07(12)	N(4)-Cu(1)-N(3A)	93.07(12)
N(4)-Cu(1)-N(3)	86.93(12)	N(3)-Cu(1)-N(3A)	180.00(10)
N(1)-Cu(1)-N(4)	83.36(12)	N(1)-Cu(1)-N(4A)	96.64(12)
N(1)-Cu(1)-N(1A)	180.00(16)	N(1)-Cu(1)-N(3)	85.95(11)
N(1)-Cu(1)-N(3A)	94.05(11)	N(1A)-Cu(1)-N(3)	94.05(11)
N(1A)-Cu(1)-N(3A)	85.95(11)	N(1A)-Cu(1)-N(4)	96.64(12)
N(1A)-Cu(1)-N(4A)	83.36(12)		
Cu(2)-N(31)	1.895(3)	Cu(2)-N(5)	2.073(4)
Cu(2)-N(2)	2.039(3)	Cu(2)-N(6)	2.121(3)
N(31)-Cu(2)-N(2)	147.86(14)	N(31)-Cu(2)-N(6)	103.15(15)
N(31)-Cu(2)-N(5)	118.08(15)	N(2)-Cu(2)-N(6)	91.46(12)
N(2)-Cu(2)-N(5)	89.99(13)	N(5)-Cu(2)-N(6)	89.86(13)

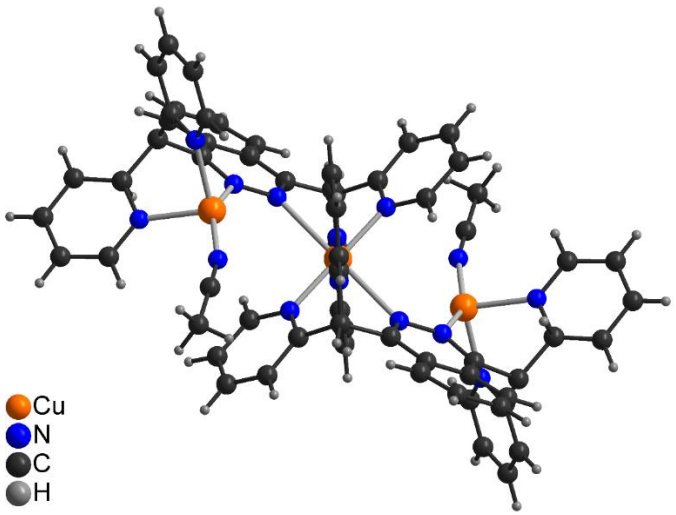

Figure S3: View of the trinuclear complex in the crystal structure of **compound 2**.

1.3. Resonance Raman Spectroscopy

Raman measurements were performed with the custom-built UT-3 Raman spectrometer,[4] combined with a frequency doubled Ti:sapphire laser (Tsunami model 3960C-15HP, Spectra Physics Lasers Inc.) to obtain an excitation wavelength of 397 nm with a pulse width of 1.8 ps. The cryostat was described previously[5] using a 1.4 mL screw cap Suprasil cuvette with septum (117104F-10-40, Hellma Analytics) for oxygenation and now equipped with a Peltier element (QC-127-1.4-6.0MS, QuickCool) and a cooling copper block which encloses three sides of the cuvette. The laser beam was widened with a spatial filter and then focused on the cuvette inside the cryostat. The focus spot size was 20 µm in diameter. With a micrometer screw, the focus was positioned 30 µm inside the cuvette. Raman scattered light was captured with the entrance optics of the UT-3 triple monochromator spectrometer.

The precursor with a concentration of 12.5 mM in acetone was cooled in the cuvette cryostat to below -90 °C. Dioxygen was added via a cannula through the septum (0.02 bar overpressure for 15 min) and a distinct color change from yellow to green was observed. For the nitrous oxide measurements the gas was added for 30 min with a comparable flow. Temperature of the solution inside the cuvette was measured with a Pt100 sensor. For the measurements above 193 K the temperature of the ethanol bath was increased and the cooling power of the Peltier element adjusted accordingly, to reach the respective temperatures. The used laser power in front of the entrance optics was between 10 to 15 mW and data was accumulated up to 900 s.

1.4. Cryo-UHR-ESI Mass Spectrometry

Cryospray-ionization mass spectrometry (CSI-MS) measurements were performed on an UHR-TOF Bruker Daltonik maXis plus, an ESI-quadrupole time-of-flight (qToF) mass spectrometer capable of a resolution of at least 60000 (FWHM), which was coupled to a Bruker Daltonik Cryospray unit.

Detection was in positive ion mode, the source voltage was 3.5 kV. The flow rates were 240 µL/hour. The drying gas (N_2), to achieve solvent removal, was held at -40 °C (or at -90 °C) and the spray gas was held at -35 °C (or at -90 °C).

The machine was calibrated prior to every experiment via direct infusion of Agilent ESI-TOF low concentration tuning mixture, which provided an *m/z* range of singly charged peaks up to 2700 Da in both ion modes.

Analyzing of the measured spectra was performed with Bruker Compass DataAnalysis 4.2.

General sample preparation for CSI-MS:

In a nitrogen atmosphere glove box Cu(I) complex (5 mg) was dissolved in dry acetone (1.5 mL). The complex solution was cooled to -35 °C (or to -90 °C).

Oxygenation of Cu(I) complexes:

The cooled Cu(I) solutions were bubbled with excess $^{16}O_2$ (or with $^{18}O_2$). After bubbling, the samples were diluted with cooled (-35 °C or -90 °C) dry acetone and then directly injected into the mass spectrometer.

Reaction of Cu(I) complexes with iodosobenzene:

In a nitrogen atmosphere glovebox iodosobenzene (50 mg) was suspended in dry acetone (3 mL). The suspension was supersonicated for better solving of iodosobenzene. Iodosobenzene solution (500 µL) was added to the cooled Cu(I) solutions. The reaction solutions were constantly held at -35 °C (or at -90 °C) for 2 h of reaction time, diluted with cooled, dry acetone and then injected into the mass spectrometer.

1.5. X-ray Absorption Spectroscopy (XAS)

Experimental:

Cu K-edge XAS spectra were measured at beamline P65 of the PETRA III synchrotron light source at Deutsches Elektronen Synchrotron (DESY) in Hamburg.[6] A Si(111) double-crystal monochromator was used for energy selection. Data were measured in fluorescence mode using a Passivated Implanted Planar Silicon (PIPS) detector. The measurement time for a complete scan from -150 eV to 1000 eV around the Cu K-edge was 300 s. Several scans were collected to increase the signal to noise ratio. In total, one sample was measured for up to 120 min. Copper foil was measured concomitantly and the first inflection point energy set to 8979.0 eV. All measurements were calibrated to this value accordingly.

The precursors of **1a**-PF_6 and **1b**-PF_6 were prepared under inert conditions (oxygen and water free) and transferred to a custom-made PEEK cuvette with septum and Kapton® windows, which were sealed by a Teflon O-ring. The cuvette was then cooled in liquid nitrogen. Afterwards the solution was warmed up slightly above the freezing point, $^{16}O_2$ was added for 5 min. The cuvette was frozen in liquid nitrogen again to prevent the solution from warming up. The oxygenation cycle was performed three times to form the complex. The cuvette was frozen directly after the final oxygenation cycle in liquid nitrogen again and subsequently transferred to a continuous flow helium cryostat Optistat CF (Oxford Instruments, UK) which was kept at 100 K. For the 243 K measurements the solution was warmed up to 243 K in the cryo, kept for one hour to let the complex form and cooled down, well below the freezing point, to 100 K again, to avoid sample damage.

Data reduction and Analysis:

Data analysis was performed using Demeter software package (Athena and Artemis).[7] χ(k) was extracted using a standard procedure in Athena. Fitting was done for k-range of 3-12 1/Å and R-range of 1-3.2/3.4 Å in R-space. DFT-calculated structures were used as structural models for the fit. Scattering paths were calculated using Feff6. All significant scattering paths up to a distance of 3.2 Å for the **Cu_2O** species and 3.4 Å for the **Cu_2O_4** species were included in the model.

1.6. GC-MS

GC-MS investigations were performed on an Agilent 7890B GC System with an Agilent 5977A MSD mass spectrometer. As column we used a HP-5M5 5 % phenyl-methyl-silox (29.5 m x 250 µm x 0.25 µm). The inlet temperature was 250 °C at 9.3 psi. We used a temperature program which started with keeping the temperature at 45 °C for 30 s, heated to 175 °C in a course of 3 min and maintained at 250 °C for 27 min (9.3 psi, 1.2 mL/min). As internal standard we used mesitylene (t_R = 3.08 min).

1.7. HR-EI Mass Spectrometry

HR-EI MS investigations were performed on an AccuTOF™ GCv 4G time-of-flight mass spectrometer from JOEL capable of a resolution of 80000. The source operated in the positive ion mode (EI+); a potential of 70 V was applied (to accelerate electrons to a kinetic energy of 70 eV to produce positive ions). The samples were measured in solid form or dissolved in dichloromethane and directly injected.

1.8. Computational Details

All calculations were performed with ORCA 4.1.1.[8] For geometry optimizations and frequency calculations the PBE[9] functional and the def2-SVP[10] basis set were used in conjunctions with D3BJ[11] dispersion correction and the RI[12] approximation with the appropriate fitting basis set.[13] None of the optimized geometries showed imaginary frequencies.

UV/Vis spectra were simulated with TDDFT using the B3LYP[14] functional, the def2-TZVP(-f)[10] basis set, the CPCM[15] continuum solvation model with the appropriate setting for the respective solvent and the RIJCOSX[16] approximation for calculation speedup. Furthermore, tight integration grids were used (grid6 and gridX6 in ORCA nomenclature). For mononuclear and binuclear complexes 60 and 80 roots were requested, respectively.

Single point energies were computed with the same method as the TDDFT calculations but with a larger def2-TZVP basis set.

All systems with two unpaired electrons were treated with the broken symmetry approach.

2. Experimental Procedures

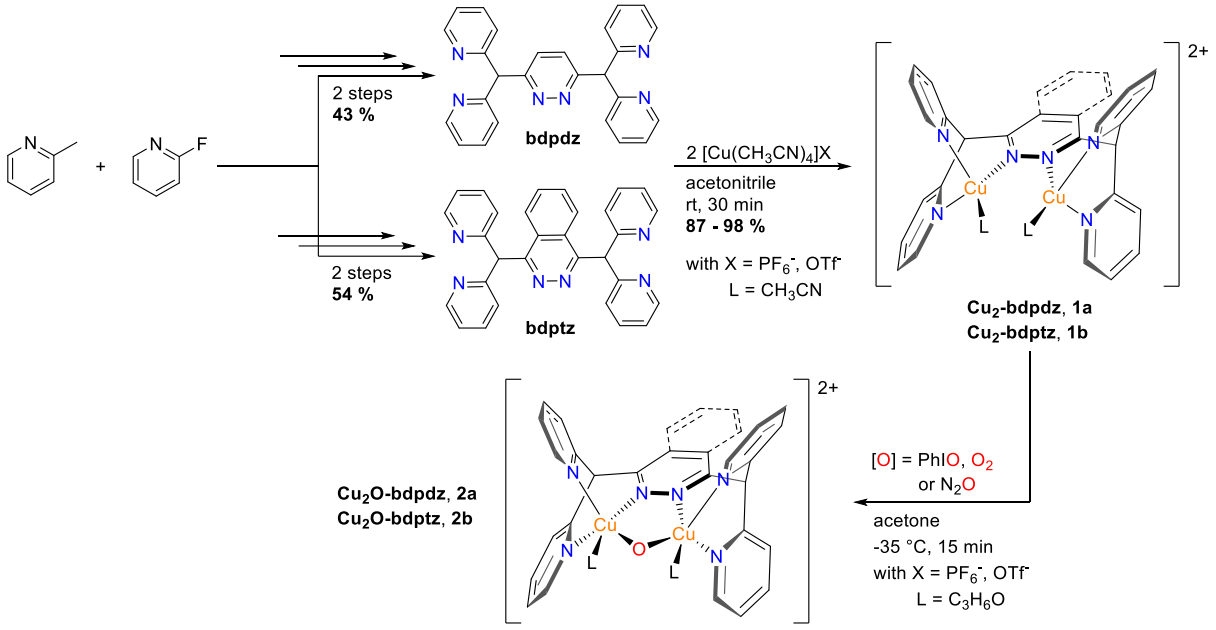

Scheme S1: Access to the Cu_2O complexes. Overview of the synthetic route to the model systems **2a** and **2b**. Preparation of the precursor complexes **1a** and **1b** and formation of the corresponding **Cu_2O** complexes **2a** and **2b**. The counterions X are hexafluorophosphate (PF_6^-) or triflate (OTf^-) and are omitted for clarity. The coordinating solvent molecules in the solid form of the precursors are acetonitrile ligands, denoted with L. In the acetone solution, the CH_3CN coligands are replaced by acetone after addition of [O]. The yields for **bdpdz** and **bdptz** are overall yields after two steps.

2.1. Choice of model systems

The diazine (=N-N=) moiety of pyrazoles, 1,2,4-triazoles, pyridazines and phthalazines is able to act as a useful scaffold to enforce the bridging of two metal ions in close proximity to each other (about 3.5-4.5 Å).[17] The rigid spacer/backbone enforces a pre-orientation of two copper centers and – in combination with the *N*-donor atoms of the ligand side arms – forms two binding pockets. The hexadentate *N*-donor ligands **bdpdz**[18] and **bdptz**[19] comply with these considerations. In order to check whether dicopper complexes supported by these ligands are also able to form the **Cu_2O** motif DFT calculations were performed. In fact, optimized geometries with reasonable structural parameters could be obtained (see Section S9), encouraging us to employ these ligands for our investigations.

2.2. Preparation of the precursor and Cu_2O complexes: General remarks

The multidentate *N*-donor ligands **bdpdz**[18] and **bdptz**[19] were synthesized by slight modifications of the published procedures (see below). Addition of two equiv. of tetrakis(acetonitrile)copper(I)-hexafluorophosphate ($[Cu(CH_3CN)_4]PF_6$) or -triflate ($[Cu(CH_3CN)_4]OTf$) to a solution of **bdpdz** or **bdptz** in acetonitrile provided the dinuclear copper(I) complexes of **bdpdz** (= **1a**) and **bdptz** (= **1b**) in excellent yields (87-98 %).[20] **1a** and **1b** show distinct sensitivity against moisture and dioxygen. Slow evaporation of an acetone solution of **1b**-OTf yielded red crystals suitable for investigation by single-crystal X-ray diffraction analysis (see below). The obtained molecular structure reveals a trinuclear mixed-valent $Cu^ICu^{II}Cu^I$-complex demonstrating the ability of the used ligand system to stabilize both oxidation states, copper(I) and copper(II) (vide infra). This was of particular importance in the investigations presented in this study.

2.3. Preparation of starting materials

2,2′-dipyridylmethane[21] was prepared by published procedure and characterized by use of ^{1}H- and ^{13}C-NMR spectroscopy and HR-ESI mass spectrometry. A modification of the literature procedure was used to purify the crude product. Instead of bulb-to-bulb distillation, column chromatography on silica gel (TLC (ethyl acetate): R_f = 0.12) was applied to yield the desired product as a slightly yellow oil (5.46 g, 32.1 mmol, 80 %). ^{1}H NMR (500 MHz, $CDCl_3$, 300 K): δ = 8.55 (ddd, J = 4.9 Hz, J = 1.8 Hz, J = 0.9 Hz, 2H, Py-CH), 7.60 (td, J = 7.7 Hz, J = 1.9 Hz, 2H, Py-CH), 7.26 (d, J = 7.8 Hz, 2H, Py-CH), 7.12 (ddd, J = 7.5 Hz, J = 4.9 Hz, J = 1.2 Hz, 2H, Py-CH), 4.34 (s, 2H, CH_2) ppm; ^{13}C NMR (126 MHz, CDCl3, 300 K): δ = 159.59 (Py-CH), 149.60 (Py-CH), 136.74 (Py-CH), 123.73 Py-CH), 121.62 (Py-CH), 47.45 (CH_2) ppm; MS (ESI): m/z (%): 171.09 (100 [*M*+H]$^+$). HRMS (ESI) *m/z* calcd. for $C_{11}H_{11}N_2$: 171.09167 [*M*+H]$^+$; found: 171.09171.

All other starting materials (3,6-dichloropyridazine and 1,4-dichlorophthalazine) were obtained from commercial sources and used as received without further purifications.

2.4. Preparation of bdpdz[18]

The ligand **bdpdz** was synthesized according to literature.[18] The published procedure was slightly modified.

To a solution of 2.00 g (11.8 mmol) 2,2′-dipyridylmethane in 50 mL diethyl ether were slowly added 4.8 mL (12.0 mmol) of a 2.5 M *n*-butyllithium solution in *n*-hexane at -15 °C within 15 min. A suspension of 869 mg (5.88 mmol) 3,6-dichloropyridazine in 40 mL diethyl ether was added to the dark orange solution at -15 °C. After complete addition, the reaction mixture was warmed up to reach room temperature within 90 min. To eliminate excess of *n*-butyllithium, 6 mL water was added to the slightly brown reaction mixture and stirred for 1 h. The solid was filtered off, washed with cold diethyl ether and with a hot ethanol-diethyl ether solution (50:50 v/v). After the suspension was stirred for 30 min at 55 °C, the off-white solid was filtered off and dried under reduced pressure to obtain 1.33 g (3.20 mmol, 54 %) of the ligand 3,6-bis(2,2′-dipyridylmethyl)-pyridazine **bdpdz**.

^{1}H NMR (500 MHz, $CDCl_3$, 300 K): δ = 8.55 (ddd, J = 4.9 Hz, J = 1.8 Hz, J = 0.9 Hz, 4H, Py-CH), 7.68 (s, 2H, Pydz-CH), 7.62 (dt, J = 7.7 Hz, J = 1.9 Hz, 4H, Py-CH), 7.37 (d, J = 7.9 Hz, 4H, Py-CH), 7.14 (ddd, J = 7.5 Hz, J = 4.9 Hz, J = 1.2 Hz, 4H, Py-CH), 6.18 (s, 2H, CH) ppm; ^{13}C NMR (126 MHz, $CDCl_3$, 300 K): δ = 161.9 (Pydz-C_q), 160.2 (Py-C_q), 149.7 (Py-CH), 136.8 (Py-CH), 128.0 (Pydz-CH), 124.4 (Py-CH), 122.1 (Py-CH), 62.0 (CH) ppm; IR (neat): $\tilde{\nu}$ = 3046 (w), 3005 (w), 2940 (w), 1584 (m), 1567 (w), 1549 (w), 1467 (m), 1431 (s), 1150 (w), 1050 (m), 993 (m), 768 (m), 751 (s), 675 (m), 654 (m), 616 (m) cm^{-1}; HRMS (ESI) *m/z* calcd. for $C_{26}H_{21}N_6$: 417.1822 [*M*+H]$^+$; found: 417.1818; HRMS (EI) *m/z* calcd. for $C_{26}H_{20}N_6$: 416.17494 [*M*]$^{+\cdot}$; found: 416.17490; Elemental analysis calcd. for $C_{26}H_{20}N_6$: C 74.98, H 4.84, N 20.18, found: C 74.68, H 4.85, N 19.97.

2.5. Synthesis of bdptz[19]

The ligand **bdptz** was synthesized by slight modifications of the published procedure.[19]

To a solution of 2.09 g (12.3 mmol) 2,2′-dipyridylmethane in 30 mL tetrahydrofuran were slowly added 4.97 mL (12.4 mmol) of a 2.5 M *n*-butyllithium solution in *n*-hexane at -78 °C. The orange solution was stirred for 15 min followed by the addition of 1.22 g (6.15 mmol) 1,4-dichlorophthalazine and 60 mL tetrahydrofuran at -78 °C within 10 min. After complete addition, the reaction mixture was warmed up to reach room temperature within 2 h. To eliminate excess of *n*-butyllithium, 10 mL water was added to the slightly brown reaction mixture. The solvents were removed under reduced pressure and the resulting crude product was washed with a hot ethanol-diethyl ether solution (50:50 v/v). After the suspension was stirred for 30 min at 55 °C, the white solid was filtered off and dried under reduced pressure to obtain 1.96 g (4.18 mmol, 68 %) of the ligand 1,4-bis(2,2′-dipyridylmethyl)-phthalazine **bdptz**.

^{1}H NMR (500 MHz, $CDCl_3$, 300 K): δ = 8.54 (ddd, J = 4.9 Hz, J = 1.8 Hz, J = 0.9 Hz, 4H, Py-CH), 8.22 (dd, J = 6.4, J = 3.3 Hz, 2H, Phthz-CH), 7.71 (dd, J = 6.3 Hz, J = 3.3 Hz, 2H, Phthz-CH), 7.56 (td, J = 7.7 Hz, J = 1.9 Hz, 4H, Py-CH), 7.31 (d, J = 7.9 Hz, 4H, Py-CH), 7.13 (ddd, J = 7.5 Hz, J = 4.9 Hz, J = 1.1 Hz, 4H, Py-CH),

6.81 (s, 2H, CH) ppm; ^{13}C NMR (126 MHz, $CDCl_3$, 300 K): δ = 160.2 (Py-C_q), 159.1 (Phthz-C_q), 149.6 (Py-CH), 136.7 (Py-CH), 132.1 (Phthz-CH), 126.7 (Phthz-CH), 125.3 (Phthz-C_q), 124.8 (Py-CH), 122.1 (Py-CH), 59.7 (CH) ppm; IR (neat): $\tilde{\nu}$ = 3072 (w), 3049 (w), 3009 (w), 2972 (w), 2863 (w), 1586 (s), 1568 (m), 1539 (w), 1467 (s), 1429 (s), 1043 (s), 993 (s), 768 (m), 751 (s), 682 (w), 659 (w), 616 (w) cm^{-1}; HRMS (ESI) *m/z* calcd. for $C_{30}H_{23}N_6$: 467.1979 [*M*+H]$^+$; found: 467.1977; HRMS (EI) *m/z* calcd. for $C_{30}H_{22}N_6$: 466.19059 [*M*]$^{+\cdot}$; found: 466.18950; Elemental analysis calcd. for $C_{30}H_{23}N_6$: C 77.23, H 4.75, N 18.01, found: C 76.97, H 4.72, N 18.03.

2.6. Preparation of the copper(I) complexes

2.6.1. General Procedure

To a colorless solution of tetrakis(acetonitrile)copper(I)-hexafluorophosphate $[Cu(CH_3CN)_4]PF_6$ or -triflate $[Cu(CH_3CN)_4]OTf$ (2 eq.) in CH_3CN (4 mL) was added a suspension of **bdpdz** or **bdptz** (1 eq.) in CH_3CN (4 mL) to generate a homogenous yellow to orange solution. The solution was stirred for 30 min at room temperature. After removing the solvent under reduced pressure **1a**-PF_6/OTf or **1b**-PF_6/OTf were obtained as colored microcrystalline solids (87-98 %).

2.6.2. Synthesis of $[Cu_2(bdpdz)(CH_3CN)_2](PF_6)_2$ (1a-PF_6)

In the same manner as described above, **1a**-PF_6 was obtained as an orange microcrystalline solid (265 mg, 318 µmol, 98 %).

To a colorless solution of 242 mg (649 µmol) tetrakis(acetonitrile)copper(I)-hexafluorophosphate dissolved in 4 mL acetonitrile was added a suspension of 135 mg (324 µmol) **bdpdz** in 4 mL acetonitrile. The resulting orange solution was stirred for 30 min at room temperature. After removing the solvent under reduced pressure 265 mg (318 µmol, 98 %) **1a**-PF_6 was obtained as an orange microcrystalline solid.

^{1}H NMR (400 MHz, CD_3CN, 300 K): δ 8.57 (s, 4H, Py-CH), 7.97-7.72 (m, 10H), 7.50-7.35 (m, 4H), 6.11 (s, 2H), 1.96 (s, 6H) ppm; ^{13}C NMR (101 MHz, CD_3CN, 300 K): δ = 158.6 (Pydz-C_q), 154.2 (Py-C_q), 150.5 (Py-CH), 140.1 (Py-CH, Pydz-CH), 127.0 (Py-CH), 125.0 (Py-CH), 118.3 (CH_3CN), 57.5 (CH), 1.62 (CH_3CN) ppm; ^{13}C NMR (101 MHz, $(CD_3)_2CO$, 300 K): δ = 158.6 (Pydz-C_q), 154.3 (Py-C_q), 150.9 (Py-CH), 140.6 (Py-CH), 134.4 (Pydz-CH), 127.2 (Py-CH), 125.3 (Py-CH), 117.6 (CH_3CN), 57.5 (CH), 1.06 (CH_3CN) ppm; IR (neat): 3105 (w), 3076 (w), 2956 (w), 1600 (m), 1575 (w), 1470 (w), 1422 (m), 1337 (w), 1151 (m), 1056 (w), 1017 (w), 883 (m), 828 (s), 774 (m), 755 (m), 654 (m), 552 (s) cm^{-1}; UV/Vis (acetone): λ_{max} (ε) = 322 nm (4450 M^{-1} cm^{-1}), 406 nm (1250 M^{-1} cm^{-1}); HRMS (ESI) *m/z* calcd. for $C_{26}H_{20}N_6Cu_2PF_6$: 686.9978 [M]$^+$; found: 686.9973; *m/z* calcd. for $C_{26}H_{20}N_6Cu_2$: 271.0165 [M]$^{2+}$; found: 271.0162; Elemental analysis calcd. for $C_{30}H_{26}N_8Cu_2P_2F_{12}$: C 39.35, H 2.86, N 12.24, found: C 39.12, H 2.90, N 12.24.

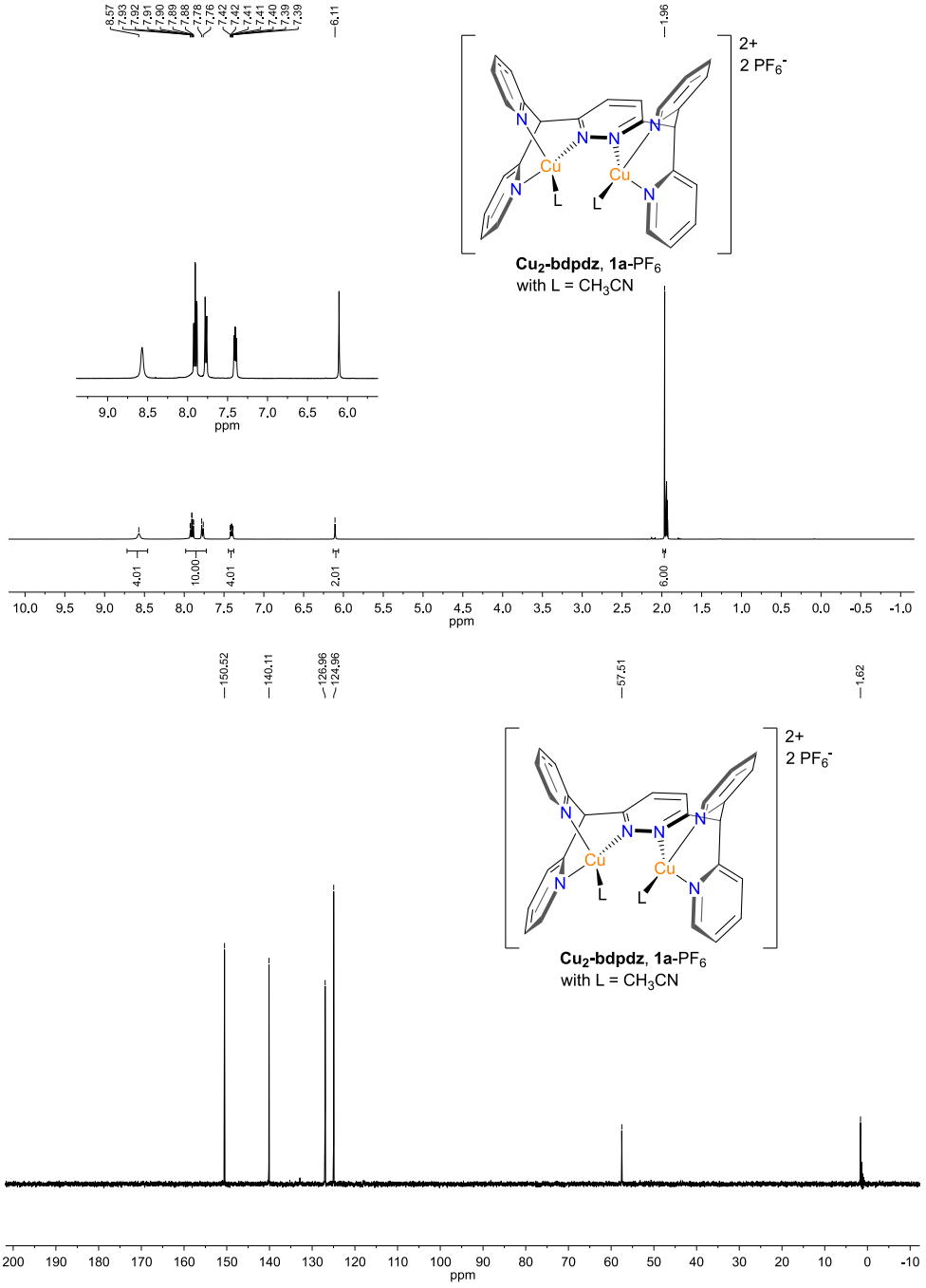

Figure S4: ^{1}H-NMR (top) and ^{13}C-NMR (bottom) of **1a**-PF_6 in CD_3CN (^{1}H: 1.94 ppm, ^{13}C: 1.32 ppm, 118.26 ppm).

2.6.3. Synthesis of $[Cu_2(bdpdz)(CH_3CN)_2](OTf)_2$ (1a-OTf)

In the same manner as described above **1a**-OTf was obtained as a dark red microcrystalline solid (286 mg, 310 µmol, 91 %).

To a colorless solution of 256 mg (678 µmol) tetrakis(acetonitrile)copper(I)-triflate dissolved in 4 mL acetonitrile was added a suspension of 141 mg (339 µmol) **bdpdz** in 4 mL acetonitrile. The resulting red solution was stirred for 30 min at room temperature. After removing the solvent under reduced pressure 286 mg (310 µmol, 91 %) **1a**-OTf was obtained as a dark red microcrystalline solid.

^{1}H NMR (400 MHz, CD_3CN, 300 K): δ = 8.54 (s, 4H, Py-CH), 8.00-7.76 (m, 10H, Py-CH, Pydz-CH), 7.40 (ddd, J = 7.5 Hz, 4H, Py-CH), 6.16 (s, 2H, CH), 1.96 (s, 6H, CH_3CN) ppm; ^{13}C NMR (101 MHz, CD_3CN, 300 K): δ = 158.5 (Pydz-C_q), 154.1 (Py-C_q), 150.5 (Py-CH), 140.1 (Py-CH, Pydz-CH), 127.0 (Py-CH), 125.0 (Py-CH), 118.3

(CH_3CN), 57.40 (CH), 1.62 (CH_3CN) ppm; ^{13}C NMR (101 MHz, $(CD_3)_2CO$, 300 K): δ = 158.7 (Pydz-C_q), 154.4 (Py-C_q), 150.8 (Py-CH), 140.5 (Py-CH), 134.5 (Pydz-CH), 127.3 (Py-CH), 125.2 (Py-CH), 117.6 (CH_3CN), 57.20 (CH), 1.05 (CH_3CN) ppm; IR (neat): 3101 (w), 3075 (w), 2992 (w), 2936 (w), 1601 (m), 1569 (w), 1472 (w), 1440 (m), 1346 (w), 1281 (s), 1251 (s), 1225 (s), 1155 (s), 1030 (s), 858 (m), 842 (m), 771 (m), 754 (m), 677 (m), 656 (w), 635 (s), 571 (m), 516 (s) cm^{-1}; UV/Vis (acetone): λ_{max} (ε) = 322 nm (5330 $M^{-1}\,cm^{-1}$), 408 nm (1280 $M^{-1}\,cm^{-1}$); HRMS (ESI) *m/z* calcd. for $C_{26}H_{20}N_6Cu_2CF_3SO_3$: 690.9856 $[M]^+$; found: 690.9851; *m/z* calcd. for $C_{26}H_{20}N_6Cu_2$: 271.0165 $[M]^{2+}$; found: 271.0160; Elemental analysis calcd. for $C_{32}H_{26}N_8Cu_2O_6S_2F_6$: C 41.60, H 2.84, N 12.13, found: C 41.76, H 2.76, N 12.15.

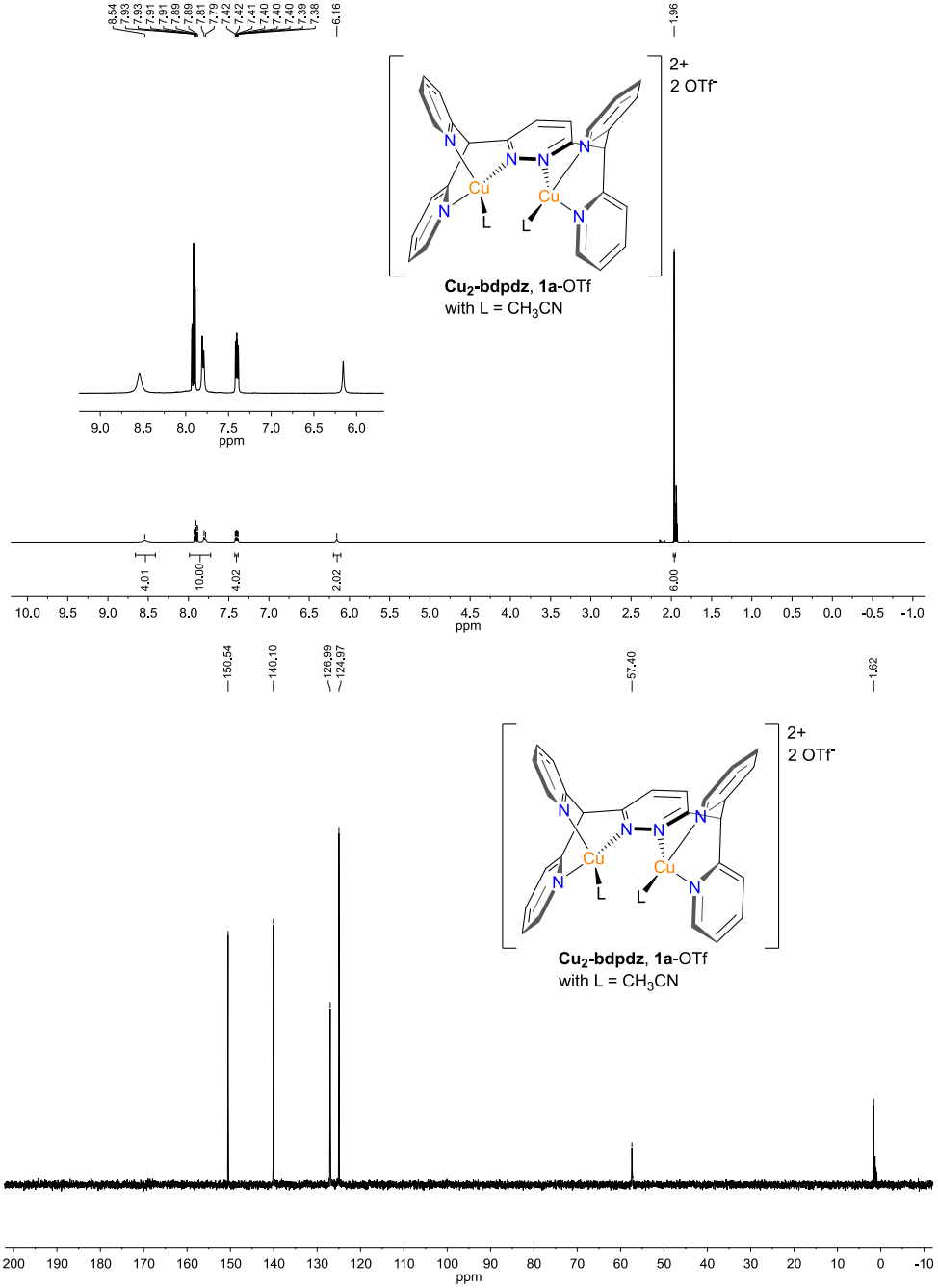

Figure S5: ^1H-NMR (top) and ^{13}C-NMR (bottom) of **1a**-OTf in CD_3CN (^1H: 1.94 ppm, ^{13}C: 1.32 ppm, 118.26 ppm).

2.6.4. Synthesis of $[Cu_2(bdptz)(CH_3CN)_2](PF_6)_2$ (1b-PF_6)

In the same manner as described above **1b**-PF_6 was obtained as a yellow microcrystalline solid (249 mg, 258 µmol, 91 %).

To a colorless solution of 211 mg (565 µmol) tetrakis(acetonitrile)copper(I)-hexafluorophosphate dissolved in 4 mL acetonitrile was added a suspension of 132 mg (283 µmol) **bdptz** in 4 mL acetonitrile. The resulting yellow solution was stirred for 30 min at room temperature. After removing the solvent under reduced pressure 249 mg (258 µmol, 91 %) **1b**-PF_6 was obtained as a yellow microcrystalline solid.

^{1}H NMR (400 MHz, CD_3CN, 300 K): δ = 8.96 (dd, J = 6.4 Hz, 2H, Phthz-CH), 8.67 (ddd, J = 5.1 Hz, 4H, Py-CH), 8.27 (dd, J = 6.3 Hz, 2H, Phthz-CH), 7.95 (m, 4H, Py-CH), 7.91 (m, 4H, Py-CH), 7.44 (ddd, J = 7.2 Hz, 4H, Py-CH), 6.93 (s, 2H, CH), 1.96 (s, 6H, CH_3CN) ppm; ^{13}C NMR (101 MHz, CD_3CN, 300 K): δ = 156.8 (Phthz-C_q), 154.1 (Py-C_q), 150.7 (Py-CH), 140.3 (Py-CH), 136.1 (Phthz-CH), 127.8 (Phthz-C_q), 127.2 (Py-CH), 126.3 (Phthz-CH), 125.2 (Py-CH), 118.3 (CH_3CN), 51.8 (CH), 1.62 (CH_3CN) ppm; IR (neat): 3110 (w), 3050 (w), 2948 (w), 1593 (m), 1574 (w), 1472 (w), 1440 (s), 1415 (w), 828 (s), 759 (m), 555 (s) cm^{-1}; UV/Vis (acetone): λ_{max} (***ε***) = 324 nm (5900 $M^{-1}\,cm^{-1}$), 385 nm (1450 $M^{-1}\,cm^{-1}$); HRMS (ESI) *m/z*: calcd. for $C_{30}H_{22}N_6Cu_2$: 296.0243 $[M]^{2+}$; found: 296.0244; Elemental analysis calcd. for $C_{34}H_{28}N_8Cu_2P_2F_{12}$: C 42.29, H 2.92, N 11.60, found: C 42.21, H 2.83, N 11.58.

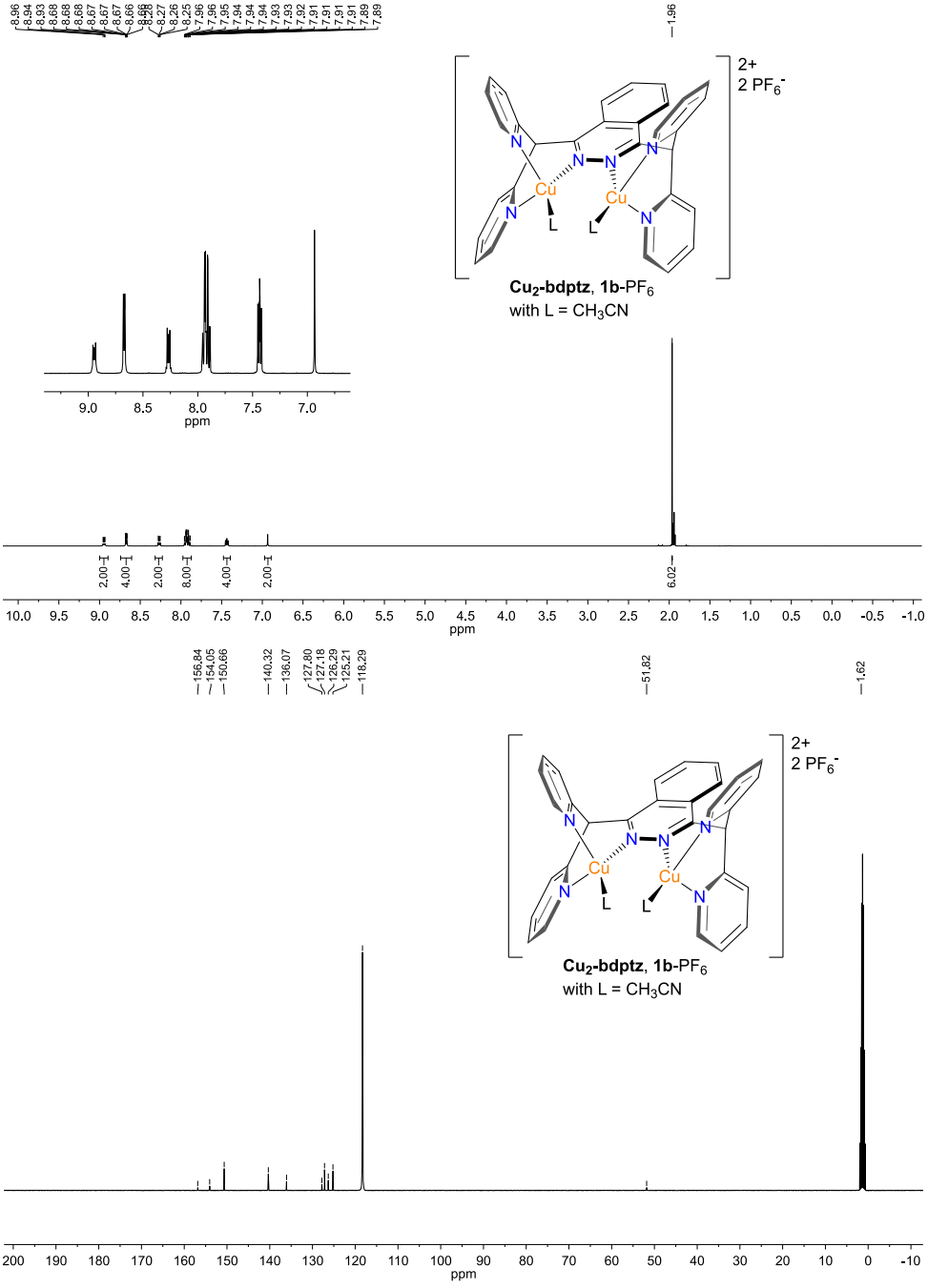

Figure S6: ^{1}H-NMR (top) and ^{13}C-NMR (bottom) of **1b**-PF_6 in CD_3CN (^{1}H: 1.94 ppm, ^{13}C: 1.32 ppm, 118.26 ppm).

2.6.5. Synthesis of $[Cu_2(bdptz)(CH_3CN)_2](OTf)_2$ (1b-OTf)[20]

The complex **1b**-OTf was synthesized by modification of the published procedure.[20] In the same manner as described above **1b**-OTf was obtained as an orange microcrystalline solid (241 mg, 247 µmol, 87 %).

To a colorless solution of 214 mg (569 µmol) tetrakis(acetonitrile)copper(I)-triflate dissolved in 4 mL acetonitrile was added a suspension of 133 mg (284 µmol) **bdptz** in 4 mL acetonitrile. The resulting yellow solution was stirred for 30 min at room temperature. After removing the solvent under reduced pressure 241 mg (247 µmol, 87 %) **1b**-OTf was obtained as an orange microcrystalline solid.

^{1}H NMR (400 MHz, CD_3CN, 300 K): δ = 8.97 (dd, J = 6.4 Hz, 2H, Phthz-CH), 8.67 (dd, J = 5.1 Hz, 4H, Py-CH), 8.26 (dd, J = 6.3 Hz, 2H, Phthz-CH), 7.96 (dt, J = 7.8 Hz, 4H, Py-CH), 7.91 (td, J = 7.7 Hz, 4H, Py-CH), 7.43 (ddd, J = 7.5 Hz, 4H, Py-CH), 6.97 (s, 2H, CH), 1.96 (s, 6H, CH_3CN) ppm; ^{13}C NMR (101 MHz, CD_3CN, 300 K): δ = 156.5 (Phthz-C_q), 153.9 (Py-C_q), 150.5 (Py-CH), 140.1 (Py-CH), 135.9 (Phthz-CH), 127.0 (Phthz-C_q), 126.9 (Py-CH), 126.2 (Phthz-CH), 125.0 (Py-CH), 118.3 (CH_3*C*N), 51.7 (CH), 1.62 (*C*H_3CN) ppm; IR (neat): 3110 (w), 3050 (w), 2948 (w), 1593 (m), 1568 (w), 1472 (w), 1440 (s), 1249 (s), 1148 (s), 1026 (s), 861 (w), 765 (m), 631 (s), 574 (s), 516 (s) cm^{-1}; UV/Vis (acetone): λ_{max} (***ε***) = 320 nm (6250 $M^{-1}\,cm^{-1}$), 382 nm (1560 $M^{-1}\,cm^{-1}$); HRMS (ESI) *m/z* calcd. for $C_{30}H_{22}N_6Cu_2CF_3SO_3$: 741.0013 $[M]^+$; found: 741.0010; *m/z* calcd. for $C_{30}H_{22}N_6Cu_2$: 296.0243 $[M]^{2+}$; found: 296.0239; Elemental analysis calcd. for $C_{36}H_{28}N_8Cu_2O_6S_2F_6$: C 44.40, H 2.90, N 11.51, found: C 44.43, H 2.73, N 11.36.

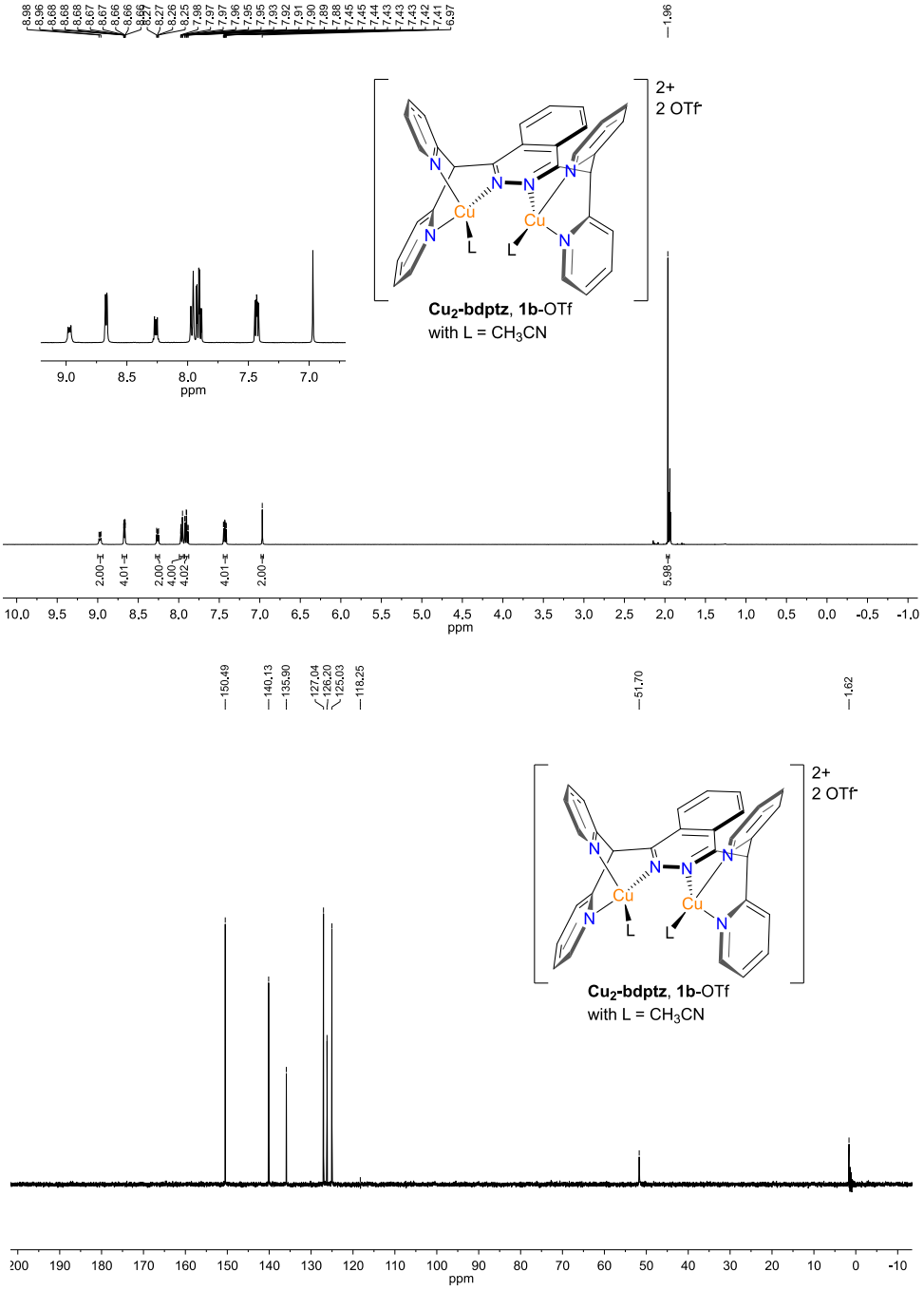

Figure S7: ^{1}H-NMR (top) and ^{13}C-NMR (bottom) of **1b**-OTf in CD_3CN (^{1}H: 1.94 ppm, ^{13}C: 1.32 ppm, 118.26 ppm).

2.7. General procedure for preparation of Cu_2O/Cu_4O_2 complexes for low-temperature measurements

Method A (dioxygen): For the detection of the mono-μ-oxo and **Cu_4O_2** complexes, low-temperature measurements (UV/Vis, resonance Raman, UHR-ESI, XAS) were done by cooling a 1-15 mM solution of the precursors **1a** or **1b** in acetone to -90 °C under N_2 atmosphere. After injection of dioxygen ($^{16}O_2$ or $^{18}O_2$; dioxygen was added via a cannula through the septum with a slight overpressure (slightly above 1 atm for a slow gas flow through the cuvette) for 15 min) formation of the copper-oxygen species could be observed (pale green tetranuclear species at -90 °C). In order to achieve the green **Cu_2O** complexes temperature was held between -40 °C and -30 °C for 15-30 min.

Method B (iodosobenzene): To obtain the desired **Cu_2O** complexes, excess solid iodosobenzene (which was prepared according to the literature procedure[22] and obtained as a white solid in 90 % yield) was added to a solution of precursor complexes of **1a** or **1b** in acetone between -40 °C and -25 °C under N_2 atmosphere. After complete addition, the suspension was stirred for 60-90 min at that temperature, then the unreacted PhIO was filtered off and the resulting green solution was investigated by UV/Vis spectroscopy and UHR-ESI mass spectrometry.

Method C (nitrous oxide): Cu_2O complexes were prepared in the same manner as described for reaction with dioxygen (method A) using N_2O instead of O_2. The starting temperature was set to 193 K instead of 183 K.

For instrumentation details see Section S1.1 for UV/Vis, S1.3 for rRaman, S.1.4 for Cyro-UHR-ESI MS and S1.5 for XAS.

2.8. General Procedure for reactivity studies of copper(I) complexes towards external substrates

In a typical reaction the copper(I) precursor **1a** or **1b** (1-2 mM, 1 eq.) was dissolved in dry acetone (15 mL) under an inert gas atmosphere. O_2 was added at -35 °C (238 K) via a cannula through the septum with a pressure slightly above 1 atm for a slow gas flow through the reaction vessel. Color change to green was observed after 30 seconds. To ensure quantitative formation of the **Cu_2O** complex the addition of O_2 was continued for 15 minutes. Then the substrate (10-50 eq.) was added. The reaction mixture was stirred for 2 h at -35 °C without bubbling O_2, but under an O_2 atmosphere, and for additional 2 h at room temperature. After 45 min at room temperature extra dioxygen was added via the cannula for 10 min; then, the solution was stirred for another hour at room temperature under O_2 atmosphere. After treatment with a saturated solution of Na_2-EDTA (10 mL) the reaction was stopped and the organic phase was separated, the aqueous phase was extracted with dichloromethane (2x 15 mL), the combined organic phases were dried with sodium sulfate, filtered and solvents were removed under reduced pressure. Characterization of the obtained residues was done by means of GC mass spectrometric measurements (vide infra). Reactions were carried out at least duplicate; values presented in this work are averaged. Blind reactions were also performed in the same manner but without the copper complexes (in case of DHA) as well as using $[Cu(CH_3CN)_4]PF_6$ or $[Cu(CH_3CN)_4]OTf$ instead of **1a** or **1b**. All control experiments lead to poorer results compared to the activity with **1a** or **1b** (see below).

3. Additional Information about the Crystal Structures

3.1. Crystal structure of the ligand bdptz (compound 1)

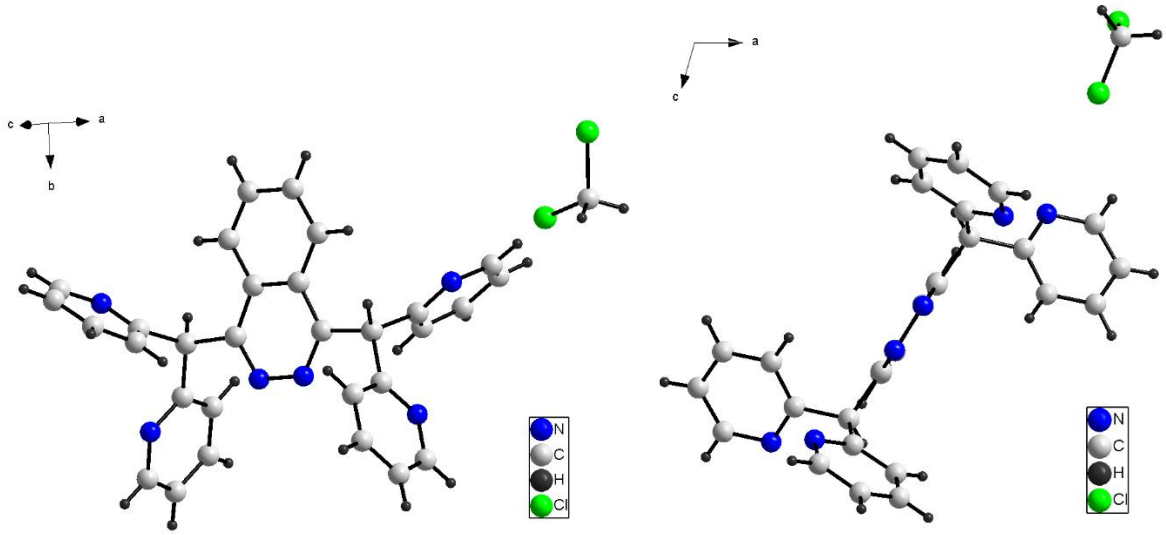

Figure S8: Molecular structure of the phthalazine ligand **bdptz**. Colorless crystals suitable for single-crystal X-ray diffraction analysis were obtained. Additional dichloromethane molecules complete the crystal structure (are omitted for clarity). The right structure shows the view along the crystallographic *b* axis. Crystal system: monoclinic. Space group: C2/c.

Table S3: Full table with the bond length (Å) and angles (°) of **bdptz** (**1b**). Symmetry transformations used to generate equivalent atoms: A: -x+1,y,-z+3/2.

N(1)-C(1)	1.3069(19)	C(6)-C(10)	1.382(3)
N(1)-N(1A)	1.387(2)	N(2)-C(7)	1.348(3)
C(1)-C(2)	1.434(2)	C(7)-C(8)	1.363(3)
C(1)-C(5)	1.520(2)	C(8)-C(9)	1.374(3)
C(2)-C(2A)	1.407(3)	C(9)-C(10)	1.376(3)
C(2)-C(3)	1.412(2)	C(11)-N(3)	1.329(2)
C(3)-C(4)	1.372(2)	C(11)-C(15)	1.377(3)
C(4)-C(4A)	1.402(4)	N(3)-C(12)	1.347(3)
C(5)-C(11)	1.519(2)	C(12)-C(13)	1.360(3)
C(5)-C(6)	1.524(2)	C(13)-C(14)	1.367(3)
C(6)-N(2)	1.333(2)	C(14)-C(15)	1.379(3)
C(1)-N(1)-N(1A)	120.05(9)	C(10)-C(6)-C(5)	118.85(15)
N(1)-C(1)-C(2)	123.24(14)	C(6)-N(2)-C(7)	116.85(17)
N(1)-C(1)-C(5)	116.69(13)	N(2)-C(7)-C(8)	123.8(2)
C(2)-C(1)-C(5)	120.04(13)	C(7)-C(8)-C(9)	118.72(18)
C(2A)-C(2)-C(3)	119.39(9)	C(8)-C(9)-C(10)	118.8(2)
C(2A)-C(2)-C(1)	116.71(8)	C(9)-C(10)-C(6)	119.03(19)
C(3)-C(2)-C(1)	123.90(14)	N(3)-C(11)-C(15)	122.30(17)
C(4)-C(3)-C(2)	120.15(15)	N(3)-C(11)-C(5)	115.85(15)
C(3)-C(4)-C(4A)	120.45(10)	C(15)-C(11)-C(5)	121.83(15)
C(11)-C(5)-C(1)	110.13(12)	C(11)-N(3)-C(12)	116.61(17)
C(11)-C(5)-C(6)	113.53(13)	N(3)-C(12)-C(13)	124.9(2)
C(1)-C(5)-C(6)	112.30(12)	C(12)-C(13)-C(14)	117.67(19)
N(2)-C(6)-C(10)	122.83(16)	C(13)-C(14)-C(15)	119.1(2)
N(2)-C(6)-C(5)	118.31(15)	C(11)-C(15)-C(14)	119.43(19)
C(16)-Cl(2)	1.653(8)	C(16')-Cl(2')	1.600(11)
C(16)-Cl(1)	1.756(7)	C(16')-Cl(1')	1.716(12)
Cl(2)-C(16)-Cl(1)	114.3(4)	Cl(2')-C(16')-Cl(1')	119.8(8)

3.2. Crystal structure of $[Cu^{I}Cu^{II}Cu^{I}(bdptz)_2(CH_3CN)_2](OTf)_4$ (compound 2)

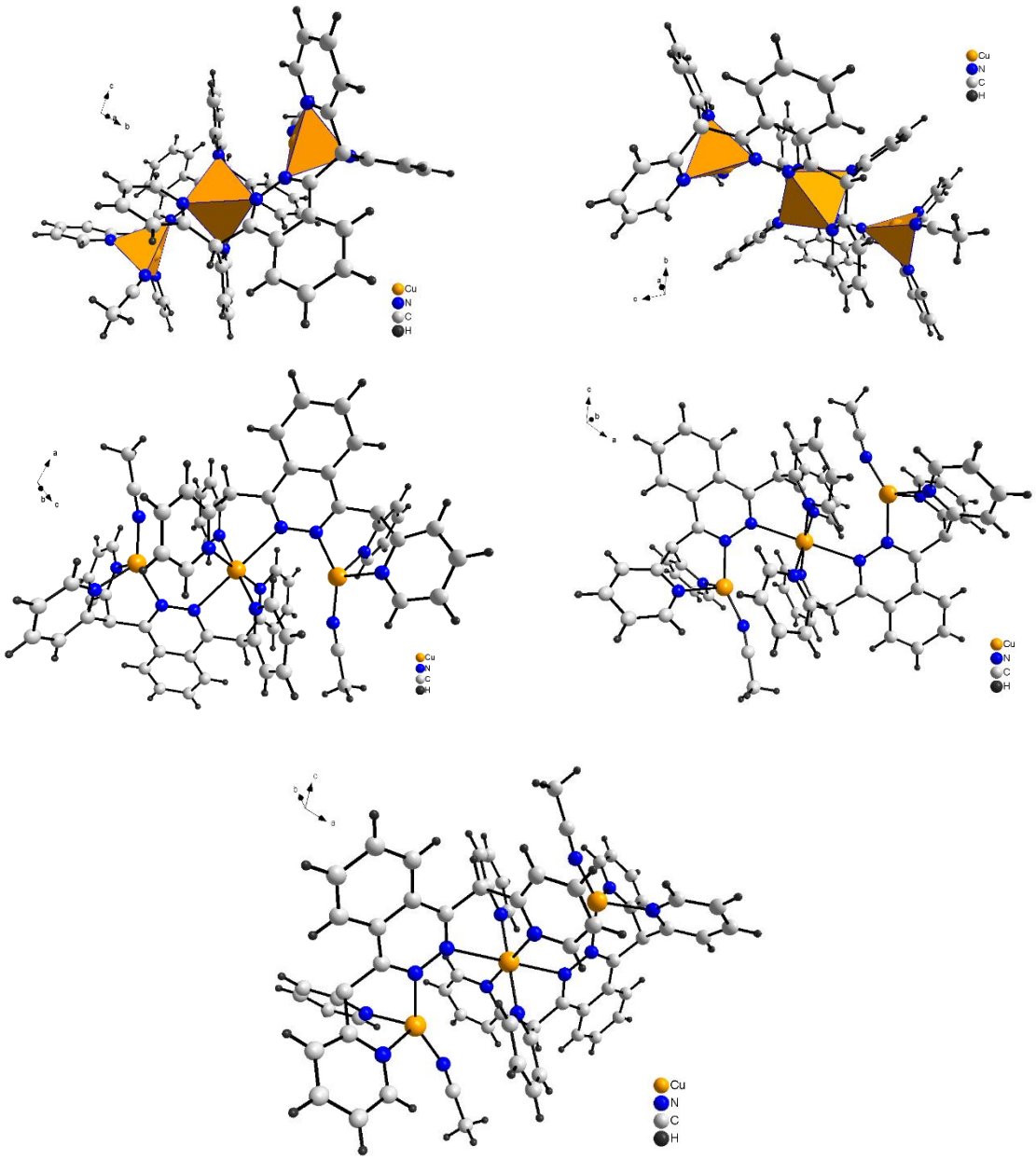

Figure S9: Different perspectives of the molecular structure of the trinuclear complex bearing **bdptz** as ligand. The molecular structure reveals a trinuclear mixed-valent $Cu^{I}Cu^{II}Cu^{I}$-complex demonstrating the ability of the used ligand system to stabilize both oxidation states copper(I) and copper(II) which is an important requirement for the final catalyst. The shown polyhedral (orange) represent tetrahedrons for the two Cu(I) units (the copper ion lies within the plane of the triangle) and a Jahn-Teller distorted octahedron for the Cu(II) moiety within the trinuclear structure. Crystal system: monoclinic. Space group: $P2_1/n$. Notably, one acetonitrile molecule completes the coordination sphere of the copper(I) centers and not acetone (which was the solvent). Additional acetone molecules complete the crystal structure (are omitted for clarity).

Table S4: Full table with the bond length (Å) and angles (°) of the trinuclear mixed-valent copper(I) copper(II) copper(I) complex supported by the ligand **bdptz**. Symmetry transformations used to generate equivalent atoms: A: -x+3,-y+1,-z+3.

Cu(1)-N(4A)	2.007(3)	Cu(1)-N(3)	2.020(3)
Cu(1)-N(4)	2.007(3)	Cu(1)-N(3A)	2.020(3)
Cu(1)-N(1)	2.491(3)	Cu(1)-N(1A)	2.491(3)
N(4A)-Cu(1)-N(4)	180.00(16)	N(4A)-Cu(1)-N(3A)	86.93(12)
N(4A)-Cu(1)-N(3)	93.07(12)	N(4)-Cu(1)-N(3A)	93.07(12)
N(4)-Cu(1)-N(3)	86.93(12)	N(3)-Cu(1)-N(3A)	180.00(10)
N(1)-Cu(1)-N(4)	83.36(12)	N(1)-Cu(1)-N(4A)	96.64(12)
N(1)-Cu(1)-N(1A)	180.00(16)	N(1)-Cu(1)-N(3)	85.95(11)
N(1)-Cu(1)-N(3A)	94.05(11)	N(1A)-Cu(1)-N(3)	94.05(11)
N(1A)-Cu(1)-N(3A)	85.95(11)	N(1A)-Cu(1)-N(4)	96.64(12)
N(1A)-Cu(1)-N(4A)	83.36(12)		
Cu(2)-N(31)	1.895(3)	Cu(2)-N(5)	2.073(4)
Cu(2)-N(2)	2.039(3)	Cu(2)-N(6)	2.121(3)
N(31)-Cu(2)-N(2)	147.86(14)	N(31)-Cu(2)-N(6)	103.15(15)
N(31)-Cu(2)-N(5)	118.08(15)	N(2)-Cu(2)-N(6)	91.46(12)
N(2)-Cu(2)-N(5)	89.99(13)	N(5)-Cu(2)-N(6)	89.86(13)
N(1)-C(8)	1.305(5)	C(15)-N(4)	1.342(5)
N(1)-N(2)	1.383(4)	C(15)-C(19)	1.389(5)
N(2)-C(1)	1.315(5)	N(4)-C(16)	1.350(5)
C(1)-C(2)	1.427(5)	C(16)-C(17)	1.381(6)
C(1)-C(20)	1.525(5)	C(17)-C(18)	1.359(8)
C(2)-C(7)	1.402(5)	C(18)-C(19)	1.379(7)
C(2)-C(3)	1.405(5)	C(20)-C(21)	1.531(5)
C(3)-C(4)	1.375(6)	C(20)-C(26)	1.531(5)
C(4)-C(5)	1.389(7)	C(21)-N(5)	1.331(5)
C(5)-C(6)	1.375(6)	C(21)-C(25)	1.384(6)
C(6)-C(7)	1.411(5)	N(5)-C(22)	1.335(6)
C(7)-C(8)	1.431(5)	C(22)-C(23)	1.373(7)
C(8)-C(9)	1.532(5)	C(23)-C(24)	1.373(8)
C(9)-C(15)	1.504(5)	C(24)-C(25)	1.372(8)
C(9)-C(10)	1.513(5)	C(26)-N(6)	1.333(5)
C(10)-N(3)	1.344(5)	C(26)-C(30)	1.398(5)
C(10)-C(14)	1.372(5)	N(6)-C(27)	1.345(5)
N(3)-C(11)	1.355(5)	C(27)-C(28)	1.380(6)
C(11)-C(12)	1.365(6)	C(28)-C(29)	1.380(7)
C(12)-C(13)	1.380(7)	C(29)-C(30)	1.386(7)
C(13)-C(14)	1.376(7)		
C(8)-N(1)-N(2)	119.6(3)	N(3)-C(10)-C(9)	116.8(3)
C(1)-N(2)-N(1)	120.2(3)	C(14)-C(10)-C(9)	121.8(4)
N(2)-C(1)-C(2)	122.7(3)	N(3)-C(11)-C(12)	121.2(4)
N(2)-C(1)-C(20)	117.6(3)	C(11)-C(12)-C(13)	119.6(4)
C(2)-C(1)-C(20)	119.6(3)	C(14)-C(13)-C(12)	118.9(4)
C(7)-C(2)-C(3)	119.4(4)	C(10)-C(14)-C(13)	119.5(4)
C(7)-C(2)-C(1)	116.5(3)	N(4)-C(15)-C(19)	120.7(4)
C(3)-C(2)-C(1)	124.0(4)	N(4)-C(15)-C(9)	119.0(3)
C(4)-C(3)-C(2)	120.1(4)	C(19)-C(15)-C(9)	120.2(3)
C(3)-C(4)-C(5)	120.8(4)	C(15)-N(4)-C(16)	119.7(3)
C(6)-C(5)-C(4)	120.0(4)	N(4)-C(16)-C(17)	121.4(4)
C(5)-C(6)-C(7)	120.4(4)	C(18)-C(17)-C(16)	119.1(4)
C(2)-C(7)-C(6)	119.3(4)	C(17)-C(18)-C(19)	120.0(4)
C(2)-C(7)-C(8)	116.9(3)	C(18)-C(19)-C(15)	119.1(4)
C(6)-C(7)-C(8)	123.7(4)	C(1)-C(20)-C(21)	113.5(3)
N(1)-C(8)-C(7)	123.1(3)	C(1)-C(20)-C(26)	111.1(3)
N(1)-C(8)-C(9)	115.9(3)	C(21)-C(20)-C(26)	110.5(3)
C(7)-C(8)-C(9)	120.9(3)	N(5)-C(21)-C(25)	122.4(4)
C(15)-C(9)-C(10)	112.1(3)	N(5)-C(21)-C(20)	118.4(3)
C(15)-C(9)-C(8)	113.9(3)	C(25)-C(21)-C(20)	119.3(4)
C(10)-C(9)-C(8)	110.4(3)	C(21)-N(5)-C(22)	117.8(4)
N(3)-C(10)-C(14)	121.4(4)	N(5)-C(22)-C(23)	123.6(5)

4. Overview of the obtained Results with O_2, N_2O and PhIO

Table S5: Overview of the obtained data for the **bdpdz** (**1a**) and **bdptz** (**1b**) systems using different oxygen transfer reagents.

		Cu_2O (233 - 253 K)		Cu_4O_2 (183 K)	
	[O]	**2**-PF_6	**2**-OTf	**3**-PF_6	**3**-OTf
Model system		**1a (bdpdz)**		**1a (bdpdz)**	
UV/Vis λ /nm (ε / $M^{-1}cm^{-1}$)	O_2	370 (2739) 421 (1282) 630 (264)	371 (2391) 422 (1119) 630 (219)	397 (1956) 619 (200)	398 (2754) 613 (160)
	N_2O	371 (2420) 414 (1230) 631 (233)	371 (1567) 414 (933) 628 (283)	N.A.	N.A.
	1 eq. PhIO	N.A.	366 (1225) 411 (sh) 637 (43)	N.A.	N.A.
	excess PhIO	360 (sh) 412 (sh) 633 (46)	360 (sh) 407 (sh) 630 (88)	N.A.	N.A.
rRaman ν ($\Delta^{18}O_2$) / cm^{-1}	O_2	629 (23)	619 (11)	607 (14) 854 (62)	N.A. N.A.
	N_2O	N.A.	N.A.	N.A.	N.A.
UHR-ESI-MS	O_2	$[LCu_2O]^{2+}$	$[LCu_2O]^{2+}$	$[L_2Cu_4O_2]^{4+[b]}$	$[L_2Cu_4O_2](OTf)^{3+}$
	PhIO	$[LCu_2O]^{2+}$	$[LCu_2O]^{2+}$	$[L_2Cu_4O_2]^{4+[b]}$	$[L_2Cu_4O_2]^{4+[b]}$
Model system		**1b (bdptz)**		**1b (bdptz)**	
UV/Vis λ /nm (ε / $M^{-1}cm^{-1}$)	O_2	368 (2488) 417 (1343) 633 (207)	370 (2642) 421 (1350) 630 (213)	393 (2150) 619 (168)	390 (2770) 621 (222)
	N_2O	369 (2593) 416 (1378) 631 (220)	372 (2257) 418 (1209) 630 (191)	N.A.	N.A.
	1 eq. PhIO	362 (1864) 415 (805) 639 (117)	351 (2303) 410 (694) 648 (77)	N.A.	N.A.
	excess PhIO	368 (1867) 405 (sh) 632 (69)	360 (1144) 408 (507) 638 (77)	N.A.	N.A.
rRaman ν ($\Delta^{18}O_2$) / cm^{-1}	O_2	623 (20)	619 (8)	607 (16) 854 (52)	604 (8) 855 (57)
	N_2O	623; 1283+ 2233[c]	N.A.	N.A.	N.A.
UHR-ESI-MS	O_2	$[LCu_2O]^{2+}$	$[LCu_2O]^{2+}$	$[L_2Cu_4O_2]^{4+[b]}$	$[L_2Cu_4O_2]^{4+[b]}$ $[L_2Cu_4O_2](OTf)^{3+}$
	PhIO	$[LCu_2O]^{2+}$	$[LCu_2O]^{2+}$	$[L_2Cu_4O_2]^{4+[b]}$	$[L_2Cu_4O_2]^{4+[b]}$

General remarks: UV/Vis: Solvent: acetone; c = 0.6-1.0 mM. The exact position of the absorption bands depends extremely on the temperature; in case of **Cu_2O** complexes temperature vary between 223 K and 253 K, causing λ_{max} ranges between 628 nm and 639 nm (648 nm); but since this absorption feature is quite broad, this was expected. Reactions using dioxygen were carried out at least duplicate; values presented in this table are averaged. **rRaman:** Solvent: acetone; c = 9-16 mM. The laser excitation wavelength was 393 nm. **Cryo-UHR-ESI-MS:** L = ligand; **bdpdz** or **bdptz**; solvent: acetone; c around 0.01 mM. UHR-ESI-MS with PhIO was performed with a large excess of PhIO.

[a]The given molar absorption coefficient at these maxima are based on the assumption that the species is tetranuclear. [b]Only observed at 238 K. [c]Feature of free/bound N_2O which decreases with increasing **Cu_2O** feature indicating a correlation.

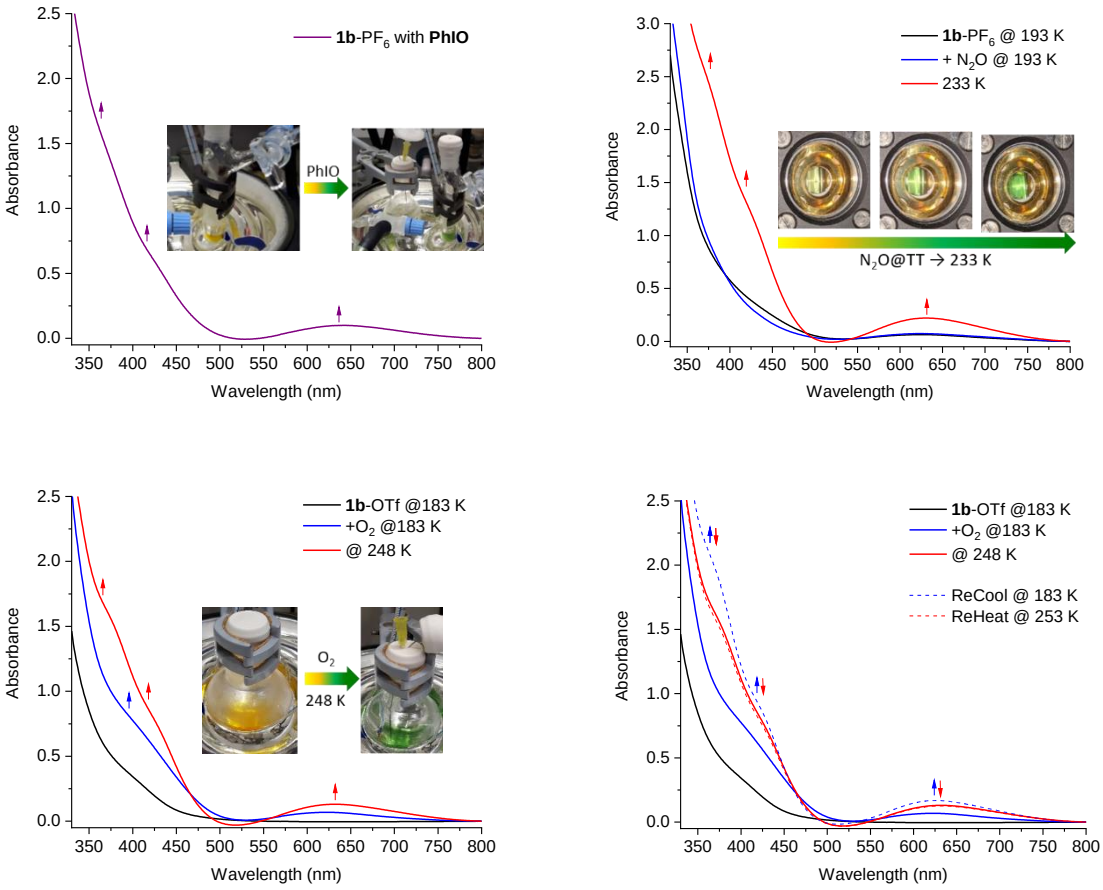

Figure S10: Overview of the obtained results generating the mono-μ-oxo species. Top, left: Iodosobenzene: UV/Vis spectra of the green solution obtained after reaction of the dinuclear copper(I) **bdptz** complex **1b**-PF_6 dissolved in acetone with an excess of PhIO at 238 K. **Top, right: Using nitrous oxide:** UV/Vis spectra of a solution of **1b**-PF_6 dissolved in acetone before (black) and after the reaction with N_2O (blue, red). The characteristic absorption feature of the **Cu_2O** species evolve upon warming along with the color change to green. **Bottom, left: Reaction with dioxygen:** Absorption spectra of a solution of **1b**-OTf dissolved in acetone before (black) and after the reaction with O_2 (blue, red). Two different species can be assigned upon reaction with dioxygen – the **Cu_4O_2** intermediate and the corresponding **Cu_2O** complex. **Bottom, right: Investigating the temperature-dependent equilibrium** with **1b**-OTf: Once the **Cu_2O** complex is formed, upon cleavage of the O-O bond of the **Cu_4O_2** species, the equilibrium is irreversible and thus the spectrum of the mono-μ-oxo species is fixed after re-cooling. l = 1 cm.

4.1. Using iodosobenzene (PhIO)

Following the approach shown in Scheme S1 we used *iodosobenzene* as oxygen transfer reagent to generate the desired **Cu_2O** motif. Upon reaction of **1a** and **1b** with PhIO in acetone at -35 °C (238 K) we observed a color change from yellow to intense green going along with a change of the initial precursor spectrum to the spectrum shown in Figure S11.

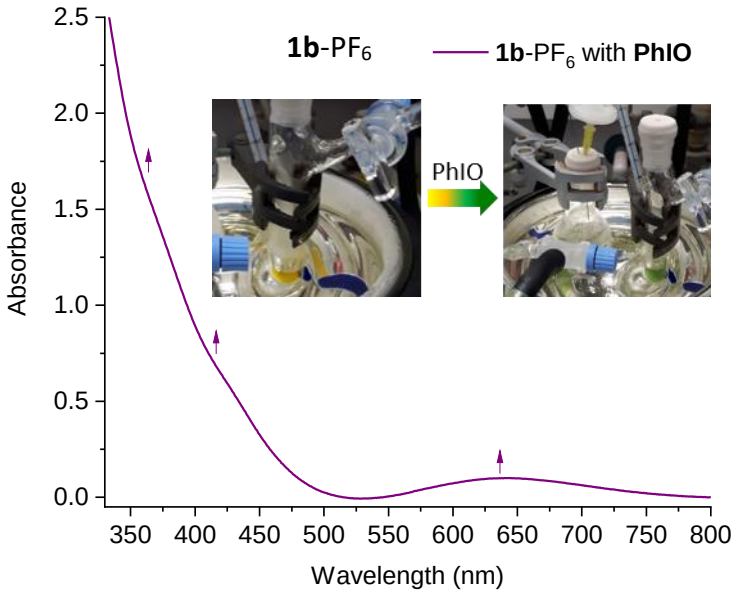

Figure S11: UV/Vis spectra of **Cu_2O** formation of **1b**-PF_6 using iodosobenzene.

The violet spectrum in Figure S11 contains three bands, i.e., at 362 nm (ε = 1864 M^{-1} cm^{-1}), 415 nm (ε = 805 M^{-1} cm^{-1}) and 639 nm (ε = 117 M^{-1} cm^{-1}) which is in good agreement with UV/Vis-spectroscopic data published for **Cu_2O** complexes (see Table S6). Correspondingly, Limberg and coworkers attributed three absorption features to the **Cu_2O** intermediate of their **FurNeu** dicopper(I) complex which upon oxygenation in acetonitrile at room temperature undergoes a color change from pale yellow to green; i.e., two broad bands, one between 400-500 nm (sh) and the other one at 644 nm (ε = 140 M^{-1} cm^{-1}), as well as a weak absorption band around 800-1100 (br).[29] Apart from the NIR band, these features correspond to those observed in our UV/Vis spectrum (Figure S11).

The formation of a mono-μ-oxo species by reaction with an excess of PhIO at -35 °C could also be confirmed through cryo-UHR-ESI mass spectrometry (see Figure S12-15).

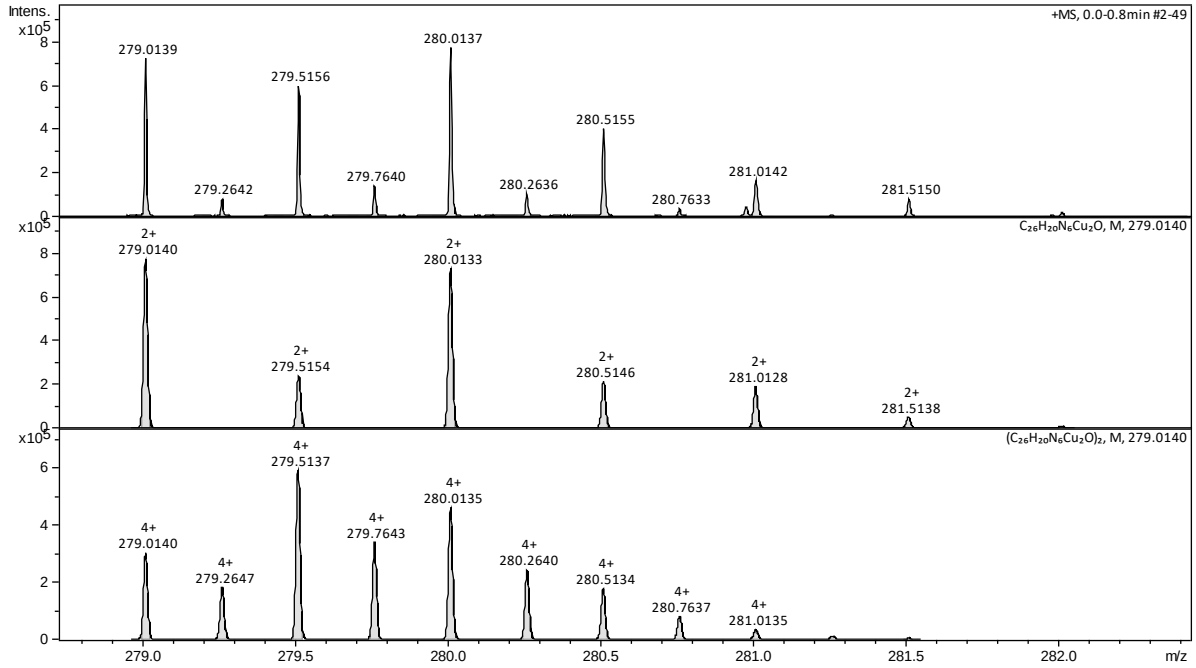

Figure S12: Cryo-UHR-ESI mass spectrum of **1a**-OTf with excess of PhIO at -35 °C after 3 h reaction time. The isotopic pattern and corresponding *m/z* value resemble the simulated spectrum for the **Cu_2O** and **Cu_4O_2** species. Additionally, mass spectra with triflate (one for **Cu_2O** and one or two for **Cu_4O_2** complexes) could be detected as well.

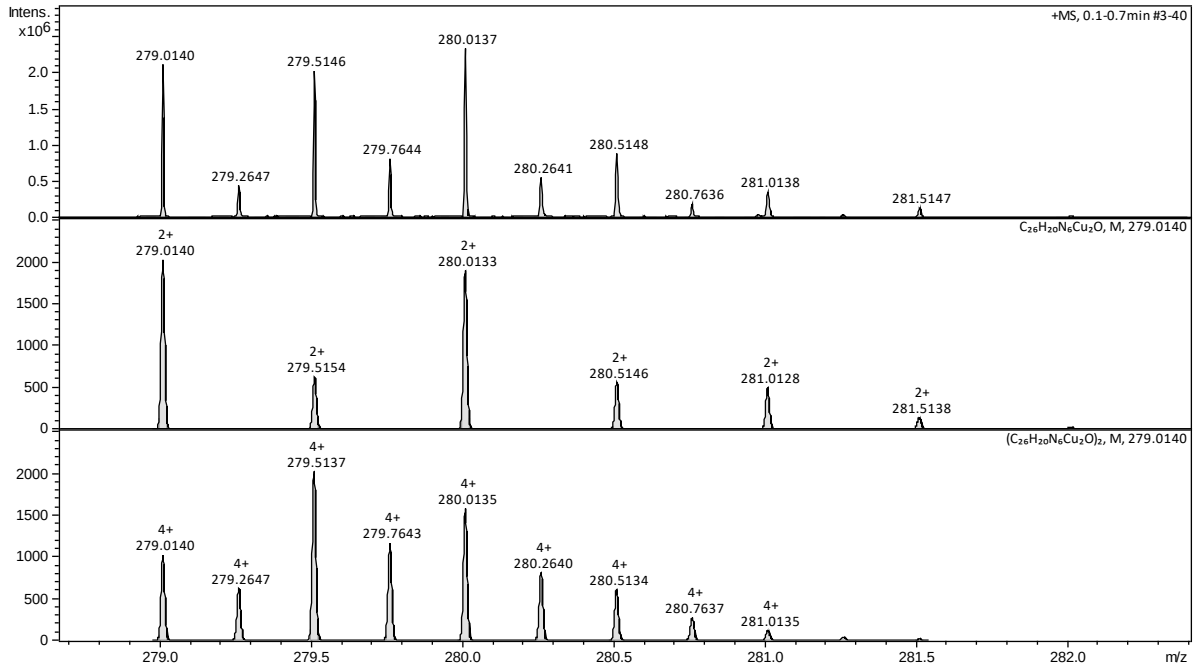

Figure S13: Cryo-UHR-ESI mass spectrum of **1a**-PF_6 with excess of PhIO at -35 °C after 3 h reaction time. The isotopic pattern and corresponding *m/z* value resemble the simulated spectrum for the **Cu_2O** and **Cu_4O_2** species.

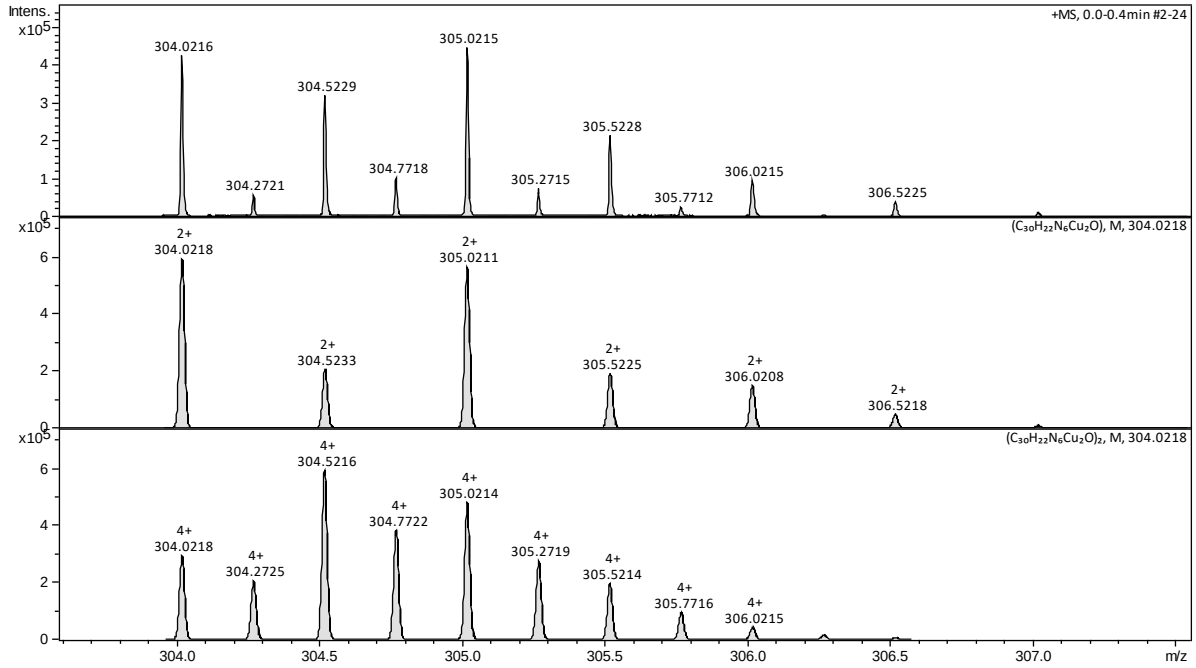

Figure S14: Cryo-UHR-ESI mass spectrum of **1b**-OTf with excess of PhIO at -35 °C after 3 h reaction time. The isotopic pattern and corresponding *m/z* value resemble the simulated spectrum for the $\mathbf{Cu_2O}$ and $\mathbf{Cu_4O_2}$ species. Additionally, mass spectra with triflate (one for $\mathbf{Cu_2O}$ and one or two for $\mathbf{Cu_4O_2}$ complexes) could be detected as well.

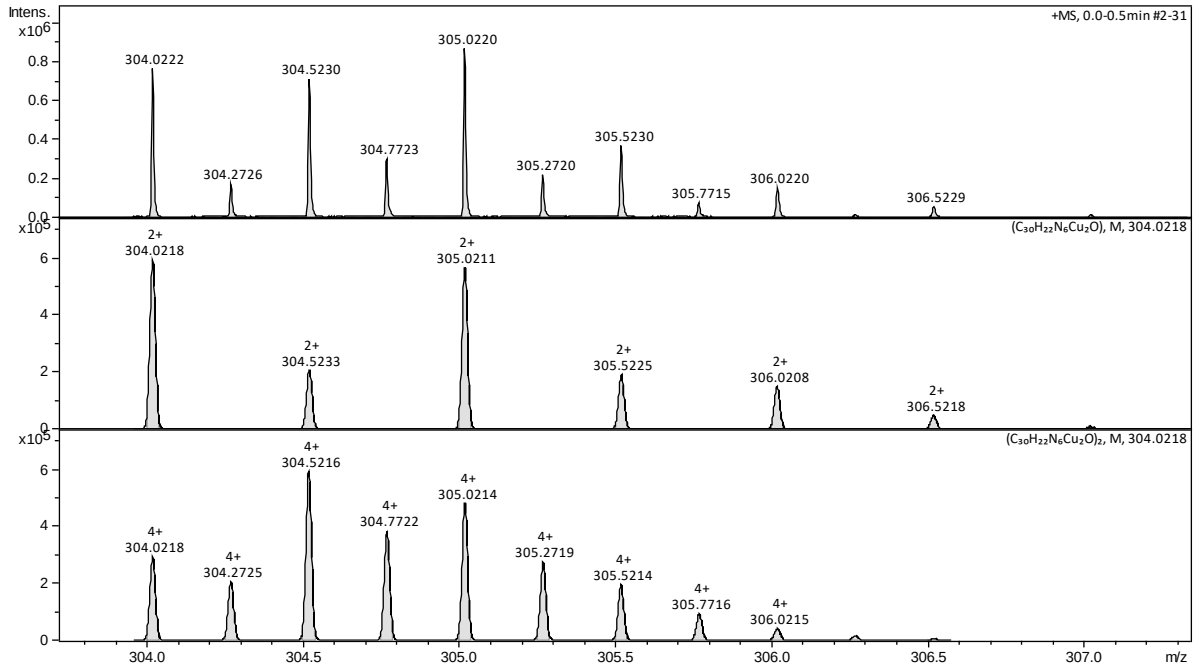

Figure S15: Cryo-UHR-ESI mass spectrum of **1b**-PF_6 with excess of PhIO at -35 °C after 3 h reaction time. The isotopic pattern and corresponding *m/z* value resemble the simulated spectrum for the $\mathbf{Cu_2O}$ and $\mathbf{Cu_4O_2}$ species.

Reaction of **1a**-PF_6, **1a**-OTf, **1b**-PF_6 or **1b**-OTf with PhIO at -35 °C provided the mass spectra shown in Figures S12-15 which are in excellent accordance with the calculated spectrum and simulated isotopic distribution pattern of the estimated doubly positively charged species, i.e., $[\mathbf{2b}\text{-}PF_6]^{2+}$ (feature is centered at 304.0222 *m/z* and calcd. 304.0218 *m/z*) containing only one O atom. When the $\mathbf{Cu_2O}$ complex of **1b**-PF_6 is prepared with $^{18}O_2$ the $\mathbf{Cu_2O}$-attributed peak shifts by one mass unit to 305.0239 *m/z*, as expected (calcd. *m/z* = 305.0223) (see additional mass spectra below; Section S7). Moreover, at this temperature and under the

conditions of the used method, we could also detect the **Cu_4O_2** species of **1a** and **1b**. As already proven, the tetranuclear species is not stable at -35 °C, this is likely caused due to collision of two **Cu_2O** fragments.

However, the reaction time to generate the **Cu_2O** complexes with iodosobenzene is quite long (up to 3 h) and the yield of **Cu_2O** is fairly low. This can be attributed to the very low solubility of PhIO in acetone and other organic solvents.

4.2. Using nitrous oxide (N_2O)

We decided to check whether our systems can be monooxygenated using an alternative oxygen-transfer reagent *nitrous oxide*, N_2O. Activation of N_2O is more challenging since the potent greenhouse gas (global warming potential is 310 times higher than that of CO_2)[23] is hard to break, especially under mild conditions.[24]

Fortunately, we were able to utilize N_2O as oxygen transfer reagent generating the desired mono-μ-oxo complexes along with the liberation of gaseous dinitrogen at low temperature. The reaction of **1b**-PF_6 with N_2O, resulted UV/Vis spectra for the mono-μ-oxo species, almost identical to what was obtained for the reaction with PhIO (cf. Figure S11). It is noteworthy that we were able to observe release of gaseous dinitrogen (see Figure S18 and the additional Video 1) accompanied by the color change from yellow to intense green (attributed to the formation of **Cu_2O** complex) upon increasing the temperature from -80 °C to -40 °C. Specifically, the red spectrum shown in Figure S17 exhibits two broad shoulders around 369 nm (ε = 2593 M^{-1} cm^{-1}) and 416 nm (ε = 1378 M^{-1} cm^{-1}) and a distinct absorption band at 631 nm (ε = 220 M^{-1} cm^{-1}) which attains its maximum intensity after keeping the solution at 233 K for at least 50 min. These values agree well with published spectroscopic data for **Cu_2O** complexes (cf. Table S6). The same results were obtained for **1a**-PF_6, **1a**-OTf and **1b**-OTf as summarized in Table S5 and shown in the following spectra. Figure S16 demonstrates again the color change from yellow to intense green, indicating **Cu_2O** formation.

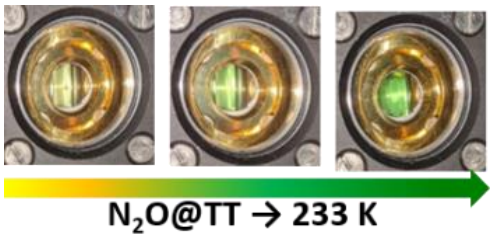

Figure S16: Observed color change during reaction with nitrous oxide and increasing the temperature from 193 K up to 233 K. After addition of N_2O at 193 K the color of the precursor complex **1a** and **1b** changed from yellow to pale yellow. Upon increasing the temperature, the characteristic green can be observed.

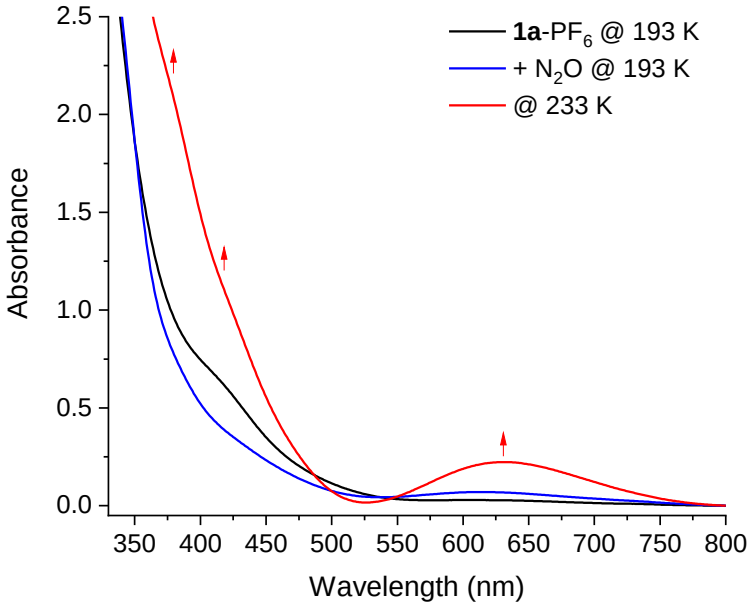

Figure S17: UV/Vis spectra of **1a**-PF_6 before (black) and after the reaction with nitrous oxide at 193 K (blue). Upon warming to 233 K the bands corresponding to **Cu_2O** motif grow and N_2 release can be seen. At 233 K the spectra of the mono-μ-oxo complex (red) is comparable to the spectra obtained with PhIO and O_2.

A video (evolution of N_2 gas upon reaction with N_2O yielding **Cu_2O** complex; Supplementary Video 1) can be found in the additional supplementary materials. The following spectrum (Figure S18, left; orange) demonstrates the N_2 release as well.

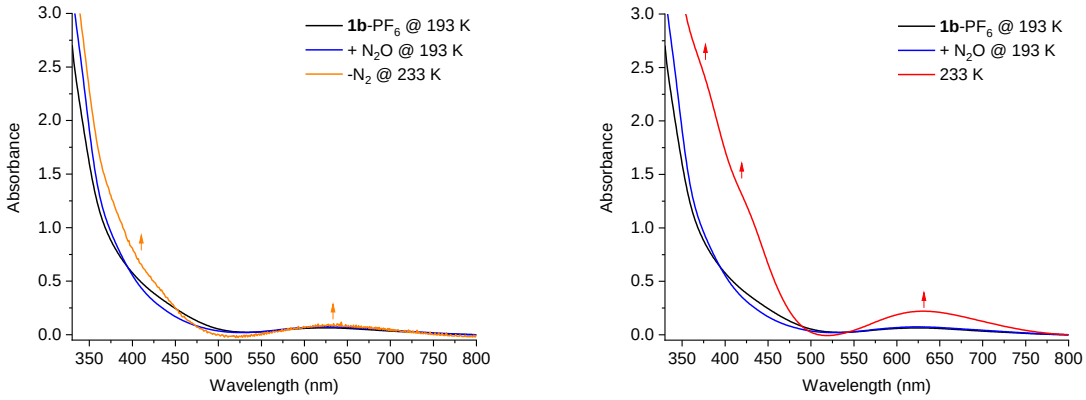

Figure S18: UV/Vis spectra of **1b**-PF_6 before (black) and after the reaction with nitrous oxide at 193 K (blue). **Left:** Upon warming to 233 K the bands corresponding to **Cu_2O** motif grow and N_2 release can be seen (orange). **Right:** At 233 K the spectra of the mono-μ-oxo complex (red) is comparable to the spectra obtained with PhIO and O_2.

To further confirm the identity of the **Cu_2O** complex and support the corresponding UV/Vis data, resonance Raman investigations were performed with nitrous oxide as potential O-transfer reagent. As shown in Figure S19, reaction of **1b**-PF_6 with nitrous oxide at -80 °C (193 K) leads to the emergence of two new peaks in the resonance Raman spectrum, both of which can be attributed to N_2O. Specifically, the peak at 1283 cm^{-1} originates from the N-O stretching vibration and the band at 2233 cm^{-1} can be attributed to the characteristic N-N stretching mode.

The observed frequencies are in very good agreement with the literature for free N_2O ($\nu_{N\text{-}N}$ = 2224 cm^{-1} and $\nu_{N\text{-}O}$ = 1285 cm^{-1}).[25]

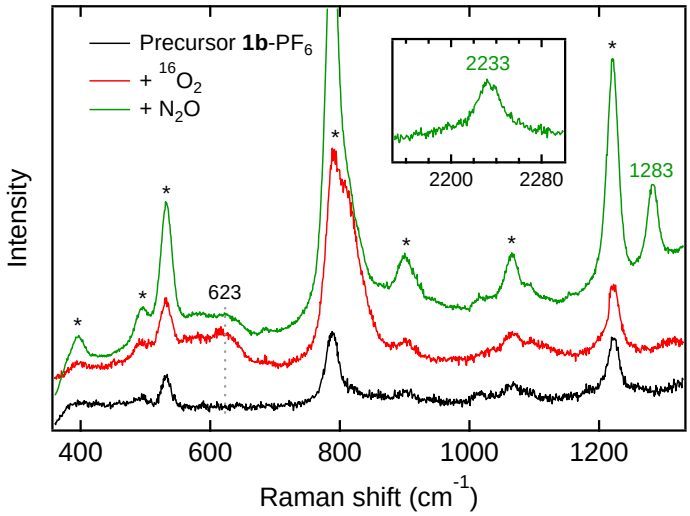

Figure S19: Resonance Raman spectra of **1b**-PF_6 before (black) and after the reaction with dioxygen (red) and upon reaction with nitrous oxide (green) at 238 K.

Upon increasing the temperature to -50 °C (223 K) both features decrease in intensity which we ascribe to the fact that coordination takes place. Further increasing the temperature leads to the liberation of gaseous dinitrogen. At -35 °C (238 K) a new peak evolves at 623 cm^{-1} (Figure S19, green). In analogy to the resonance Raman spectra obtained after reaction with dioxygen (Figure S19, red) the observed feature is attributed to the antisymmetric Cu-O stretching vibration of the mono-μ-oxo species.

5. UV/Vis spectroscopy

5.1. UV/Vis spectroscopy using dioxygen: Overview of the obtained data

Table S6: Overview of the experimentally and theoretically obtained absorption features for the **bdpdz** (**1a**) and **bdptz** (**1b**) systems after oxygenation leading to the corresponding **Cu_2O** (233 - 253 K) or **Cu_4O_2** complexes (183 K). In addition, selected examples of available data for **Cu_2O** and **Cu_4O_2** complexes are presented.

Model system	Cu_2O			Cu_4O_2[b]	
	TDDFT[a]	**2**-PF_6	**2**-OTf	**3**-PF_6	**3**-OTf
1a (bdpdz) λ /nm (ε / $M^{-1}cm^{-1}$)	390	370 (2739)	371 (2391)	397 (1956)	398 (2754)
	431	421 (1282)	422 (1119)	N.A.	N.A.
	554+701	630 (264)	630 (219)	619 (200)	613 (160)
1b (bdptz) λ /nm (ε / $M^{-1}cm^{-1}$)	380	368 (2488)	370 (2642)	393 (2150)	390 (2770)
	434	417 (1343)	421 (1350)	N.A.	N.A.
	572	633 (207)	630 (213)	619 (168)	621 (222)

General remarks: Solvent: acetone; Oxygenations were carried out at least duplicate; values presented here are averaged; c = 0.6-1.0 mM.
[a] Based on the assumption that acetone is the coordinating solvent; values with acetonitrile instead of acetone can be found within the SI. DFT: RI-B3LYP/def2-TZVP(-f). [b] The given molar absorptivities at these maxima are based on the assumption that the species is tetranuclear.

Cu_2O-complexes	λ /nm (ε / $M^{-1}cm^{-1}$)	Solvent	Special remarks
Cu-ZSM-5[26, 27]	441 752	solid	zeolite; after activation with dioxygen
Xanthdim[28]	640 (1000)	THF	$[(CuOCu)]_{1,2,n}$
FurNeu[29]	400-500 (sh) 644 (140) 800-1100 (br)	CH_3CN	$[FurNeu(Cu_2(\mu\text{-}O))](OTf)_2$
ENCA[30]	720 (1200) 810 (1200)	$PhNO_2$	$[((ENCA)CuCl)_4O_2]$
DENC[31]	233 (34900), 253 (31500) 760 (810) 838 (813)	DCM	$[((DENC)CuX)_4O_2]$; X = Cl, Br
TEED[32] with μ-Br	700 (265)	$PhNO_2$	$[((TEED)Cu)_2(\mu\text{-}Br)_2(\mu\text{-}O)]$
TEED[32] with μ-Br	280 (4400), 320 (5300) 500 (380, sh) 700 (265)	DCM	$[((TEED)Cu)_2(\mu\text{-}Br)_2(\mu\text{-}O)]$
TEED[33, 34] with μ-Cl	675 (228)	$PhNO_2$	$[((TEED)Cu)_2(\mu\text{-}Cl)_2(\mu\text{-}O)]$
^{Me}Py2[35]	345 (4000) 620 (100)	THF	$[(^{Me}Py2Cu)_2(\mu\text{-}O)](BArF)$ T = - 80 °C; RT→680 (100)
Tp^{Me}[36]	335 (2560) 660 (105)	$CHCl_3$	$[Tp^{Me}Cu)_2(\mu\text{-}O)]$
Cu_4O_2-complexes	**λ /nm (ε / $M^{-1}cm^{-1}$)**	**Solvent**	**Special remarks**
TEED[33, 34] with μ-Cl	380 (1600) 650 (360)	DCM	Relatively low absorptivities are due to its being a neutral, mixed-valent species
The following **Cu_4O_2** complexes show a *side-on* coordination of the peroxo ligand within the binuclear complex units.			
bpmp[37]	387 (6850) 587 (370)	DCM	$[(bpmp)_2Cu_4(\mu_4\text{-}O)(OMe)_2]^{2+}$
Krebs *et al.*[37, 38]	ca. 390 (9500)[b, c] ca. 580 (600)[b, c]	DCM	phenolate/O_2^{2-} → Cu(II)-CT (390 nm), O_2^{2-} → Cu(II)-CT (580 nm); [b]observed under basic reaction conditions; [c]ligands closely related to bpmp
pzdien[39]	360 (3100) 631 (260)	EtCN	$[(pzdien)_2Cu_4(\mu_4\text{-}O_2)(OH)_2]^{2+}$; O_2^{2-} → Cu(II)-CT (360 nm), dd transition (630 nm); crystal structure: $d_{O\text{-}O}$ = 1.50 Å

5.2. Expectations and assignments based on TDDFT

Table S7: Overview of the theoretical obtained absorption features for the **bdpdz** (**1a**) and **bdptz** (**1b**) systems using TDDFT.

Model system	Cu_2O		
	C_3H_6O[a]	CH_3CN	Assignment[b]
1a (bdpdz) λ /nm (ε / $M^{-1}cm^{-1}$)	**390**	367, 357 + 388, 344 (**351**)	**LLCT (O-Cu-acetone)**; LLCT (O-Cu-py, pdz) + MLCT (Cu-pdz)
	417+**451** (**431**)	**425**	**d-d transition + LLCT (O-Cu-pdz)**; LLCT (O-Cu-pdz)
	552, 701+558 (**554**+**701**)	**510**+586 (540)	**d-d transition + LLCT (O-Cu-pdz)**; **d-d transition**
1b (bdptz) λ /nm (ε / $M^{-1}cm^{-1}$)	374, 390 (**380**)	379,378+362+341 ((**379**+**355**)/2 = **361**)	**LLCT (O-Cu-py, ptz)**
	414, 449 (**434**)	410, 415, 418 (**415**)	**d-d transition**
	586, 568+567 (**572**)	**643**, **536** (**560**)	**LLCT (O-Cu-ptz)**

General remarks: DFT: RI-B3LYP/def2-TZVP(-f). LMCT: ligand-to-metal charge transfer. MLCT: metal-to-ligand charge transfer. LLCT: ligand-to-metal charge transfer with participation of the phthalazine/pyridazine spacer (and pyridine moieties) since electron density is forwarded to them – causing a ligand-to-ligand charge transfer from the O-atom of the **Cu_2O** to part(s) of the ligand backbone (LMCT from O^{2-} to Cu(II) and MLCT from Cu(II) to phthalazine/pyridazine (and pyridine): LMCT→MLCT = LLCT). (XXX) = mean values; as average of the individual values depending on their intensity (weighted average).
[a] Compared to the obtained spectroscopic data, we assign that acetone fits best and therefore seems to be the best theoretical model describing the real system. [b] Assignments in the following order: acetone; acetonitrile.

5.3. Investigating the interconversion between Cu_4O_2 and Cu_2O

Based on the spectral changes observed and on the obtained data, we anticipate that the spectrum observed at 183 K does not originate from a **Cu_2O** complex, but rather from a different, initially generated species, a peroxo complex. Consequently, we assume the reaction sequence shown in Scheme S2 below.

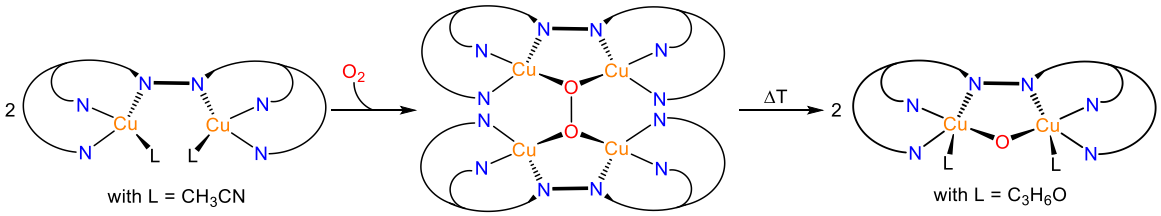

Scheme S2: Assumption of an irreversible equilibrium – breaking the dioxygen O-O bond. Temperature-dependent equilibrium between the tetranuclear, mixed-valent μ_4-peroxo complex (**Cu_4O_2**) and the dinuclear mono-μ-oxo species (**Cu_2O**). Once the O-O bond is broken, the reverse reaction, the formation of an O-O bond, doesn't take place since the energy barrier is not conquerable and the **Cu_2O** site is entropically more favorable. The aromatic rings have been omitted for clarity and simplified by the *N* donor atoms.

A reaction pathway for formation of the **Cu_2O** complex thus would proceed through the following steps: (i) dissolving the precursor species in acetone leading to substitution of the bound acetonitrile ligands by acetone, (ii) upon reaction with dioxygen at low temperature a tetranuclear, mixed-valent **Cu_4O_2** species is formed whereby two electrons delivered by two Cu(I) centers to bind O_2 as peroxo ligand, and finally (iii) increasing the temperature leads to homolytic O-O bond cleavage of the tetranuclear, mixed-valent μ_4-peroxo[Cu(I)/Cu(II)]$_2$ intermediate, generating the mono-μ-oxo species (Scheme S2). The last step occurs irreversibly as a thermally activated reaction (see below).

Assignment of the primary dioxygen adduct to a tetranuclear **Cu_4O_2** complex is supported by data of Davies and El-Sayed.[34]

If the solution containing the **Cu_2O** species of **1b**-OTf (Figure S20) is cooled again from -25 °C down to -90 °C, the absorption features assigned to the **Cu_4O_2** species do not re-appear but the spectrum of the **Cu_2O** complex is retained upon cooling, indicating that the considered transformation process shown in Scheme S2 is not reversible once the O-O bond is cleaved.

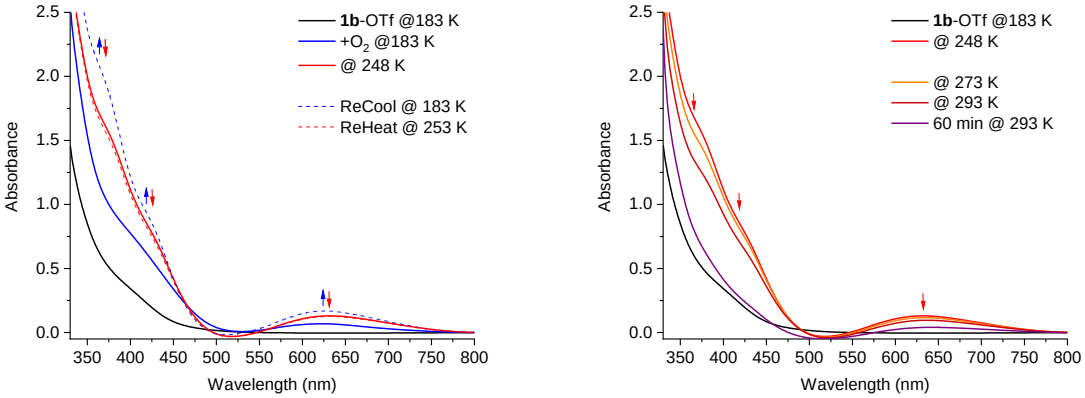

Figure S20: Investigating the temperature-dependent equilibrium with **1b**-OTf: **Left:** Once the **Cu_2O** complex is formed (red), upon cleavage of the O-O bond of the **Cu_4O_2** species (blue), the equilibrium is irreversible and thus the spectrum of the mono-μ-oxo species is retained after re-cooling (blue, dashed). Increasing the temperature to 253 K matches the identical spectrum for the **Cu_2O** obtained before at 248 K. **Right:** Increasing the temperature from 253 K to room temperature results in decomposition of the **Cu_2O** complex (decrease of the three characteristic bands; from red to orange to dark red). After 60 min at 293 K (violet) the absorption features associated with the **Cu_2O** motif are nearly vanished. l = 1cm.

Similar observations are made for **1a-PF_6** before and after reaction with dioxygen at -90 °C (183 K) and -40 °C (233 K) (see Figure S21).

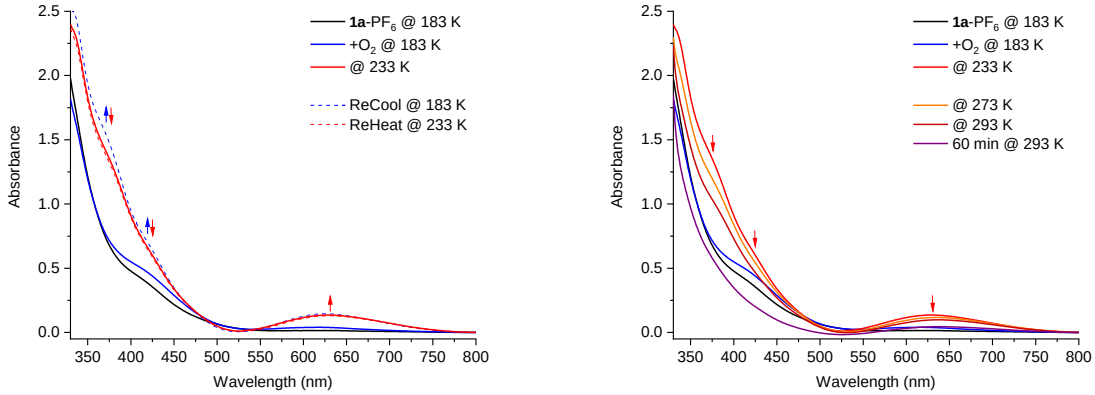

Figure S21: UV/Vis spectra of **1a**-PF_6. **Left:** Once the **Cu_2O** complex is formed (red), upon cleavage of the O-O bond of the **Cu_4O_2** species (blue), the equilibrium is irreversible and thus the spectrum of the mono-μ-oxo species is retained after re-cooling (blue, dashed). Increasing the temperature to 233 K matches the identical spectrum for the **Cu_2O** obtained before at 233 K. **Right:** Increasing the temperature from 233 K to room temperature results in decomposition of the **Cu_2O** complex (decrease of the three characteristic bands; from red to orange to dark red). After 60 min at 293 K (violet) the absorption features associated with the **Cu_2O** motif are nearly vanished. l = 1cm.

6. Resonance Raman Spectroscopy using Dioxygen

6.1. Spectroscopic data and calculated vibrations

Table S8: Overview of the obtained Data for the measured frequencies and DFT-expected vibrations for the **Cu_2O** and **Cu_4O_2** species of the **bdpdz** (**1a**) and **bdptz** (**1b**) systems as well as available vibrational data for known model systems.

Vibrational mode Cu_2O	DFT-calculated vibrations[a]			Experimental data for Cu_2O		
	ν ($\Delta^{18}O_2$) / cm^{-1}	Assignment[b]				
	1a (bdpdz)			**1a (bdpdz)**		
ν_1	245 (6)	out-of-plane	oop	**DFT**[a]	**rR** (PF_6)	**rR** (OTf)
ν_2	437 (19)	A_1	*s*Cu-O	$_{s}$437 (19)	-	-
ν_3	563 (35)	B_2	*as*Cu-O	$_{as}$563 (35)	629 (23)	619 (11)
	1b (bdptz)			**1b (bdptz)**		
ν_1	235 (2)	out-of-plane	oop	**DFT**[a]	**rR** (PF_6)	**rR** (OTf)
ν_2	444 (16)	A_1	*s*Cu-O	$_{s}$444 (16)	-	-
ν_3	587 (29)	B_2	*as*Cu-O	$_{as}$587 (29)[c]	623 (20)	619 (8)

General remarks: DFT: RI-PBE-D3(BJ)/def2-SVP.
[a] Based on the assignment that acetone is the coordinating solvent. Values without acetone or with acetonitrile can be found in Section 6.2, Table S9. [b] The assignment is based on the following assumption: idealized symmetry of the **Cu_2O** unit is given by the point group C_{2v}. Note: ν_3 is observed. [c] There are two frequencies corresponding to the $vas_{Cu\text{-}O}$, in particular, 568 and 558 cm^{-1} which can be assigned as the vibration upon isotope exchange (^{16}O: 587 cm^{-1}) – meaning Δ = 19 or 29 cm^{-1}. In addition, the bound acetone molecules participate in this mode. This effect is more expected for the phthalazine system and this might be the main reason why the Cu-O assigned peak is a plateau in case of **1b** and a more defined peak in the spectra of **1a** (see below).

Vibrational mode Cu_4O_2	DFT-calculated vibrations[a]			Experimental data for Cu_4O_2		
	ν ($\Delta^{18}O_2$) / cm^{-1}	Assignment[b]				
ν_1	121 (5)	out-of-plane	*s*[c]	**1a (bdpdz)**		
ν_2	195 (4)	out-of-plane	*as*[c]			
ν_3	375 (16)	A_1	*s*Cu-O[d]	**DFT**[a]	**rR** (PF_6)	**rR** (OTf)
ν_4	458 (21)	B_3	*s*Cu-O			
ν_5	523 (28)	B_2	*as*Cu-O	$_{as}$523 (28)	607 (14)	-
ν_6	854 (50)	A_1	O-O	$_{OO}$854 (50)	854 (62)	-
ν_1	113 (4)	out-of-plane	*s*[c]	**1b (bdptz)**		
ν_2	189 (5)	out-of-plane	*as*[c]			
ν_3	381 (16)	A_1	*s*Cu-O[d]	**DFT**[a]	**rR** (PF_6)	**rR** (OTf)
ν_4	477 (25)	B_3	*s*Cu-O			
ν_5	534 (27)	B_2	*as*Cu-O	$_{as}$534 (27)	607 (16)	604 (8)
ν_6	849 (49)	A_1	O-O	$_{OO}$849 (49)	854 (52)	855 (57)

General remarks: DFT: RI-PBE-D3(BJ)/def2-SVP.
[a] Based on the assignment without any coligands like acetone or acetonitrile. **1a**: $d_{O\text{-}O}$ = 1.412 Å and **1b**: $d_{O\text{-}O}$ = 1.414 Å. [b] The assignment is based on the following assumption: idealized symmetry of the **Cu_4O_2** unit is given by the point group D_2. Note: ν_5 and ν_6 are observed. [c] out-of-plane. [d] perpendicular to the higher energetic symmetric Cu-O vibration.

Cu_2O-complexes	$\nu_{Cu\text{-}O}$ ($\Delta^{18}O_2$) / cm^{-1}	Solvent	Special remarks
Cu-ZSM-5[26, 27]	*δ*: 237 (3) *vs*: 456 (8) *vas*: 870 (40)	solid	zeolite; after activation with dioxygen
Xanthdim[28]	593 (25) 612 (14)[c] 640 (18)[c]	THF	[c]only observed with λ_{ex} = 647 nm; $[(CuOCu)]_{1,2,n}$
FurNeu[29]	*δ*: 236 *vs*: 565 *vas*: 619	CH_3CN	calculated frequencies; B3LYP/def2-TZVP; $[FurNeu(Cu_2(\mu\text{-}O))](OTf)_2$
ENCA[30]	555[d]	$PhNO_2$	[d]infrared spectroscopy data; $[((ENCA)CuX)_4O_2]$; X = Cl, Br
DENC[31]	580[d]	DCM	[d]see above; $[((DENC)CuX)_4O_2]$; X = Cl, Br
TEED[32] with μ-Br	600[d]	DCM	[d]see above; $[((TEED)Cu)_2(\mu\text{-}Br)_2(\mu\text{-}O)]$

TEED[33, 34] with μ-Cl	627 701	DCM	bands are not clearly attributable; [((TEED)Cu)$_2$(μ-Cl)$_2$(μ-O)]
	ν_{O-O}: 822	DCM	mixed-valent tetranuclear peroxo species (Cu_4O_2); satellite at 842 cm^{-1}
Cu_4O_2-complexes	**ν_{Cu-O} and ν_{O-O} ($\Delta^{18}O_2$) / cm^{-1}**	**Solvent**	**Special remarks**
TEED[32, 33, 34] with μ-Cl	ν_{O-O}: 822	DCM	mixed-valent tetranuclear peroxo species (Cu_4O_2); satellite at 842 cm^{-1}
The following **Cu_4O_2** complexes show a *side-on* coordination of the peroxo ligand within the binuclear complex units.			
bpmp[37]	ν_{O-O}: 878 (37)[e]	DCM	[Cu_4(bpmp)$_2$(μ_4-O_2)(OMe)$_2$-(ClO_4)]ClO_4; d_{O-O} = 1.453(4) Å; [e]ν_{Cu-O}: 353 (6) cm^{-1} + an additional feature around 600 cm^{-1} (no assignment)
Krebs *et al.*[37, 38]	ν_{O-O}: 880-900[e, f]	DCM	[f]ligands closely related to bpmp
Fe_4O_2[40]	ν_{O-O}: 853	THF	[$Fe_6(O)_2O_2(O_2CPh)_{12}(OH_2)_2$]; d_{O-O} = 1.480(12) Å

Vibrational analysis: DFT calculations performed for the **Cu_2O** complexes predict two Cu-O vibrations of A_1 and B_2 symmetry along with a lower-frequency, out-of-plane vibration (ν_1) (cf. Table S8). Based on the frequency, the observed mode is assigned as the B_2 mode predicted at 563 cm^{-1} (ν_3; Δ = 35 cm^{-1}; cf. Table S8) for **1a**-PF_6, whereas the Cu-O mode of A_1 symmetry predicted at 437 cm^{-1} (ν_2; Δ = 19 cm^{-1}; cf. Table S8) does not appear to have a significant intensity (see below). The symmetry labels of the theoretically expected vibrations are based on an idealized C_{2v} symmetry for the **Cu_2O** moiety; these modes are shown in the figure below.

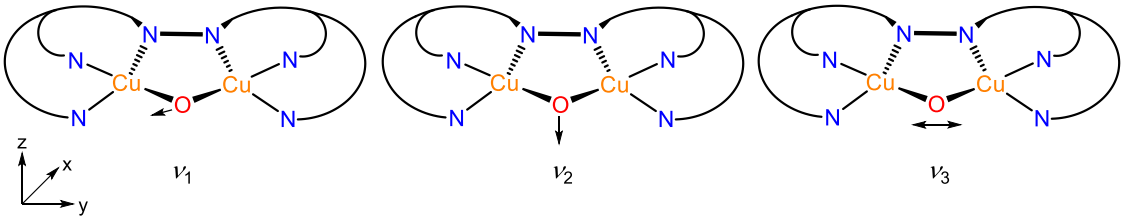

Scheme S3: Schematic representation of the expected vibration modes for the Cu_2O species. From left to right: the out-of-plane vibration (ν_1) is depicted on the left; the symmetric Cu-O stretch (ν_2) is shown in the middle and the antisymmetric Cu-O mode (ν_3) is illustrated on the right side. DFT: RI-PBE-D3(BJ)/def2-SVP. The aromatic rings have been omitted for clarity and simplified by the *N* donor atoms.

Cu_2O core: ν_2 and ν_3 are referred to as symmetric and antisymmetric Cu-O stretch, respectively, reflecting their transformation behavior with respect to the vertical mirror plane of the **Cu_2O** core (cf. Scheme S3). The fact that the symmetric Cu-O stretch corresponding to ν_2 is not observed can be explained by assuming that the oxo → Cu(II) CT transition is localized (shifting an electron from the bound O^{2-} to one of the two Cu(II) centers), similar to the Raman spectrum of oxy-hemocyanin.[41] The excited state thus exhibits a distortion which corresponds to a displacement along the antisymmetric Cu-O stretching vibration, and only one strong resonance-enhanced Raman feature is expected that corresponds to the antisymmetric Cu-O mode.[41]

Cu_4O_2 core: Upon reaction of e.g. **1a**-PF_6 with dioxygen at -80 °C (193 K) two characteristic isotope-sensitive peaks emerge in the resonance Raman spectrum. Based on the peroxo-core of the assumed **Cu_4O_2** species the peak at 854 cm^{-1} is attributed to the O-O stretch (ν_6) and the peak at 607 cm^{-1} to the Cu-O stretching vibration (ν_5). Upon ^{18}O substitution, the scattering intensity at the position of the O-O stretch is significantly reduced and the peak is presumably shifted to a position where it is masked by the large solvent peak at 792 cm^{-1}. These findings are compatible with theoretical values for $\nu_{O-O} \equiv \nu_6$ (854 cm^{-1}; A_1 symmetry) and Δ $^{16}O_2$–$^{18}O_2$ (50 cm^{-1}; cf. Table S8). Moreover, an ^{18}O isotope shift of the 607 cm^{-1} peak to 593 cm^{-1} (Δ = 14 cm^{-1}) is observed. Based on its frequency, this mode is assigned to a Cu-O mode of B_2 symmetry predicted at 523 cm^{-1} (ν_5; Δ = 28 cm^{-1};

cf. Table S8). The symmetry labels of the two mentioned vibrations are based on an idealized D_2 symmetry for the **Cu_4O_2** moiety. These modes are shown in Scheme S4 which also includes two Cu-O modes of B_3 and A_1 symmetry predicted at 458 cm^{-1} (ν_4; Δ = 21 cm^{-1}) and 375 cm^{-1} (ν_3; Δ = 16 cm^{-1}), respectively, as well as two lower-frequency, out-of-plane vibrations (ν_1 and ν_2; cf. Table S8). For simplicity we refer to ν_4 and ν_5 as symmetric and antisymmetric Cu-O stretch, respectively, corresponding to their transformation behavior with respect to a rotation around the molecular y axis of the **Cu_4O_2** core.

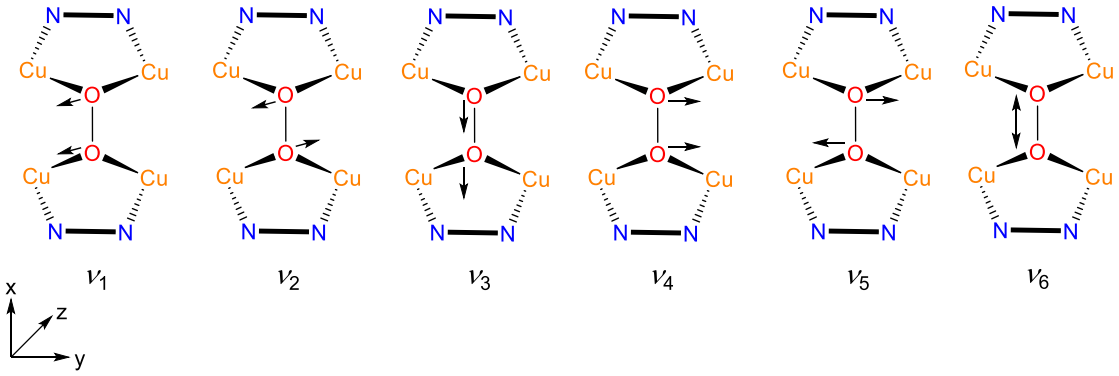

Scheme S4: Schematic representation of the expected vibration modes for the Cu_4O_2 species. From left to right: the two out-of-plane vibrations (ν_1 and ν_2) are depicted on the left; two symmetric Cu-O stretches perpendicular to each other (ν_3 and ν_4) and an antisymmetric Cu-O mode (ν_5) are shown in the middle; the O-O vibration (ν_6) is illustrated on the right side ($d_{O\text{-}O}$ changes during this vibration). DFT: RI-PBE-D3(BJ)/def2-SVP. The aromatic rings have been omitted for clarity and simplified by the *N* donor atoms.

6.2. Theoretical spectra derived from DFT

Table S9: Overview of the theoretical obtained Raman features for the **bdpdz** (**1a**) and **bdptz** (**1b**) systems using DFT.

Vibration mode ($\Delta^{18}O_2$) / cm^{-1}	**Cu_2O**			**Cu_4O_2**	
	naked	**acetone**	**CH_3CN**	**naked**	**acetone**[c]
1a (bdpdz)					
$\nu s_{Cu\text{-}O}$	509 (18)	**437 (19)**	418 (15)	**458 (21)**; 375 (16)[a]; 121 (5)[b]	N.A.
$\nu as_{Cu\text{-}O}$	660 (41)	**563 (35)**	577 (27)	**523 (28)**; 195 (4)[b]	N.A.
$\nu_{O\text{-}O}$	N.A.	**N.A.**	N.A.	**854 (50)**	N.A.
1b (bdptz)					
$\nu s_{Cu\text{-}O}$	481/490 (15/24)	**444 (16)**	428 (16)	**477 (25)**; 381 (16)[a]; 113 (4)[b]	N.A.
$\nu as_{Cu\text{-}O}$	596 (29)	**587 (29)**	582 (28)	**534 (27)**; 189 (5)[b]	N.A.
$\nu_{O\text{-}O}$	N.A.	**N.A.**	N.A.	**849 (49)**	N.A.

General remarks: DFT: RI-PBE-D3(BJ)/def2-SVP.
[a] Perpendicular to the higher energetic symmetric Cu-O vibration. [b] Out-of-plane. [c] Possibly only one acetone molecule is coordinated; the second acetone is too far away from any of the copper centers (d > 3.7 Å). Since this situation is quite comparable to **Cu_4O_2** without any acetone, we decided to perform the frequency calculation without any solvent molecule attached.

Assignment for symmetric vs. antisymmetric Cu-O mode

The assignment for symmetric vs. antisymmetric mode for the observed Cu-O vibration of the **Cu_2O** core is based on Ling *et al* (see above).[41]

6.3. Spectra with fit components and implications for intrinsic features

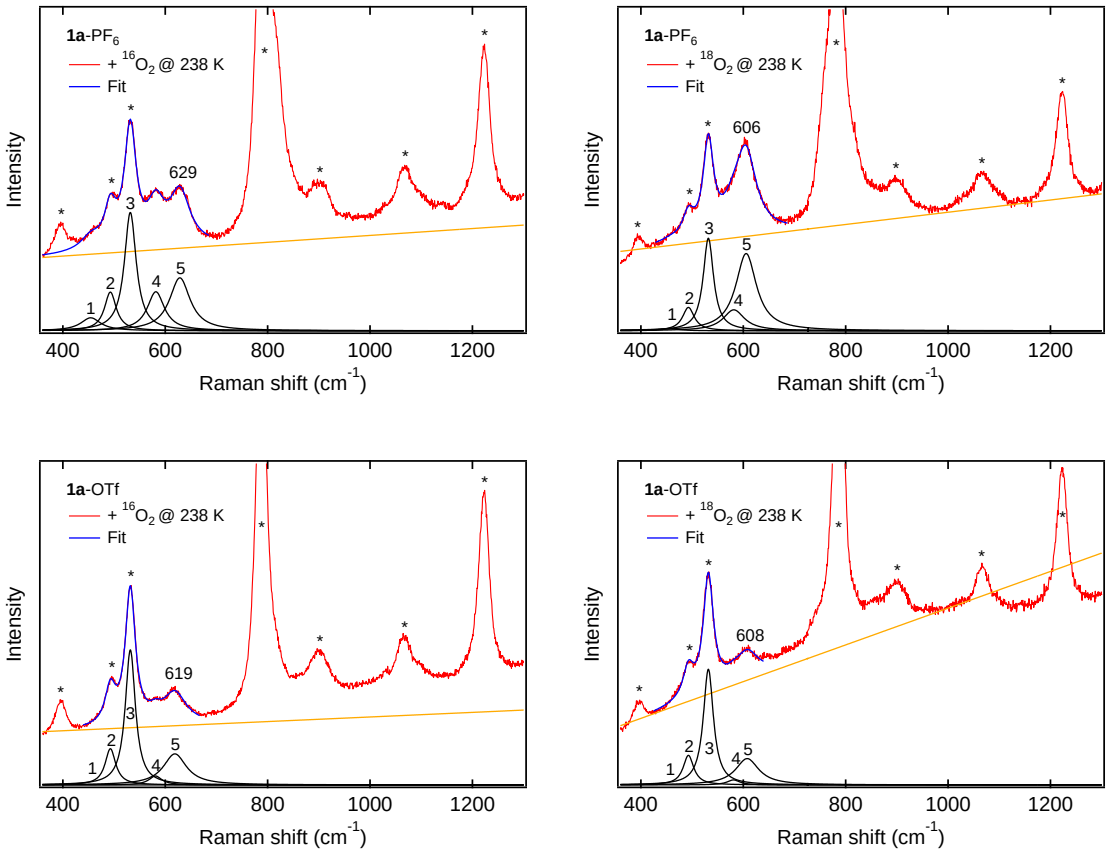

Figure S22: Resonance Raman spectra of 1a-PF_6 and 1a-OTf with fit components at 238 K. Top: 1a-PF_6 after the reaction with $^{16}O_2$ (left) and after the reaction with $^{18}O_2$ (right). **Bottom: 1a**-OTf after the reaction with $^{16}O_2$ (left) and upon reaction with $^{18}O_2$ (right). The peaks notated with 1-3 are solvent signals; peak 5 is assigned as the Cu-O vibration of the **Cu_2O** complex and the peak around 580 cm^{-1} (Δ = 0 cm^{-1}) = peak 4 is attributed to vibrations of the bound acetone coligands. The asterisks mark solvent signals of acetone. The laser excitation wavelength was 393 nm.

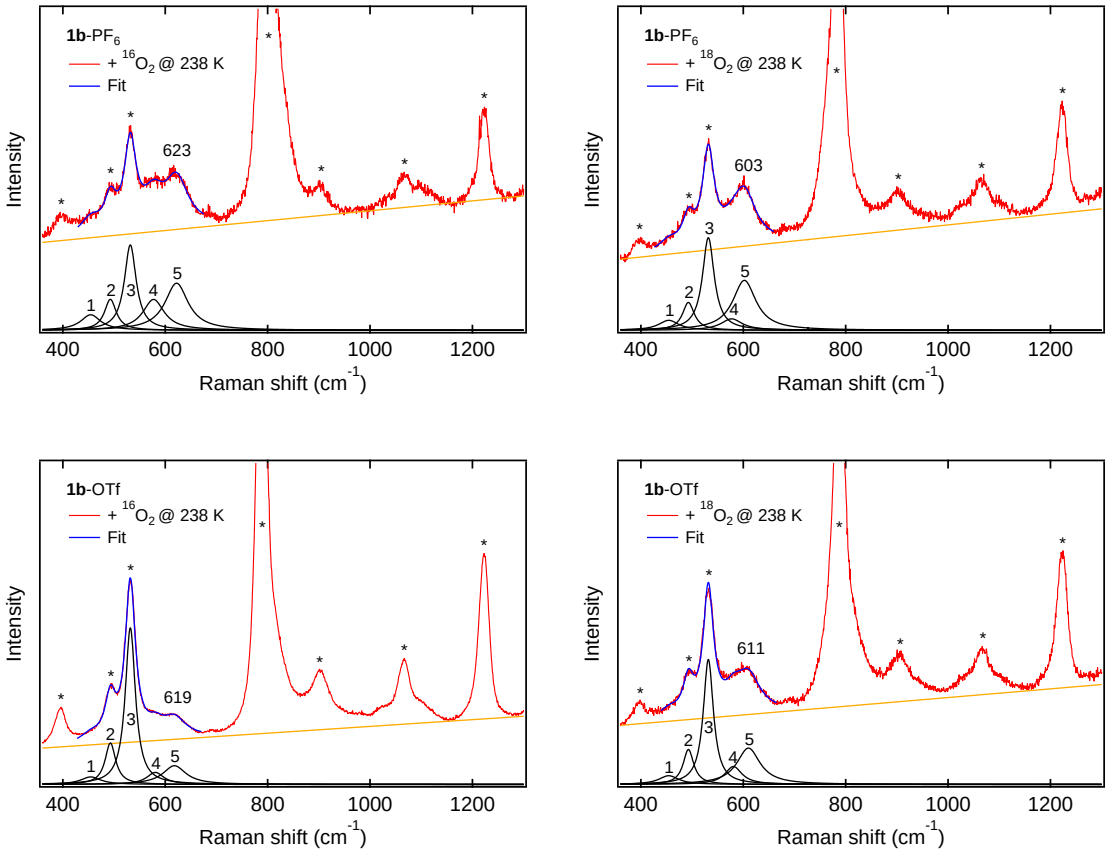

Figure S23: Resonance Raman spectra of 1b-PF_6 and 1b-OTf with fit components at 238 K. Top: 1b-PF_6 after the reaction with $^{16}O_2$ (left) and after the reaction with $^{18}O_2$ (right). **Bottom: 1b**-OTf after the reaction with $^{16}O_2$ (left) and upon reaction with $^{18}O_2$ (right). The peaks notated with 1-3 are solvent signals; peak 5 is assigned as the Cu-O vibration of the **Cu_2O** complex and the peak around 580 cm^{-1} (Δ = 0 cm^{-1}) = peak 4 is attributed to vibrations of the bound acetone coligands. The asterisks mark solvent signals of acetone. The laser excitation wavelength was 393 nm.

The peaks notated with 1-3 are solvent signals; peak 5 is assigned as the Cu-O vibration of the **Cu_2O** complex and the peak around 580 cm^{-1} (Δ = 0 cm^{-1}) = peak 4 is attributed to vibrations of the bound acetone coligands (vide infra; Section 6.5, Table S10) effecting the shape of the Cu-O peak in the ^{16}O spectra (plateau vs. defined sharp peak, see Figures S22, S23 and S24, right).

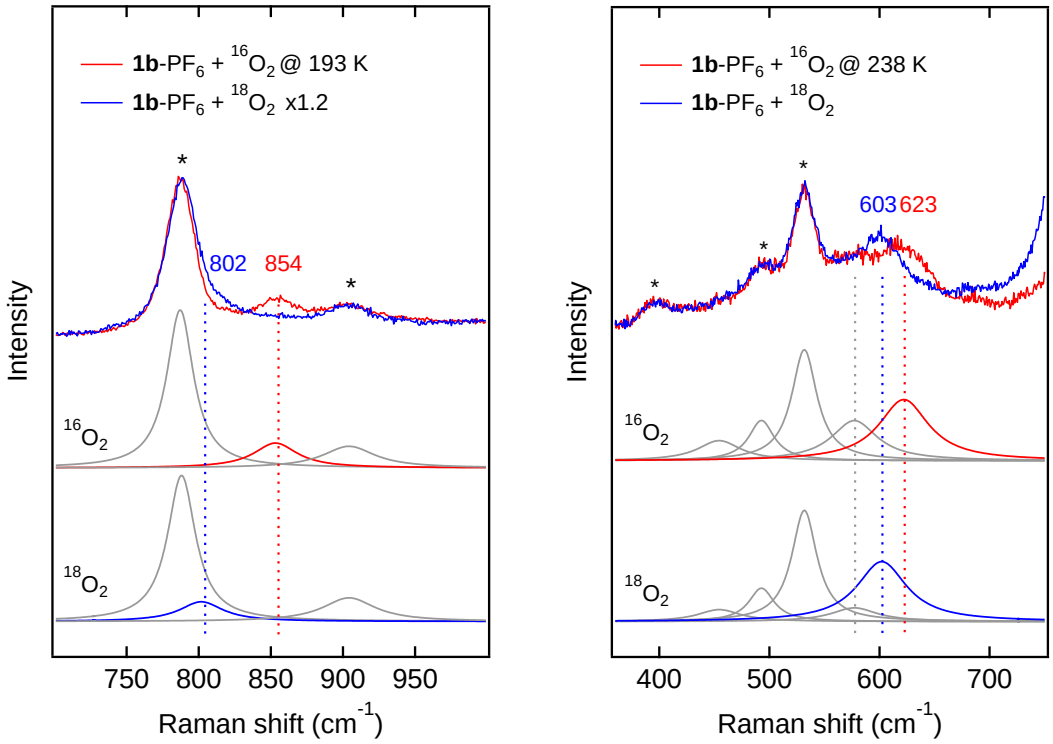

Figure S24: Resonance Raman spectra of 1b-PF_6 with fit components in more detail. Left: 1b-PF_6 after the reaction with dioxygen at 193 K (top); $^{16}O_2$ (middle) and upon reaction with $^{18}O_2$ (bottom) at 193 K. **Right: 1b**-PF_6 after the reaction with O_2 at 238 K (top); $^{16}O_2$ (middle) and upon reaction with $^{18}O_2$ (bottom) at 238 K. The asterisks mark solvent signals of acetone. The laser excitation wavelength was 393 nm.

Based on the peroxo-core of the assumed **Cu_4O_2** species the peak at 854 cm^{-1} is attributed to the O-O stretch (Figure S24, left; red). Upon ^{18}O substitution, the scattering intensity at the position of the O-O stretch is significantly reduced (Figure S24, left; blue) and the peak is doubtless shifted to a position where it is – at least partially – masked by the intense solvent peak at around 800 cm^{-1}. The shown stacked spectra above demonstrate clearly that the attributed shift is correct and indeed necessary to fit the experimentally observed spectrum. This is also the case for **1a**.

6.4. Spectral feature deriving from decomposition of the precursor

The precursor decomposes upon increasing the temperature from 193 K to 238 K (comparing cold and warm precursor spectra), which is obvious since the shoulder around 800 cm^{-1} gets broader and the shape is more asymmetric at higher temperature (= intrinsic precursor feature).

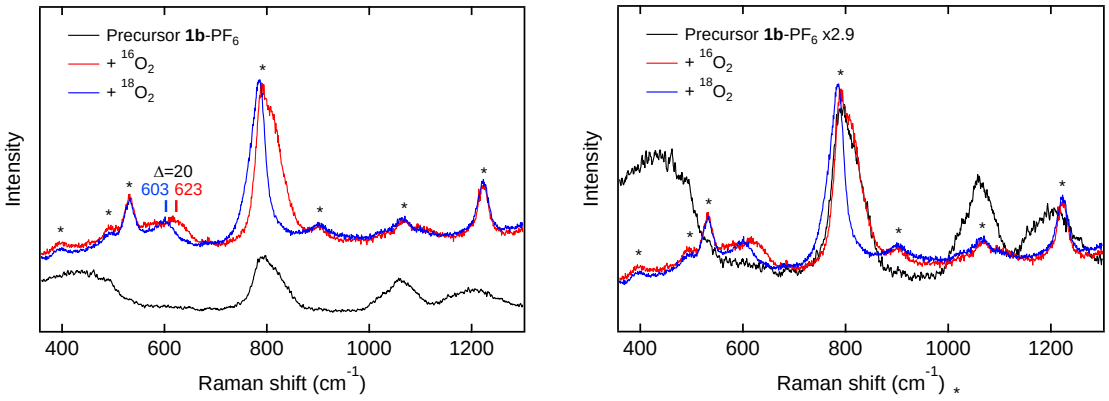

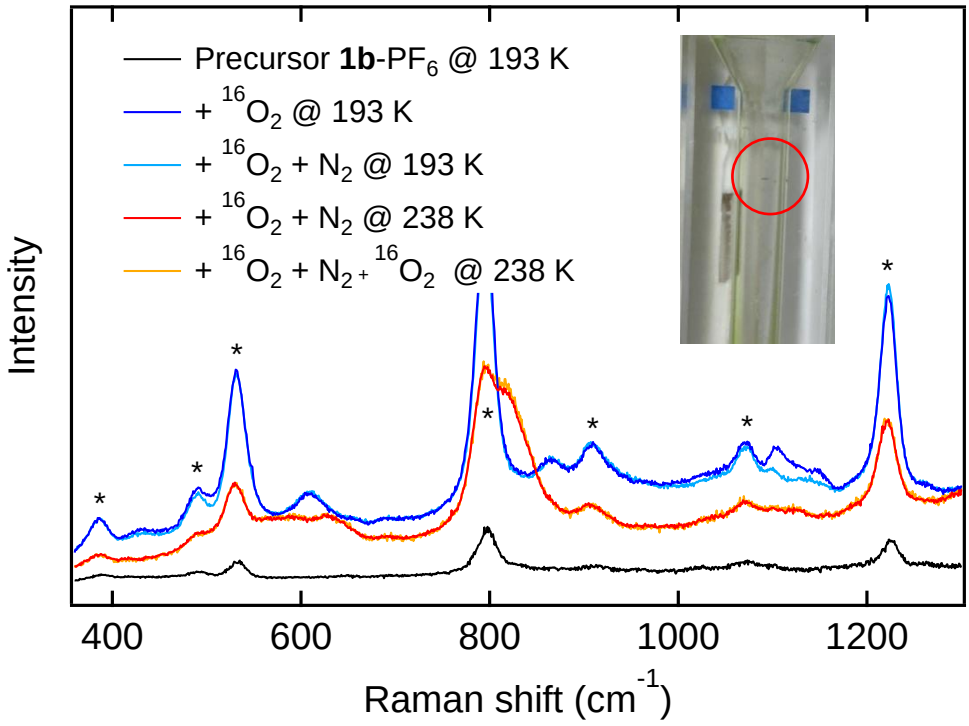

Figure S25: Top, left: Resonance Raman spectra of **1b**-PF_6 before (black) and after the reaction with $^{16}O_2$ (red) and $^{18}O_2$ (blue) at 238 K. The 623 cm^{-1} feature corresponds to the Cu-O vibration of the mono-μ-oxo motif. **Top, right:** The spectra represent an **adjusted intensity of the precursor** (black) to compare the width and shape of the solvent/precursor feature around 800 cm^{-1}. The precursor spectrum is rescaled by factor 2.9 to compare precursor and **Cu_2O** spectra. The asymmetric broad shape is most likely caused due to photo decomposition in combination with increasing temperatures (not observed at 193 K). **Bottom: Control experiment** to check if excess of dioxygen/removed excess of dioxygen is closely related to the observation of the broad shape of the peak around 800 cm^{-1}. As a result, the effect is negligible and thus the broad shape is an intrinsic feature of the precursor complex (ligand framework). **Inset:** The cuvette shows the burn-in of the complex after warming to 238 K and laser irradiation. The asterisks mark solvent signals of acetone. The laser excitation wavelength was 393 nm.

Therefore, this intrinsic precursor feature arising at higher temperatures is most likely caused due to photo decomposition in combination with thermal damage induced by laser radiation; using a cooled wire-guided jet would help to overcome this problem and thus this is one of the planned further investigations.[42]

On the other hand, the peak around 800 cm^{-1} shows a shoulder on the right side upon reaction with $^{16}O_2$ and on the left side after exposure to $^{18}O_2$ (see Figure S25). This shifting feature could possibly be assigned as O-O stretch of a **Cu_2O_2** species which could be a conceivable decomposition product of the tetranuclear μ_4-peroxo species upon increasing the temperature from 193 K (-80 °C) to 238 K (-40 °C). Further evidence comes from cryo-UHR-ESI mass spectrometry. The following figures show the mass spectra of such a μ-1,1-peroxo species **Cu_2O_2**.

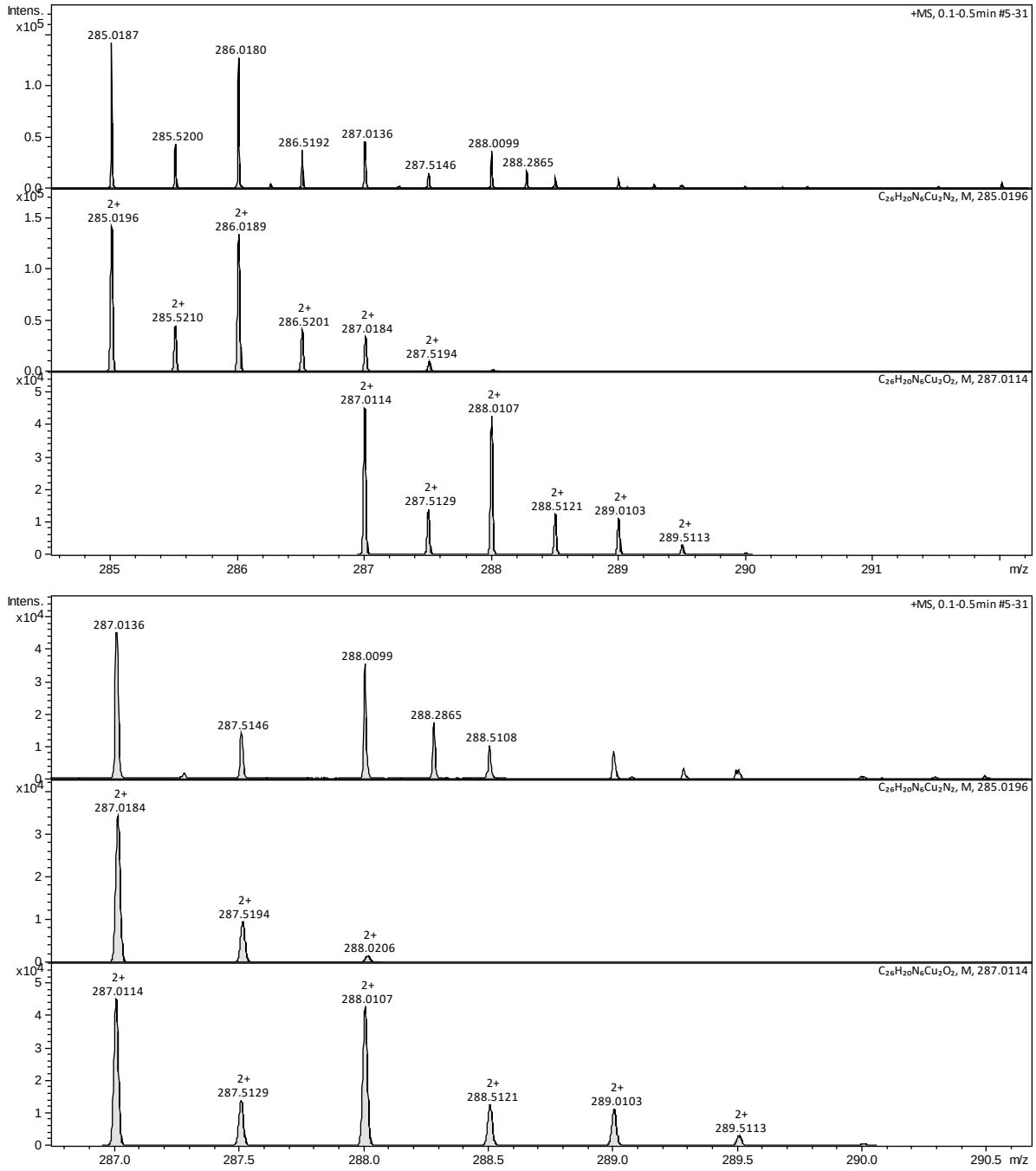

Figures S26: Cryo-UHR-ESI mass spectra of **1a** after reaction with dioxygen at -40 °C. **Top:** The isotopic pattern and corresponding *m/z* value resemble the simulated spectrum for the **Cu_2O_2** species which might be a possible decomposition product of the tetranuclear species upon increasing the temperature. But the corresponding μ-N_2 dicopper(I) species fits even better with the experimentally obtained spectrum than the presumed **Cu_2O_2** complex. **Bottom:** Zoom.

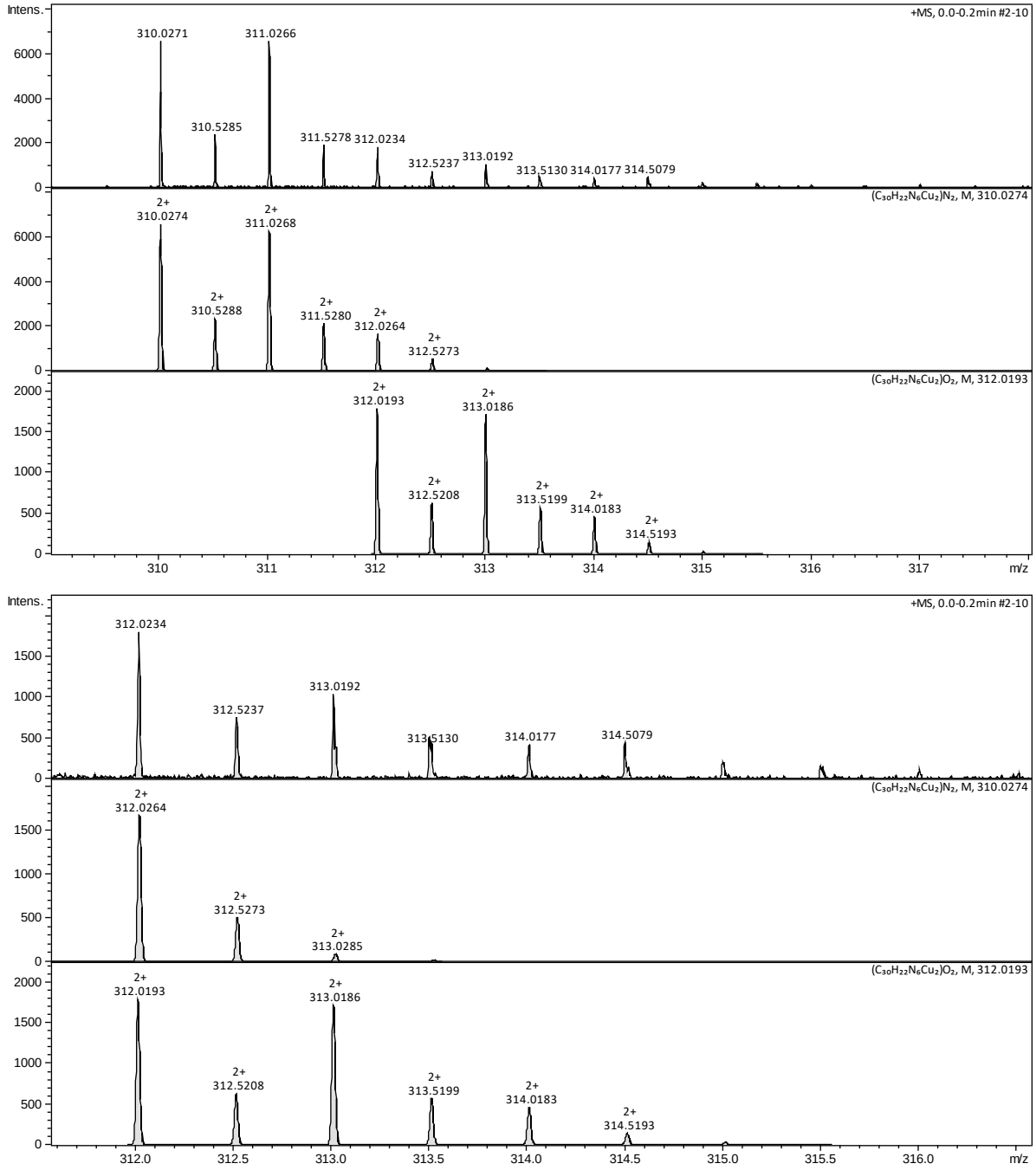

Figure S27: Cryo-UHR-ESI mass spectra of **1b** after reaction with dioxygen at -40 °C. **Top:** The isotopic pattern and corresponding *m/z* value resemble the simulated spectrum for the $\mathbf{Cu_2O_2}$ species, but the corresponding μ-N_2 dicopper(I) species fits better with the experimentally obtained spectrum than the presumed $\mathbf{Cu_2O_2}$ complex. **Bottom:** Zoom.

However, as can be seen from the spectra above (Figures S26 and S27), the experimental spectra show more μ-N_2 dicopper(I) species of **1a** and **1b**, respectively, than of the assumed decomposition product ($\mathbf{Cu_2O_2}$). This might be a first evidence for excluding this species.

Furthermore, the resonance Raman spectra of the reaction with N_2O showed a comparable and almost similar feature around 800 cm^{-1} (see Figure S28). Here, a tetranuclear peroxo species cannot exist and therefore, the μ-1,1-peroxo species $\mathbf{Cu_2O_2}$ can be ruled out as a reason for the broad asymmetric feature around 800 cm^{-1}.

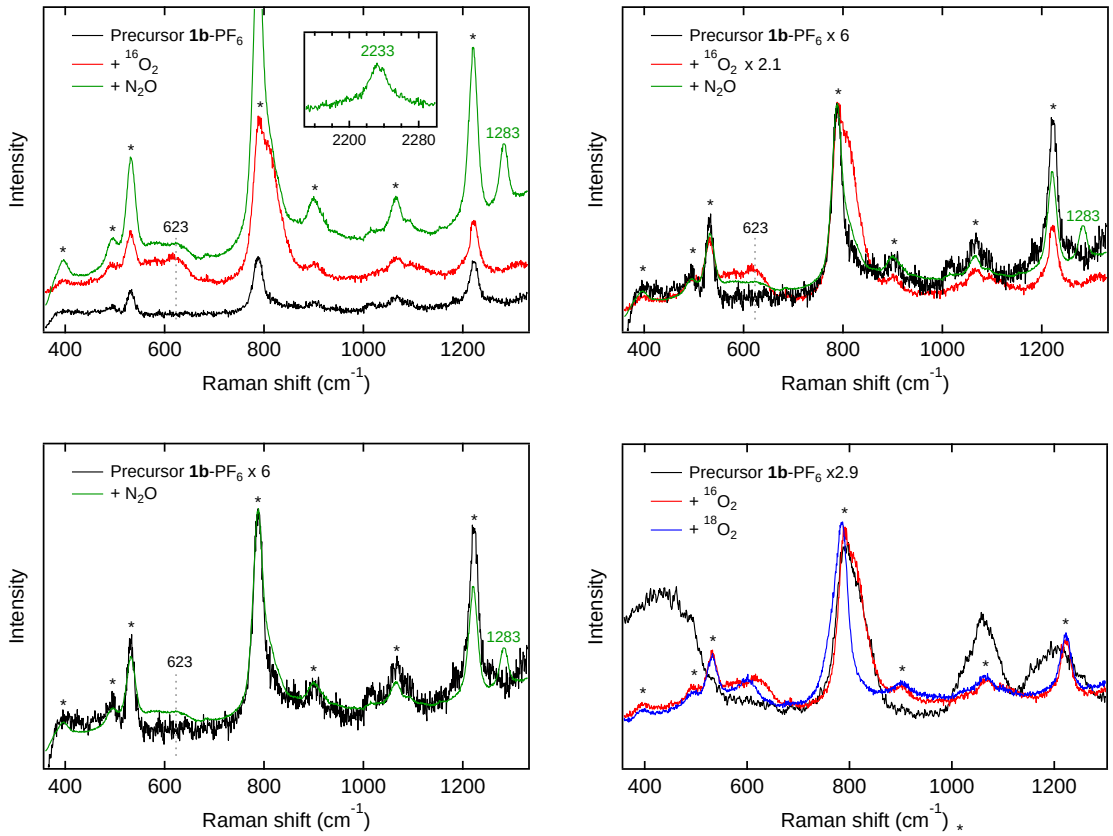

Figure S28: rRaman spectra of **1b**-PF_6 before (black) and after the reaction with dioxygen (red; blue: $^{18}O_2$) and upon reaction with nitrous oxide (green). The precursor spectrum is rescaled for clarity (indicated by the factor behind the precursor; except in the figure on the top, left). **Top, left:** The same peak at 623 cm^{-1} is observed for the **Cu_2O** species after reaction with O_2 or with N_2O. **Top, right** and **bottom, left:** Rescaled precursor spectrum indicating that the broad peak around 800 cm^{-1} is comparable with and without nitrous oxide. **Bottom, right:** Demonstrating that only the precursor spectrum obtained before reaction with O_2/N_2O can be used for comparison. Otherwise (as shown in the spectra on the top, right) the curve shape seems to be completely different comparing precursor and the spectrum obtained after reaction with O_2. The laser excitation wavelength was 393 nm.

Conclusively, most likely, the photo/thermal decomposition of the precursor seems to be the reason for this feature and it is supposed to be an intrinsic property of the used ligand scaffold/complex.

6.5. Spectral feature deriving from bound acetone

Upon reaction with dioxygen the formed complexes reveal another interesting feature in their resonance Raman spectra. Maybe this feature can be also fitted into the corresponding precursor feature but unfortunately, because of the problem mentioned above, measuring the precursor at higher temperature leads to spectra with lower quality (broad intense feature around 800 cm^{-1}) and in addition, the bound acetonitrile coligands in the dicopper(I) complexes seem to be quite stable under anaerobic conditions (the bound acetonitrile can be exchanged by acetone; this process is enforced by thermal activation upon warming up to 238 K – being another reason for the broad peak around 800 cm^{-1} since the bound acetone shows also vibrations in this region).

There is always a peak around 580 cm^{-1} in the spectra of the **Cu_2O** species of **1a** and **1b** which does not shift upon isotope exchange (see Figures S22 and S23 above and cf. Table S10). This effect is even stronger for the phthalazine model systems, resulting in a broad peak/plateau instead of a defined sharp peak as observed for the pyridazine model systems. This intrinsic feature can be attributed to the bound acetone coligands and it is obviously an intrinsic feature of the mono-μ-oxo complex (and maybe as well of the precursor complex), but not in case of the peroxo species (no or maybe only one acetone molecule is bound in the tetranuclear unit; therefore this feature is not expected for the **Cu_4O_2** complex). Moreover, there are two frequencies predicted by DFT corresponding to the $vas_{Cu\text{-}O}$ vibration (^{16}O: 587 cm^{-1}) in the **Cu_2O** complex of **1b** upon isotope exchange, in particular, 568 and 558 cm^{-1} (Δ = 19 or 29 cm^{-1}, respectively). In addition, the bound acetone molecules participate in this mode. This effect is more expected for the phthalazine system (and consequently only observed in the calculations of the **Cu_2O** complex of **1b**) and this might be the main reason why the Cu-O assigned peak at 587 cm^{-1} is a broad peak/plateau in case of **1b** (and a more defined peak in **1a**). The experimentally observed vibration corresponds to the peak at 623 cm^{-1} (Δ = 20 cm^{-1}). The DFT-predicted frequencies for additional vibrations attributed to bound acetone molecules in the **Cu_2O** complexes are listed in the table below (Table S10) and are in very good agreement with the experimentally observed peak around 580 cm^{-1}. In addition, the bound acetone causes also vibrations centered around 800 cm^{-1} (as well as the used ligand scaffold by itself, see above), strengthening the effect of the broad decomposition feature of the precursor mentioned above.

Table S10: Vibrations attributed to the bound acetone in the **Cu_2O** species of **1a** and **1b**.

Vibration mode ($\Delta^{18}O_2$) / cm^{-1}	**DFT Cu_2O-1a**	**Cu_2O 1a-PF_6/OTf**	**DFT Cu_2O-1b**	**Cu_2O 1b-PF_6/OTf**
Cu2-(O1)-O3	544 (3)	582 (0)/ 581 (0)	553 (6)	578 (0)/ 581 (0)
Cu1-(O1)-O2	554 (7)		561 (3)	
Cu1-O2	810 (0), 837 (0)	N.A.	805 (0), 844 (0)	N.A.
Cu2-O3	803 (0), 833 (0)		807 (0), 834 (0)	
General remarks: DFT: RI-PBE-D3(BJ)/def2-SVP. The used notation of the atoms corresponds to the numbers used in Section 9. (O1) means that the oxygen atom of the **Cu_2O** moiety participates in the vibration.				

6.6. Additional resonance Raman spectra

6.6.1. Measurements at 193 K: Characterization of the Cu_4O_2 species

Upon reaction of **1a**-PF_6 with dioxygen at -80 °C (193 K) two characteristic isotope-sensitive peaks emerge in the resonance Raman spectrum (Figure S29, left). Based on the peroxo-core of the assumed **Cu_4O_2** species the peak at 854 cm^{-1} is attributed to the O-O stretch (ν_6) and the peak at 607 cm^{-1} to the Cu-O stretching vibration (ν_5) (Figure S29, left; red). Upon ^{18}O substitution, the scattering intensity at the position of the O-O stretch is significantly reduced (Figure S29, left; blue) and the peak is presumably shifted to a position where it is masked by the large solvent peak at 792 cm^{-1}. These findings are compatible with theoretical values for $\nu_{O\text{-}O} \equiv \nu_6$ (854 cm^{-1}; A_1 symmetry) and $\Delta\ ^{16}O_2$–$^{18}O_2$ (50 cm^{-1}; cf. Table S8). Moreover, an ^{18}O isotope shift of the 607 cm^{-1} peak to 593 cm^{-1} (Δ = 14 cm^{-1}) is observed. Based on its frequency, this mode is assigned to a Cu-O mode of B_2 symmetry predicted at 523 cm^{-1} (ν_5; Δ = 28 cm^{-1}; cf. Table S8).

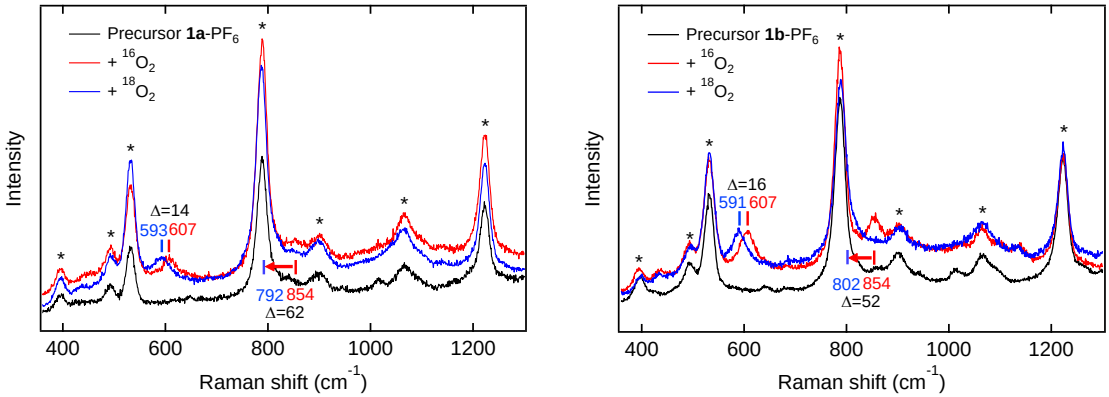

Figure S29: Low-temperature resonance Raman spectra at 193 K. Left: Resonance Raman spectra of **1a**-PF_6 before (black) and after the reaction with $^{16}O_2$ (red) and $^{18}O_2$ (blue). **Right:** Resonance Raman spectra of **1b**-PF_6 before (black) and after the reaction with $^{16}O_2$ (red) and $^{18}O_2$ (blue). The asterisks mark solvent signals of acetone. The laser excitation wavelength was 393 nm.

Reaction of **1b**-PF_6 with dioxygen at -80 °C (193 K) leads to a resonance Raman spectrum which is very similar to that of **1a**-PF_6 and exhibits two isotope-sensitive peaks at 854 and 607 cm^{-1} (Figure S29, right). In analogy to the latter, the peak at 854 cm^{-1} is attributed to the O-O stretch (ν_6) and the peak at 607 cm^{-1} to the antisymmetric Cu-O stretching vibration (ν_5) (Figure S29, right; red). Upon ^{18}O substitution, the intensity of the O-O stretch at 854 cm^{-1} vanishes, reflecting an isotope effect on the frequency of this mode. The ^{18}O-shifted peak appears to be – at least partially – masked by the intense solvent peak at around 800 cm^{-1}. These findings are compatible with theoretical values for $\nu_{O\text{-}O} \equiv \nu_6$ = 849 cm^{-1} and $\Delta(^{16}O_2\text{-}^{18}O_2)$ = 49 cm^{-1}; cf. Table S8. Moreover, using $^{18}O_2$ (Figure S29, right; blue) a frequency shift of the 607 cm^{-1} peak to 591 cm^{-1} (Δ = 16 cm^{-1}) is observed. For **1b**-PF_6 DFT predicts the corresponding Cu-O stretch (ν_5) at 534 cm^{-1} (Δ = 27 cm^{-1}; cf. Table S8), supporting the above assignment of the experimentally observed, isotope-sensitive vibration at 607 cm^{-1} to the antisymmetric Cu-O stretch.

6.6.2. Measurements at 238 K: Characterization of the Cu_2O species

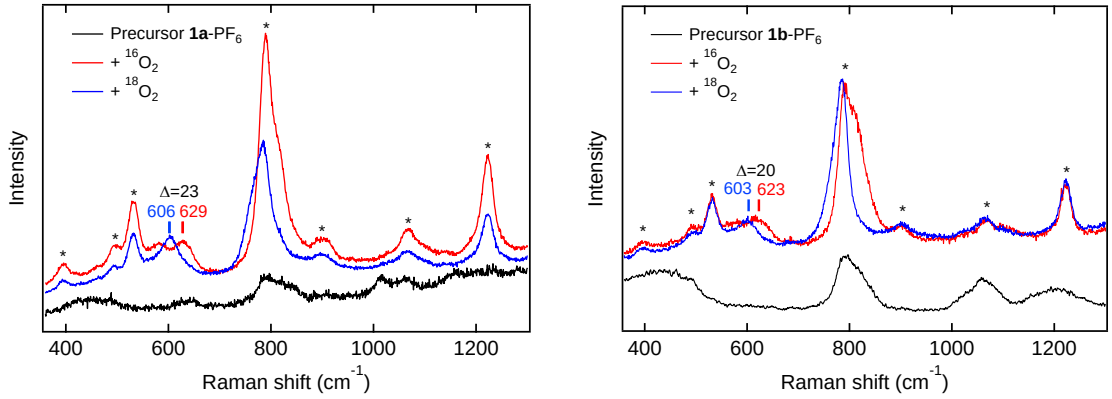

Figure S30: Resonance Raman spectroscopy at 238 K. Left: Resonance Raman spectra of **1a**-PF_6 before (black) and upon reaction with $^{16}O_2$ (red) and $^{18}O_2$ (blue). **Right:** Resonance-enhanced vibrational spectra of **1b**-PF_6 before (black) and after the reaction with $^{16}O_2$ (red) and $^{18}O_2$ (blue). The asterisks mark solvent signals of acetone. The laser excitation wavelength was 393 nm.

Upon reaction of **1a**-PF_6 with dioxygen at -35 °C (238 K), a characteristic isotope-sensitive peak emerges at 629 cm^{-1} (Δ = 23 cm^{-1}) in the resonance Raman spectrum (Figure S30, left). DFT calculations performed for the **Cu_2O** complex of **1a**-PF_6 predict two Cu-O vibrations of A_1 and B_2 symmetry along with a lower-frequency, out-of-plane vibration (ν_1) (cf. Table S8). Based on the frequency, the observed mode is assigned as the B_2 mode predicted at 563 cm^{-1} (ν_3; Δ = 35 cm^{-1}).

Similar observations are made for **1b**-PF_6 upon reaction with dioxygen at -35 °C (238 K). In particular, a characteristic isotope-sensitive peak at 623 cm^{-1} (Δ = 20 cm^{-1}) is observed (Figure S30, right). DFT calculations performed for the **Cu_2O** complex suggest assignment of this feature to the antisymmetric Cu-O stretching vibration (ν_3) which is predicted at 587 cm^{-1} with a ^{18}O shift of Δ = 29 cm^{-1} (cf. Table S8).

6.6.3. Further investigations of the Cu_4O_2 and Cu_2O species: Temperature-induced formation of the Cu_2O complexes

As already stated above, a broad intense feature emerges around 800 cm^{-1} in the resonance Raman spectra of **1a-PF_6** and **1b-PF_6** upon increasing the temperature from -80 °C (183 K) to -35 °C (238 K). As the broad 800 cm^{-1} feature obscures the region of the O-O stretch of the μ_4-peroxo species, evolution of this peak upon heating the sample is difficult to monitor. Importantly, however, a similar feature is also observed for the non-oxygenated complex at the elevated temperature (see above). We therefore assume that it is due to decomposition of the mono-μ-oxo complex, generating free precursor which in turn is subject to thermal/photochemical damage induced by the laser irradiation.

Due to this problem, warming-up of the solution was repeated for **1b**-PF_6, but performed in two steps (cf. Figure S31, top, left). Upon increasing the temperature from -80 °C (Figure S31, top, left; 193 K, blue) to -50 °C (Figure S31, top, left; 223 K, green) the peroxo-associated features (including the O-O stretch) clearly vanish, and further warming to -35 °C leads to the spectrum of the mono-μ-oxo species (Figure S31, top, left; 238 K, red). This confirms that, in agreement with the reaction sequence shown in Scheme S2, thermally induced O-O bond cleavage of the tetranuclear complex does occur in our systems, leading to two **Cu_2O** species. This process

may, however, not proceed in a single step, but involves a more complex reaction sequence. The same experiment was performed for **1b**-OTf which is shown in Figure S31, top, right.

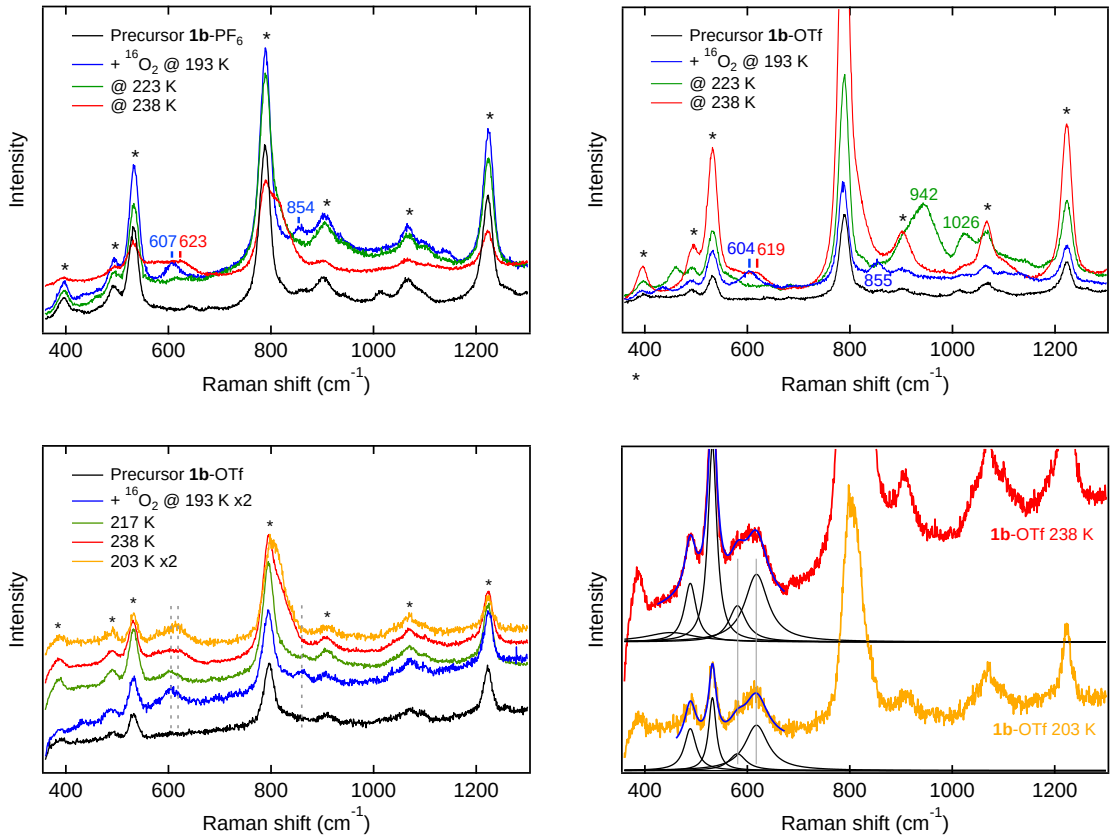

Figure S31: Top, left: Gaining deeper insights into the reaction with O_2: Resonance Raman spectra of **1b**-PF_6 before (black) and after the reaction with dioxygen at three different temperatures (blue: 193 K; green: 223 K; red: 238 K). **Top, right: Investigating the temperature-dependent interconversion – stepwise warming-up:** Resonance Raman spectra of **1b**-OTf before (black) and after the reaction with dioxygen at three different temperatures (blue: 193 K; green: 223 K; red: 238 K). **Blue, 193 K:** The 855 cm^{-1} peak can be attributed to the O-O vibration in the assumed μ_4-peroxo species. The feature at 604 cm^{-1} corresponds to the Cu-O vibration. **Green, 223 K:** Vanishing of the peroxo-attributed O-O feature. Upon ^{18}O substitution the peaks around 430 cm^{-1} (193 K) and 460, 941 and 1026 cm^{-1} (223 K) do not shift. Note, that the broad and intense features at 941 and 1026 cm^{-1} are not reproducible. **Red, 238 K:** The 619 cm^{-1} feature corresponds to the antisymmetric Cu-O vibration of the mono-μ-oxo motif. **Bottom, left: Investigating the temperature-dependent interconversion – re-cooling:** Once the **Cu_2O** complex of **1b**-OTf is formed (red), the interconversion is irreversible and the spectrum of the mono-μ-oxo species is retained after re-cooling (orange). **Bottom, right:** Fit components of the red and orange spectra shown in the figure on the bottom, left, clearly demonstrate that the **Cu_2O** complex is retained after re-cooling. The asterisks mark solvent signals of acetone. The laser excitation wavelength was 393 nm.

Interestingly, if the solution containing the **Cu_2O** species of **1b**-OTf (Figure S31, bottom, left) is cooled again from -35 °C down to -70 °C, the features of the peroxo-core (**Cu_4O_2**) do not re-appear, but the mono-μ-oxo peak at 619 cm^{-1} is retained upon cooling. The fit components for the two relevant spectra are shown in Figure S31 (bottom, right) and clearly demonstrate that the **Cu_2O** species is retained. These observations correspond to those obtained from UV/Vis spectroscopy (see above) and indicate that the considered transformation process is irreversible. Moreover, it appears to be thermally activated.

6.6.4. Reaction with O_2 (additional spectra)

Some additional spectra which are obtained upon reaction of the precursor complexes **1a**-OTf and **1b**-OTf with dioxygen are shown below (see also Table S8).

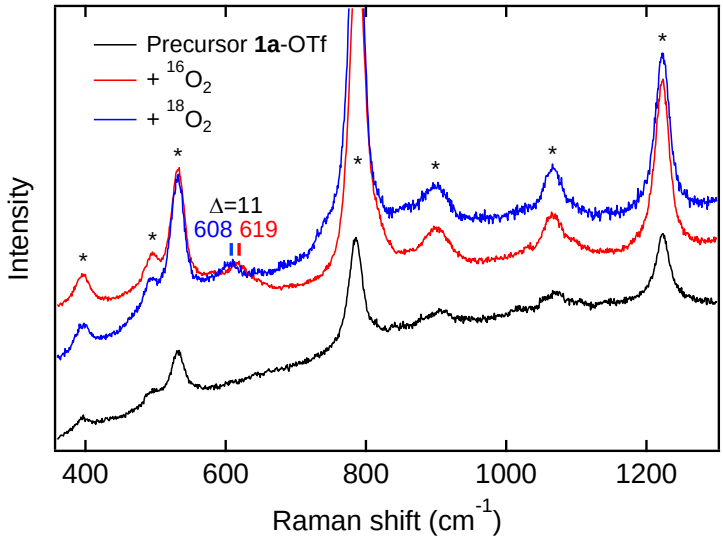

Figure S32: Resonance Raman spectra of 1a-OTf at 238 K. Resonance Raman spectra of **1a**-OTf before (black) and after the reaction with $^{16}O_2$ (red) and $^{18}O_2$ (blue). The asterisks mark solvent signals of acetone. The laser excitation wavelength was 393 nm.

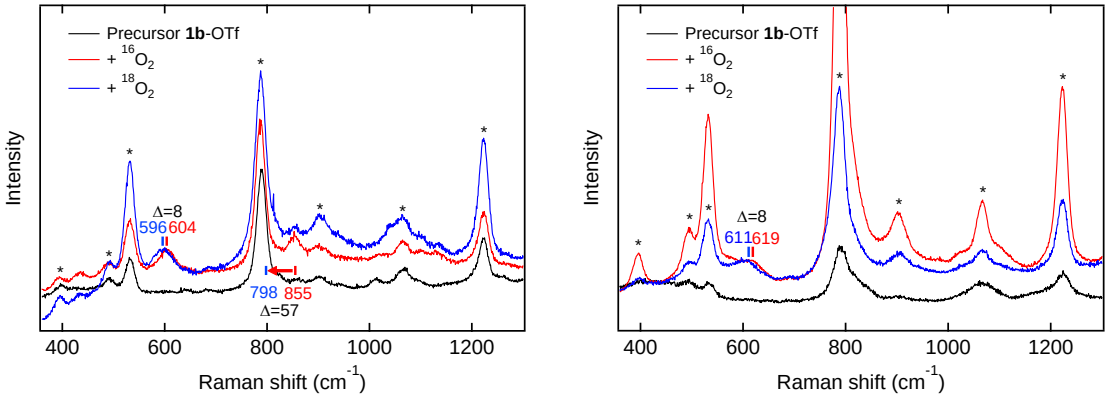

Figure S33: Resonance Raman spectra of 1b-OTf. Left: Resonance Raman spectra of **1b**-OTf before (black) and after the reaction with $^{16}O_2$ (red) and $^{18}O_2$ (blue) at 193 K. **Right:** Resonance-enhanced Raman spectra of **1b**-OTf at 238 K before (black) and after the reaction with $^{16}O_2$ (red) and $^{18}O_2$ (blue). The asterisks mark solvent signals of acetone. The laser excitation wavelength was 393 nm.

6.7. Spectroscopic exclusion of alternative copper dioxygen species at 193 K

The observation that the **Cu_2O** species of **2a** and **2b** can be formed not only by using OAT reagents (PhIO and N_2O) but also by reaction with O_2, suggests that the corresponding Cu(I) precursors are able to bind dioxygen and subsequently cleave the O-O bond of the resulting peroxo complex (cf. Scheme 2 in the main paper). Correspondingly, the UV/Vis spectrum observed upon oxygenation at 183 K does not originate from a **Cu_2O** complex, but rather from the initially formed dioxygen adduct.

In order to obtain more information about this intermediate and its O-O cleavage leading to the **Cu_2O** species, resonance Raman experiments were performed at 193 K. Based on the corresponding DFT calculation (cf. Section S6.1 and S6.2, see also Section S9), the observed isotope-sensitive peaks at 854 cm^{-1} (Δ = 62 cm^{-1}) and the Cu-O stretch at 607 cm^{-1} (Δ = 14 cm^{-1}) for **1a**-PF_6 (corresponding values for **1b-PF6**: $\nu_{O\text{-}O}$ = 854 cm^{-1} (Δ = 52 cm^{-1}) and $\nu_{Cu\text{-}O}$ = 607 cm^{-1} (Δ = 16 cm^{-1}) and for **1b**-OTf : $\nu_{O\text{-}O}$ = 855 cm^{-1} (Δ = 57 cm^{-1}) and $\nu_{Cu\text{-}O}$ = 604 cm^{-1} (Δ = 8 cm^{-1}) can be attributed to a tetranuclear mixed-valent μ_4-peroxo $[Cu(I)/Cu(II)]_2$ complex with a **Cu_4O_2** core.

Importantly, the observed Raman spectra are **NOT** compatible with other adducts of **1a** or **1b** and dioxygen, for the following reasons:

(i) A ***μ*-1,1-peroxo species** where the peroxo ligand bridges the two copper centers could be a possibility. However, the corresponding DFT calculation (PBE-D3(BJ)/def2-SVP) of this species leads to an O-O stretching vibration at 1129 cm^{-1} (Δ = 60 cm^{-1}) for the the **bdpdz** system and 1113 cm^{-1} (Δ = 53 cm^{-1}) for the complex with the **bdptz** ligand, indicating the presence of μ-1,1-superoxo species. However, this would clearly be in contrast with the observed O-O stretching frequencies around 855 cm^{-1} (see above). The optimized structure of the μ-1,1-peroxo dicopper(II) species of the ligands **bdpdz** (left) and **bdptz** (right) are shown in the following figure (see Figure S34).

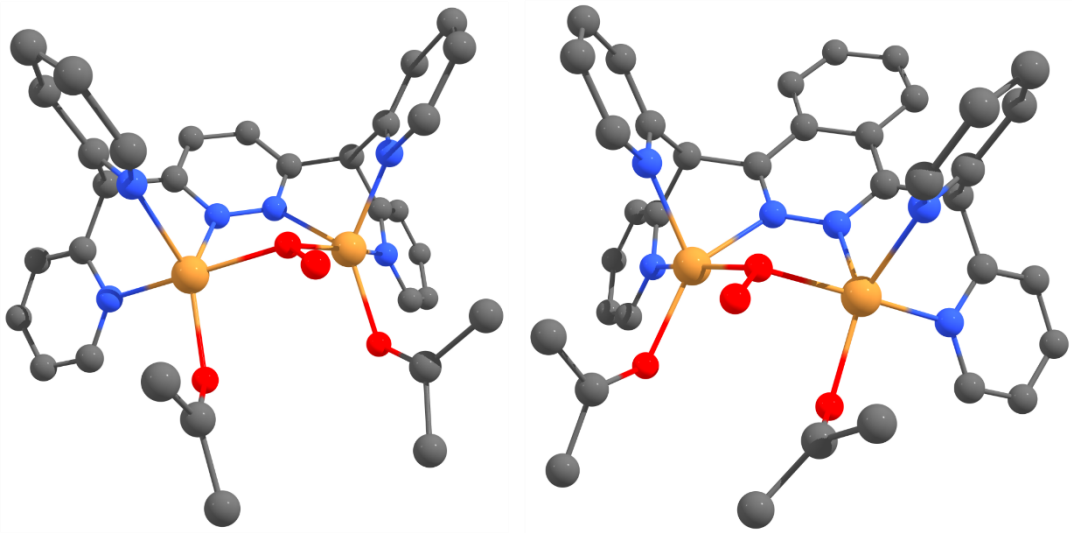

Figure S34: Geometry optimization of the peroxo complex of the ligand **bdpdz** (left) and **bdptz** (right). In analogy to the corresponding **Cu_2O** species, additional acetone molecules complete the coordination sphere. All hydrogen atoms bound to carbon atoms have been omitted for clarity. DFT: RI-PBE-D3(BJ)/def2-SVP.

(ii) For **terminally (η^1-) bound superoxo complexes**, the literature gives values of $\nu_{Cu\text{-}O}$ = 472 (20) cm^{-1} and $\nu_{O\text{-}O}$ = 1121 (63) cm^{-1}),[43, 44] also ruling out such species to account for the low-temperature Raman data. The same applies to **terminally (η^1-) bound peroxo** species; e.g., the complex of the **XYL-O** ligand from Karlin and Zubieta, which shows an O-O stretching frequency at 803 cm^{-1} (Δ = 53 cm^{-1}) and a Cu-O vibration at 488 cm^{-1} (Δ = 24 cm^{-1}).[45, 46] Notably, both the O-O stretch and the Cu-O vibration are at lower frequency than observed in our case. Moreover,

the UV/Vis spectrum of this species (two absorption bands at λ_{max} = 500-510 nm (ε = 4900-6700 M^{-1} cm^{-1}) and λ_{max} = 610-642 nm (ε = 800-2700 M^{-1} cm^{-1}, *shoulder*)) is characteristically different from those of our peroxo complexes.[46, 45] Finally, a ***μ*-1,1-hydroperoxo complex** may form through protonation of an initially formed peroxo complex. However, these species have frequencies of ν_{Cu-O} = 322/506-572 (10/20) cm^{-1} and ν_{O-O} = 860-892 (50) cm^{-1}.[43, 44, 45] While their O-O stretches are higher than observed in our case, the Cu-O stretches are below 600 cm^{-1}, in contrast to our case.

(iii) **End-on bridging peroxo (*μ*-1,2-peroxo) species** are well-known in the literature. The resonance Raman spectrum shows a peak around 799-848 cm^{-1} (which typically shifts upon isotope exchange by Δ = 44-54 cm^{-1}) that corresponds to the O-O stretch. In addition, the Cu-O peak can be found at about 437-571 cm^{-1} (Δ = 19-26 cm^{-1}).[43, 44, 45, 47] Again, no Cu-O stretches above 600 cm^{-1} have been observed for these species. Moreover, their UV/Vis spectrum with two absorption features around 500-550 nm (ε = 2000-11300 M^{-1} cm^{-1}) and 600-630 nm (ε = 1250-5800 M^{-1} cm^{-1}) and a band around 415-435 nm (ε = 1100-1700 M^{-1} cm^{-1}) is characteristically different from that of our species. The *μ*-1,2-peroxo species thus can be excluded as well.

In conclusion, the observed Raman spectra at 193 K, which exhibits two isotope-sensitive peaks at 854-855 and 604-607 cm^{-1} (Δ = 52-62 and 8-16 cm^{-1}, respectively), are not compatible with one of the species considered above, but can only be interpreted on the basis of the **Cu_4O_2** complex. This could be confirmed by use of UV/Vis spectroscopy complemented by XAS and UHR-ESI mass spectrometry. Assignment of the primary dioxygen adduct to a tetranuclear **Cu_4O_2** complex is also supported by data of Davies and El-Sayed.[34] Scheme S5 describes a possible pathway for the formation of the tetranuclear species from the dinuclear copper(I) precursor and dioxygen in agreement with the findings. Thermally induced O-O-bond cleavage occurring at T > 193 K is irreversible and leads to the final **Cu_2O** species.

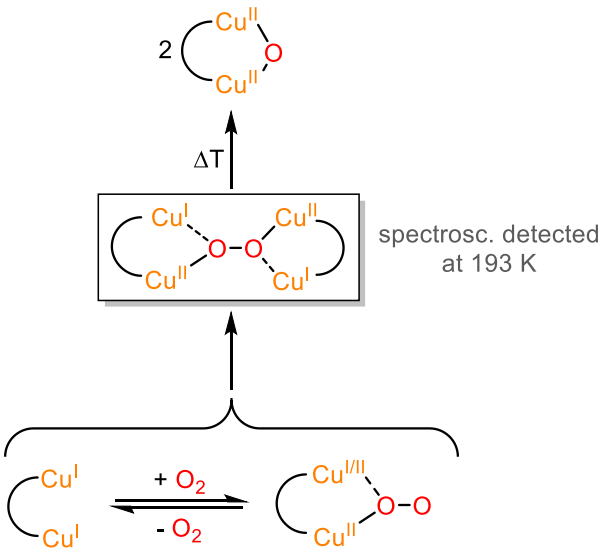

Scheme S5: Formation of the tetranuclear species from the dinuclear copper(I) precursor and dioxygen. Thermally induced O-O-bond cleavage leads to the final **Cu_2O** species.

7. Cryo-UHR-ESI Mass Spectrometry

Reaction of **1a** or **1b** with dioxygen at -35 °C provided the following mass spectra which are in excellent accordance with the calculated spectrum and simulated isotopic distribution pattern of the estimated doubly positively charged species containing only one O atom. When the **Cu_2O** complex of **1a** or **1b** is prepared with $^{18}O_2$ the **Cu_2O**-attributed peak shifts by one mass unit as expected (see below). Notably, while no mono-μ-oxo species is found at -90 °C, the oxygenation of **1a** or **1b** at -35 °C yielded also tetranuclear species containing only one O atom (**Cu_4O**; which can be attributed to a decomposition product caused by the higher temperature) as well as **Cu_4O_2** species (not clearly identified because the peaks overlap). In addition, **Cu_2O_2** species which could be a possible decomposition product of the tetranuclear μ_4-peroxo species upon increasing the temperature from 193 K (-80 °C) to 238 K (-40 °C) can also be observed, but the peaks overlap with the corresponding **Cu_2N_2** analogue (cf. Section 6.4). Moreover, beside the **Cu_2O** complex being the predominant species at that temperature, mono-μ-hydroxo species can also be assigned, probably because of humidity and preparation procedure (condensing conditions because of low temperature compared to room temperature). Notably, no bis-μ-hydroxo species is observed, which would be an indication for a high basicity of the oxo ligand.[48]

Upon reaction of an acetone solution of **1a**-OTf **or 1b**-OTf with O_2 at -90 °C (183 K) the mass spectra shown below were obtained demonstrating the relevant peaks with the isotopic pattern and corresponding *m/z* values resembling the simulated spectrum of the tricationic species [**3a-**OTf]$^{3+}$ or [**3b-**OTf]$^{3+}$. Hence, the oxidation states are mixed-valent Cu(II) and Cu(I) as we proposed and the species contains two O-atoms deriving from O_2 (O_2^{2-}, two Cu(II), two Cu(I), two **bdpdz** or **bdptz** and one triflate). The complex cannot be a tetranuclear all Cu(II) species with two **bdpdz** or **bdptz**, O_2^{2-} and a bound OTf^- anion, since such a complex would be detected as fourfold positive species. Consequently, by usage of $^{18}O_2$ the characteristic peak shifted by 4/3 mass units. Noteworthy, the triflate complexes of **1a** and **1b** seem to stabilize the **Cu_2O_4** core better in contrast to their PF_6-counterparts under the conditions of cryospray-ionization mass spectrometry (CSI-MS) measurements. Therefore, we could not observe the tetranuclear species at -90 °C with the corresponding PF_6-complexes of **1a** and **1b**. This might be attributed to the ability of the PF_6^- anion to be more weakly coordinating in contrast to the OTf^- anion which is able to coordinate via the O-atom.[49]

7.1. Obtained mass spectra upon reaction with $^{18}O_2$

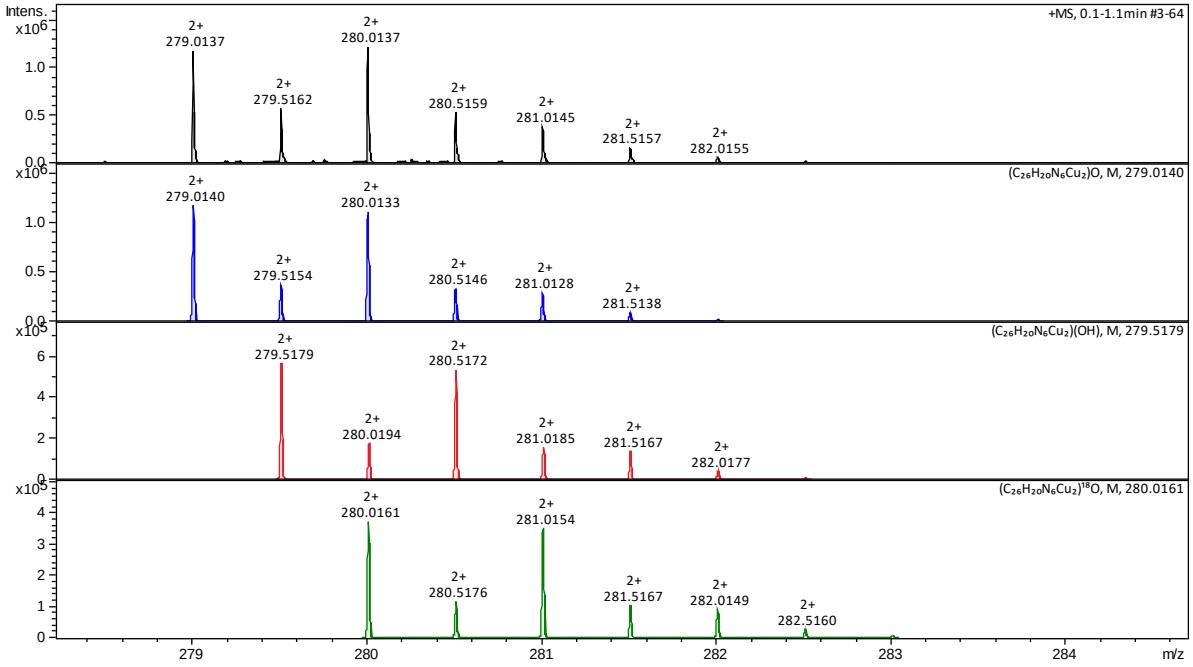

Figure S35: Cryo-UHR-ESI mass spectrum of **1a**-OTf after reaction with $^{18}O_2$ at -40 °C. The isotopic pattern and corresponding *m/z* value resemble the simulated spectrum for the **$Cu_2{}^{18}O$** species (green). Due to humidity the detected pattern is a superposition of the **$Cu_2{}^{18}O$** (green) and **$Cu_2{}^{16}O$** (blue) species together with the mono-μ-hydroxo complex (red). The corresponding **$Cu_2{}^{18}O$** species with one triflate can be detected as well. The same result was obtained for **1a**-PF_6 (not shown).

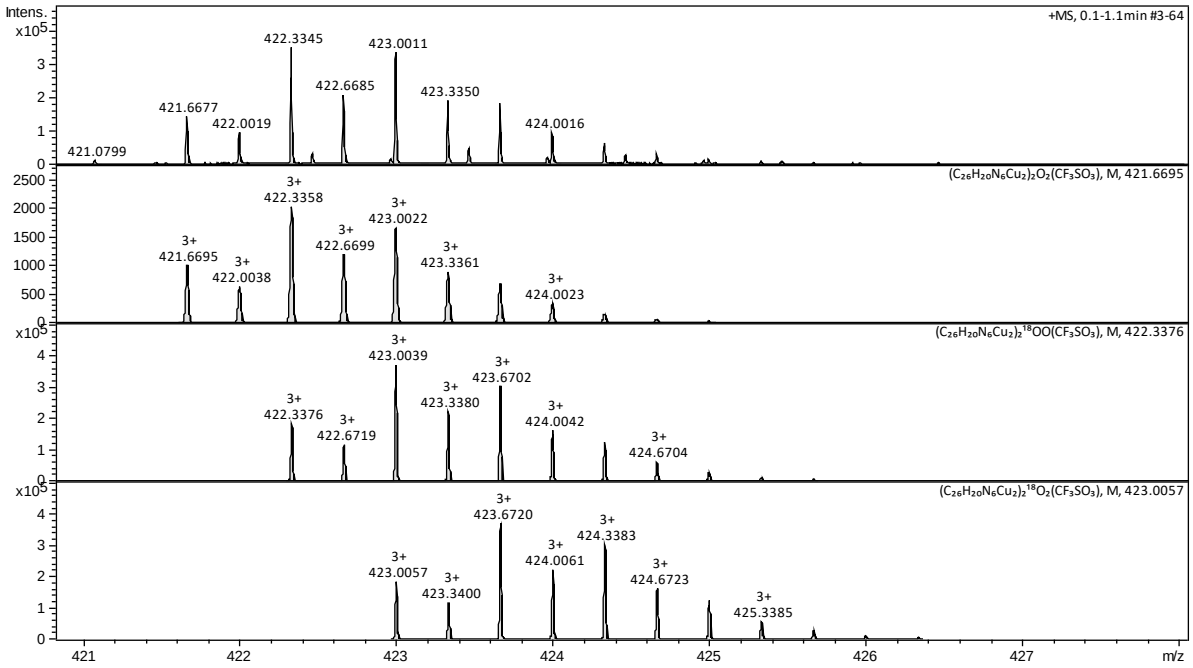

Figure S36: Cryo-UHR-ESI mass spectrum of **1a**-OTf after reaction with $^{18}O_2$ at -90 °C. The isotopic pattern and corresponding *m/z* value resemble the simulated spectrum for the tetranuclear **$Cu_4{}^{18}O_2$** species with an additional triflate ion. Further, the **Cu_4O_2** complex with $^{16}O^{18}O$ and $^{16}O^{16}O$ can be detected as well. The same result was obtained for **1a**-PF_6 (not shown).

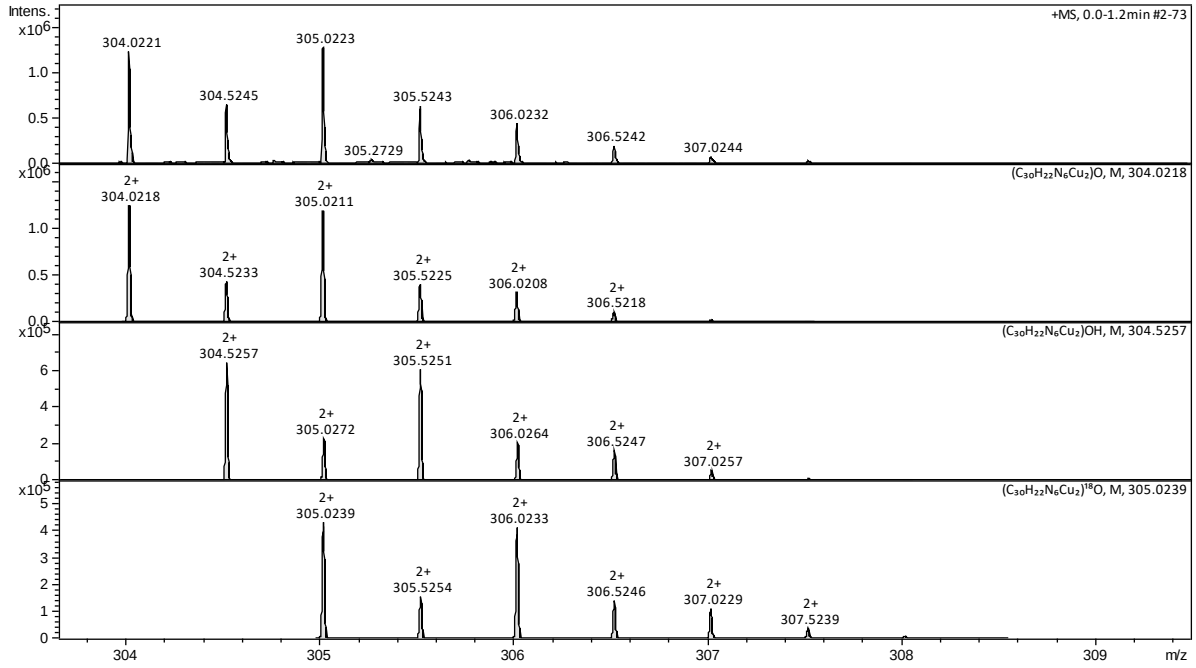

Figure S37: Cryo-UHR-ESI mass spectrum of **1b**-OTf after reaction with $^{18}O_2$ at -40 °C. The isotopic pattern and corresponding *m/z* value resemble the simulated spectrum for the **$Cu_2{}^{18}O$** species. Due to humidity the detected pattern is a superposition of the **$Cu_2{}^{18}O$** and **$Cu_2{}^{16}O$** species together with the mono-μ-hydroxo complex. The corresponding **$Cu_2{}^{18}O$** species with one triflate can be detected as well. The same result was obtained for **1b**-PF_6 (not shown).

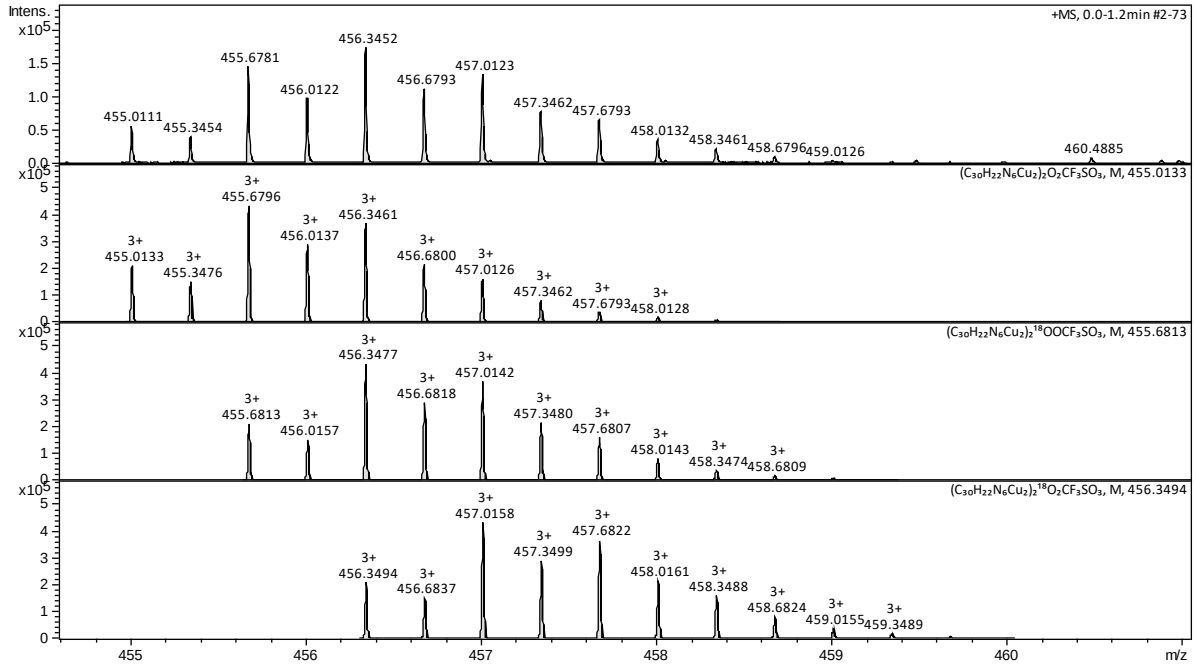

Figure S38: Cryo-UHR-ESI mass spectrum of **1b**-OTf after reaction with $^{18}O_2$ at -90 °C. The isotopic pattern and corresponding *m/z* value resemble the simulated spectrum for the tetranuclear **$Cu_4{}^{18}O_2$** species with an additional triflate ion. Further, the **Cu_4O_2** complex with $^{16}O^{18}O$ and $^{16}O^{16}O$ can be detected as well. The same result was obtained for **1b**-PF_6 (not shown).

In addition, the same results were obtained for the corresponding hexafluorophosphate analogues **1a**-PF_6 and **1b**-PF_6 as well.

In conclusion, the observed isotopic patterns and *m/z* values for both species (**Cu_2O** and **Cu_4O_2**) correspond excellent to the predicted spectra, demonstrating mixed-valence of the tetranuclear peroxo species and there is clear evidence for both the mono-μ-oxo complex and the **Cu_4O_2** species, confirming our assignments. Moreover, the Cryo-UHR-ESI data presented in this section strongly support the reaction sequence shown in Fig. 2a of the main paper and in Scheme S2; i.e., at low temperature a tetranuclear mixed-valent μ_4-peroxo-species (**Cu_4O_2**) is formed and at higher temperature the corresponding mono-μ-oxo complex (**Cu_2O**) can be found.

8. X-ray Absorption Spectroscopy

8.1. Additional XANES and EXAFS spectra of 1a-PF_6

Detailed information on the oxidation state and the nearest-neighbor environment of the copper centers in the **Cu_2O** and **Cu_4O_2** complexes of **1a**-PF_6 is provided by EXAFS and XANES. Similar results are obtained as presented for **1b**-PF_6.

Upon oxygenation of the Cu(I) precursor (**1a**-PF_6) to the **Cu_4O_2** complex (**3a**-PF_6) and further conversion to the **Cu_2O** species (**2a**-PF_6) the spectra shown in Figures S39 and S40 are obtained.

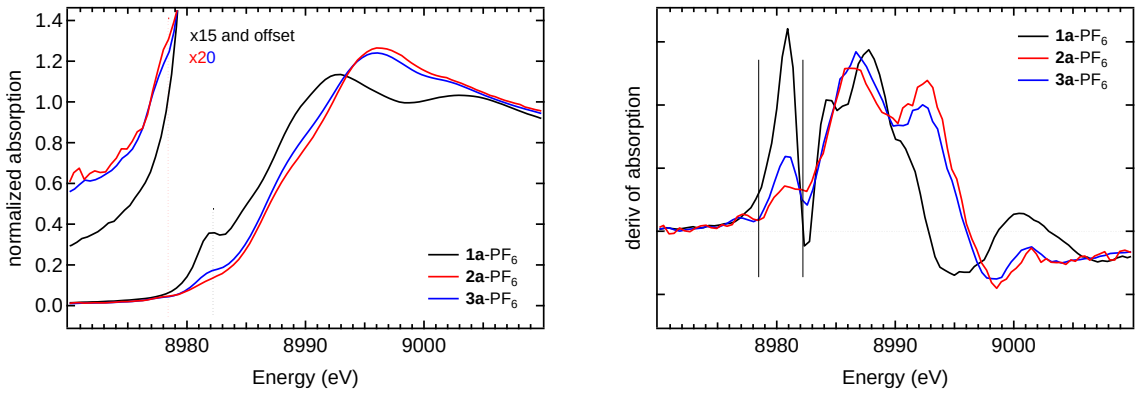

Figure S39: X-ray absorption data for the copper(I) complex and oxygen intermediates of 1a-PF_6 (Part I). Left: Cu K-edge XANES spectra of **1a**-PF_6 before (black line, Cu(I)) and after the reaction with dioxygen at 183 K (blue line, **Cu_4O_2**) and 238 K (red line, **Cu_2O**) with enlarged pre-edge region. **Right:** Derivatives of the spectra given on the left, showing the XANES region in more detail.

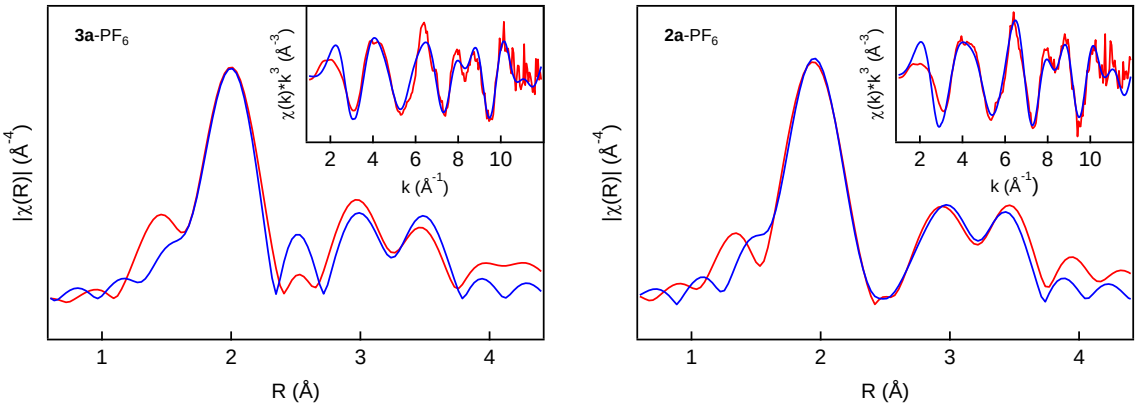

Figure S40: X-ray absorption data for the copper(I) complex and oxygen intermediates of 1a-PF_6 (Part II). Left: Phase-corrected Cu K-edge Fourier transform of EXAFS of **3a**-PF_6 at 183 K (red). Inset: k^3-weighted Cu K-edge EXAFS of **3a**-PF_6 (red). The best fit for both spectra is shown in blue. **Right:** Phase-corrected Cu K-edge Fourier transform of EXAFS of **2a**-PF_6 at 238 K (red). Inset: k^3-weighted Cu K-edge EXAFS of **2a**-PF_6 (red). The best fit (blue) is obtained using the theoretical model with two acetone ligands coordinating with their carbonyl O-atoms (O)s.

8.2. EXAFS analysis of 1a-PF_6 and 1b-PF_6

The best fits are obtained by use of theoretical models with two acetone coligands for the **Cu_2O** and no solvent ligands for the **Cu_4O_2** species. With these assumptions, good agreement between the data and the respective fit spectra is achieved; the most important bond lengths and interatomic distances around the Cu centers derived from Cu K-edge EXAFS for the model systems **1b**-PF_6 and **1a**-PF_6 are summarized in Tables S11 and S12, respectively.

Table S11: EXAFS fit parameters of the oxygenated complexes **2b**-PF_6 and **3b**-PF_6.

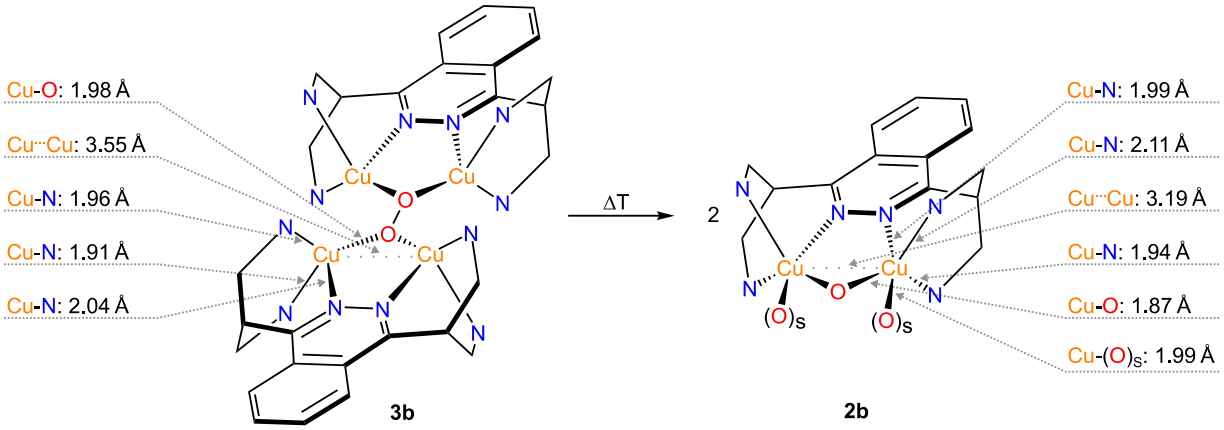

Sample	R-factor	N_{idp}	N_{var}	R-range fit	k-range fit	ΔE_0 (eV)	
2b-PF_6	0.017	12.4	9	1-3.2	3-12	1.74	
3b-PF_6	0.012	13.5	11	1-3.4	3-12	-0.34	
Sample	**Path**	**R_{Fit} (Å)**	**R_{DFT} (Å)**	**R_{Fit}-R_{DFT} (Å)**	**+/- R_{Fit} (Å)**	**σ^2 (10^{-3} Å^2)**	**+/- σ^2 (10^{-3} Å^2)**
2b-PF_6	Cu-O	1.87	1.86	0.01	0.09	9	16
	Cu-N_{Py}	1.94	2.06	-0.12	0.02	3	3
	Cu-N_{Phtz}	1.99	2.11	-0.12	0.02	3	3
	Cu-(O)s	1.99	2.11	-0.12	0.02	3	3
	Cu-N_{Py}	2.11	2.24	-0.13	0.02	3	3
	Cu···Cu	3.19	3.19	-0.01	0.03	7	2
3b-PF_6	Cu-O	1.98	1.95	0.03	0.05	4	3
	Cu-N_{Py}	1.91	2.01	-0.10	0.05	7	5
	Cu-N_{Py}	1.96	2.06	-0.10	0.05	7	5
	Cu-N_{Phtz}	2.04	2.15	-0.11	0.05	7	5
	Cu···Cu	3.55	3.39	0.16	0.03	9	3

With N_{py}: *N*-donor of a pyridine ring and N_{Phtz}: *N*-donor of the phthalazine spacer.

Table S12: EXAFS fit parameters of the oxygenated complexes **2a**-PF_6 and **3a**-PF_6.

Sample	R-factor	N_{idp}	N_{var}	R-range fit	k-range fit	ΔE_0 (eV)	
2a-PF_6	0.014	12.4	10	1-3.2	3-12	0.07	
3a-PF_6	0.036	13.5	9	1-3.4	3-12	2.27	
Sample	**Path**	**R_{Fit} (Å)**	**R_{DFT} (Å)**	**R_{Fit}-R_{DFT} (Å)**	**+/- R_{Fit} (Å)**	**σ^2 (10^{-3} Å^2)**	**+/- σ^2 (10^{-3} Å^2)**
2a-PF_6	Cu-O	1.91	1.88	0.03	0.1	3	4
	Cu-N_{Py}	1.95	2.09	0.14	0.05	8	10
	Cu-(O)s	1.96	2.09	0.13	0.05	8	10
	Cu-N_{Pydz}	2.00	2.12	0.12	0.05	8	10
	Cu-N_{Py}	2.00	2.14	0.14	0.05	8	10
	Cu···Cu	3.23	3.12	0.11	0.02	4	2
3a-PF_6	Cu-O	1.91	1.96	0.05	0.06	3	10
	Cu-N_{Py}	1.95	2.02	0.07	0.06	1*	-
	Cu-N_{Py}	1.98	2.05	0.07	0.06	1*	-
	Cu-N_{Pydz}	2.07	2.14	0.07	0.06	1*	-
	Cu···Cu	3.25	3.41	0.16	0.02	4	2

With N_{py}: *N*-donor of a pyridine ring and N_{Pydz}: *N*-donor of the pyridazine spacer.
*: hits lower constraints bound of 0.0015 taken from reference [50].

We see a rather big error in R of 0.09 Å for Cu-O in **2b**-PF_6 and a corresponding considerably big error in σ^2 (cf. Table S13). This could be an indicator that we measured a mixture of **Cu_2O** (**2b**) and **Cu_4O_2** (**3b**). The reason for this could stem from being too cold when oxygenating and or not warming the sample up long enough in the cryostat. For **1a**-PF_6 we see the opposite trend that both fits converge near the calculated values for the **Cu_2O** species (**2a**) indicating being too warm while oxygenation and as the reaction being not reversible generating more **Cu_2O** than **Cu_4O_2** already (cf. Figure S39).

Cu···Cu distances for both **Cu_4O_2** species differ considerably from the calculated values. This could originate from the fact that the theoretical model used, is not considering coordinated acetone in the mixed-valent copper species and thus measuring the complex in a slightly different geometry than what has been calculated by DFT (see Table S14).

The Cu-O-Cu angle of the mono-μ-oxo complexes of **1a** and **1b** derived from the EXAFS data were 115.5° for **1a**-PF_6 (DFT: 113.538°, see Section S9) and 117.1° for **1b**-PF_6 (DFT: 118.205°, see Section S9).

All in all, this leads to the conclusion that while performing good XAS measurements and obtaining adequate data for the **Cu_2O** and **Cu_4O_2** species is possible already with our custom-made cuvette, validating the results from the other methods used, improvements for controlling the exact temperature for oxygenation is a necessary step for improving the setup for this challenging measurement.

Comparison with the literature: The EXAFS spectroscopy carried out for the **Cu_2O** species of the **MePy2** ligand of Karlin *et al*. provided values for the Cu-N bond length at 2.023 Å and 1.906 Å for the Cu-O bond length (which was identified by comparing the atomic distances with those within bis-μ-hydroxo dicopper(II), bis-μ-oxo dicopper(III) and μ-peroxo dicopper(II) units).[35] EXAFS data of the **Cu_2O** complex supported by the **FurNeu** system of Limberg *et al*. provided the following values: 2.91 Å (DFT: 2.844 Å) for the Cu-Cu distance and 1.79 Å (DFT: 1.791 Å) for the Cu-O (Cu-O/N) bond length and 105.17° for the Cu-O-Cu angle.[29] The same group published the crystal structure for their room temperature stable **Cu_2O** complex (Cu-Cu: 2.844 Å, Cu-O: 1.791 Å and Cu-N: 2.407/2.415 Å, 2.022/2.024 Å, 2.163/2.157 Å, Cu-O-Cu: 105.17°).[29] With 2.9 Å (DFT: 3.29 Å) the Cu-Cu distance in the oxygen-activated zeolite **Cu-ZSM-5** lies in the same range and for the Cu-O bond length 1.75/1.76 Å and 139° for the Cu-O-Cu angle were expected by DFT.[26] Therefore, our obtained data are in good agreement with the values for **Cu_2O** complexes found in literature.

9. Additional DFT Calculations

The presented data within the main paper demonstrate that the available spectroscopic data for **Cu_2O** complexes show overall agreement, although some variations, reflecting the influence of different ligand environments, structural parameters or solvents are encountered. To gain deeper insights we performed calculations for the **Cu_2O** and **Cu_4O_2** complexes of **1a** and **1b** (see Figure S41). We decided to do calculations for solvent-free complexes and structures containing additional coligands, e.g. acetonitrile or acetone and compared these with the experimentally obtained data. In addition, for the **Cu_2O** species of **1a** and **1b** we performed TDDFT calculations. Furthermore, the theoretically and experimentally obtained data show reasonable agreement given the known limitations of (TD)DFT for the assigned **Cu_2O** and **Cu_4O_2** complexes of **1a** and **1b**.

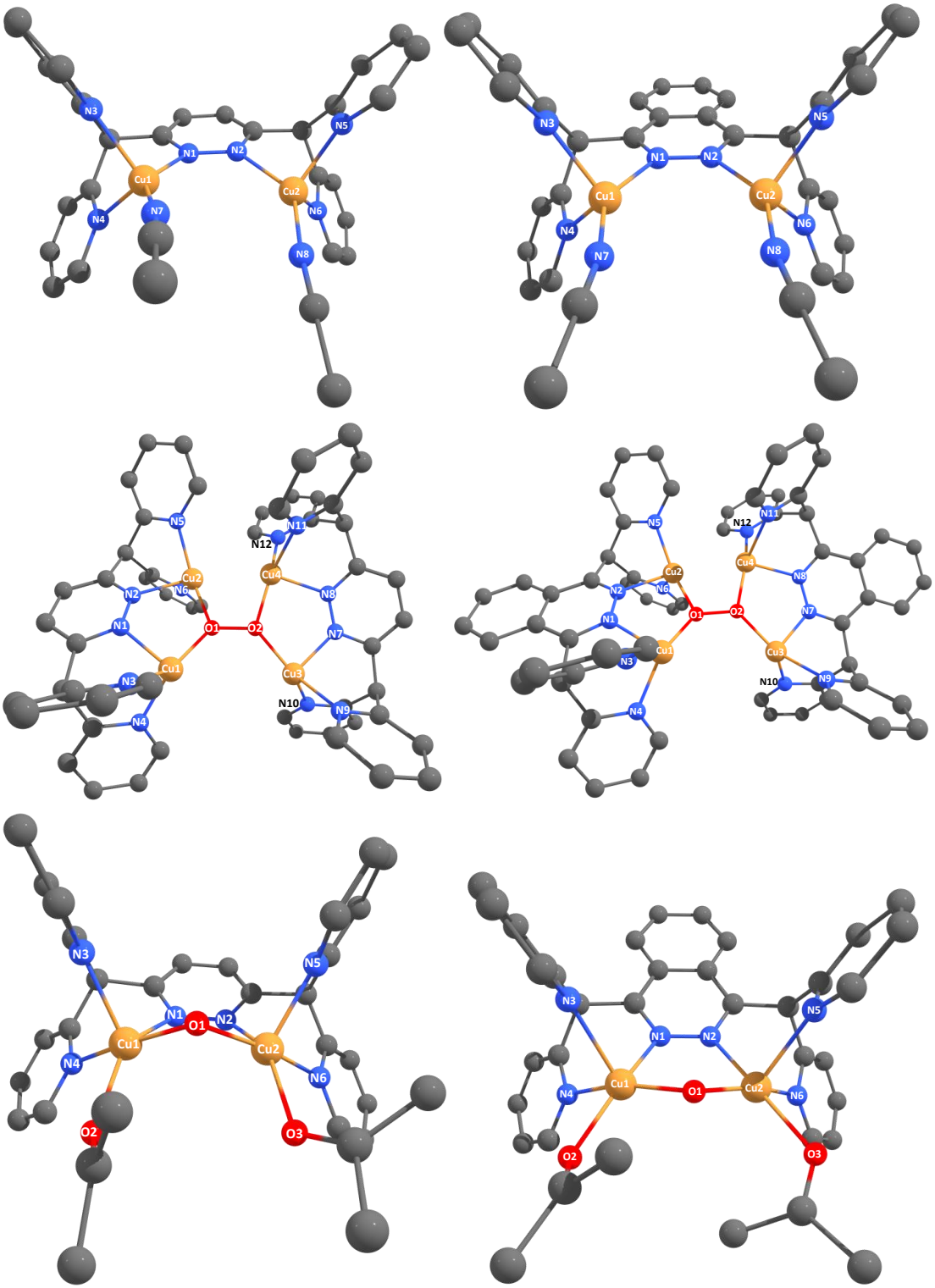

Figure S41: Geometry optimization of the **Cu_2** (top), **Cu_4O_2** (middle) and **Cu_2O** (bottom) complexes of the ligands **bdpdz** (left) and **bdptz** (right). The most promising DFT-structures are shown; e.g. the **Cu_2O** complexes with additional acetone molecules as coligands completing the coordination sphere to distorted square pyramidal. All hydrogen atoms have been omitted for clarity. Selected bond lengths and angles are given in the following tables (see below). Notation for the **Cu_4O_2** complex of **1b** with two additional acetone molecules: the bound acetone is named O3 (bound to Cu1) and O4 is the second, free acetone molecule. DFT: RI-PBE-D3(BJ)/def2-SVP.

9.1. Selected bond length and angles

Table S13: Selected bond lengths (Å), including Cu···Cu distances (Å) and angles (°) for the precursor complexes of **bdpdz** (**1a**) and **bdptz** (**1b**) obtained by DFT. DFT: PBE/def2-SVP-def2/J-RI-D3BJ.

precursor	1a (bdpdz)		1b (bdptz)	
	acetone	CH_3CN	acetone	CH_3CN
Bond lengths / Å				
Cu1···Cu2	3.776	**3.702**	3.614	**3.563**
Cu1-N1	2.033	**2.036**	2.020	**2.036**
Cu1-N3	2.061	**2.084**	2.078	**2.077**
Cu1-N4	2.056	**2.073**	2.060	**2.080**
Cu1-O1	1.993	N.A.	2.011	N.A.
Cu1-N7	N.A.	**1.882**	N.A.	**1.880**
Cu2-N2	2.004	**2.040**	2.030	**2.035**
Cu2-N5	2.062	**2.071**	2.049	**2.080**
Cu2-N6	2.057	**2.081**	2.056	**2.078**
Cu2-O2	1.983	N.A.	1.978	N.A.
Cu2-N8	N.A.	**1.881**	N.A.	**1.880**
Bond angles / °				
N1-Cu1-N3	92.652	**91.322**	92.040	**90.570**
N1-Cu1-N4	92.617	**90.648**	91.126	**90.531**
N3-Cu1-N4	93.319	**91.253**	93.240	**91.738**
N3-Cu1-O1	122.126	N.A.	109.777	N.A.
N1-Cu1-O1	129.725	N.A.	137.814	N.A.
N3-Cu1-N7	N.A.	**112.875**	N.A.	**114.618**
N1-Cu1-N7	N.A.	**136.740**	N.A.	**142.918**
N4-Cu1-N7	N.A.	**122.343**	N.A.	**114.057**
N2-Cu2-N5	94.777	**90.552**	91.290	**90.570**
N2-Cu2-N6	92.980	**91.356**	92.913	**90.593**
N5-Cu2-N6	92.033	**91.309**	93.040	**91.696**
N5-Cu2-O2	121.421	N.A.	139.963	N.A.
N2-Cu2-O2	133.444	N.A.	116.852	N.A.
N5-Cu2-N8	N.A.	**122.938**	N.A.	**114.144**
N2-Cu2-N8	N.A.	**135.665**	N.A.	**142.948**
N6-Cu2-N8	N.A.	**113.606**	N.A.	**114.461**

Table S14: Selected bond lengths (Å), including Cu···Cu distances (Å) and angles (°) for the **bdpdz** (**1a**) and **bdptz** (**1b**) systems after reaction with dioxygen obtained by DFT. DFT: RI-PBE-D3(BJ)/def2-SVP.

1a (bdpdz)	Cu_2O	Cu_4O_2	
	acetone	naked	acetone
Bond lengths / Å			
Cu1···Cu2	3.124	3.409	N.A.
Cu3···Cu4	N.A.	3.408	N.A.
Cu1···Cu3	N.A.	4.013	N.A.
Cu2···Cu4	N.A.	2.662	N.A.
Cu1-N1	2.122	2.083	N.A.
Cu1-N3	2.140	2.050	N.A.
Cu1-N4	2.085	2.044	N.A.
Cu1-O1	1.879	1.945	N.A.
Cu1-O2	2.091	N.A.	N.A.
Cu3-O2	N.A.	1.945	N.A.
Cu3-N7	N.A.	2.080	N.A.
Cu3-N9	N.A.	2.043	N.A.
Cu3-N10	N.A.	2.055	N.A.
O-O	N.A.	1.412	N.A.
Cu2-N2	2.120	2.053	N.A.
Cu2-N5	2.138	2.019	N.A.
Cu2-N6	2.062	2.148	N.A.
Cu2-O1	1.857	1.964	N.A.

1a (bdpdz)	Cu_2O	Cu_4O_2	
	acetone	naked	acetone
Bond lengths / Å			
Cu2-O3	2.194	N.A.	N.A.
Cu4-O2	N.A.	1.964	N.A.
Cu4-N8	N.A.	2.053	N.A.
Cu4-N11	N.A.	2.149	N.A.
Cu4-N12	N.A.	2.018	N.A.
Bond angles / °			
Cu1-O1-Cu2	113.538	121.428	N.A.
Cu3-O2-Cu4	N.A.	121.322	N.A.
Cu1-O-O-Cu4	N.A.	22.256	N.A.
Cu1-O-O-Cu3	N.A.	28.590	N.A.
Cu2-O-O-Cu3	N.A.	22.867	N.A.
Cu2-O-O-Cu4	N.A.	16.532	N.A.
N1-Cu1-N3	86.686	89.877	N.A.
N1-Cu1-N4	84.737	92.503	N.A.
N3-Cu1-N4	87.379	90.909	N.A.
N3-Cu1-O1	96.495	136.667	N.A.
N4-Cu1-O1	171.370	132.422	N.A.
N1-Cu1-O1	87.784	88.040	N.A.
N3-Cu1-O2	128.946	N.A.	N.A.
N1-Cu1-O2	143.615	N.A.	N.A.
N4-Cu1-O2	89.344	N.A.	N.A.
O1-Cu1-O2	94.152	N.A.	N.A.
N2-Cu2-N5	86.471	92.303	N.A.
N2-Cu2-N6	85.424	86.731	N.A.
N5-Cu2-N6	89.138	90.188	N.A.
N5-Cu2-O1	97.997	154.549	N.A.
N2-Cu2-O1	88.718	89.139	N.A.
N6-Cu2-O1	170.480	115.262	N.A.
N5-Cu2-O3	120.773	N.A.	N.A.
N2-Cu2-O3	152.729	N.A.	N.A.
N6-Cu2-O3	93.227	N.A.	N.A.
O1-Cu2-O3	88.543	N.A.	N.A.
N7-Cu3-N9	N.A.	92.617	N.A.
N7-Cu3-N10	N.A.	89.780	N.A.
N9-Cu3-N10	N.A.	90.832	N.A.
N9-Cu3-O2	N.A.	133.227	N.A.
N10-Cu3-O2	N.A.	135.940	N.A.
N7-Cu3-O2	N.A.	88.127	N.A.
N8-Cu4-N11	N.A.	86.716	N.A.
N8-Cu4-N12	N.A.	92.299	N.A.
N11-Cu4-N12	N.A.	90.179	N.A.
N11-Cu4-O2	N.A.	114.882	N.A.
N8-Cu4-O2	N.A.	89.074	N.A.
N12-Cu4-O2	N.A.	154.938	N.A.
1b (bdptz)	Cu_2O	Cu_4O_2	
	acetone	naked	acetone
Bond lengths / Å			
Cu1···Cu2	3.193	3.377	3.106
Cu3···Cu4	N.A.	3.387	3.198
Cu1···Cu3	N.A.	4.008	4.379
Cu2···Cu4	N.A.	2.666	2.634
Cu1-N1	2.114	2.086	2.103
Cu1-N3	2.244	2.041	2.002
Cu1-N4	2.057	2.041	2.130
Cu1-O1	1.860	1.933	1.955
Cu1-O2	2.114	N.A.	N.A.
Cu1-O3	N.A.	N.A.	2.603
Cu3-O2	N.A.	1.934	1.943
Cu3-N7	N.A.	2.082	2.091
Cu3-N9	N.A.	2.031	2.110

1b (bdptz)	Cu_2O	Cu_4O_2	
	acetone	naked	acetone
Bond lengths / Å			
Cu3-N10	N.A.	2.062	1.991
O-O	N.A.	1.414	1.492
Cu2-N2	2.090	2.057	2.094
Cu2-N5	2.202	2.014	2.000
Cu2-N6	2.057	2.140	2.220
Cu2-O1	1.861	1.953	1.918
Cu2-O3	2.100	N.A.	N.A.
Cu4-O2	N.A.	1.953	1.936
Cu4-N8	N.A.	2.060	2.120
Cu4-N11	N.A.	2.150	2.206
Cu4-N12	N.A.	2.011	2.021
Cu1···O4	N.A.	N.A.	5.006
Cu2···O4	N.A.	N.A.	4.802
Cu3···O4	N.A.	N.A.	3.700
Cu2···O4	N.A.	N.A.	5.291
Bond angles / °			
Cu1-O-Cu2	118.205	120.726	106.597
Cu3-O-Cu4	N.A.	121.175	111.058
Cu1-O-O-Cu4	N.A.	22.362	50.227
Cu1-O-O-Cu3	N.A.	33.750	102.285
Cu2-O-O-Cu3	N.A.	26.060	46.123
Cu2-O-O-Cu4	N.A.	14.672	5.935
N1-Cu1-N3	84.792	89.909	89.331
N1-Cu1-N4	86.533	92.748	89.114
N3-Cu1-N4	86.639	91.154	90.533
N3-Cu1-O1	111.003	137.762	175.182
N4-Cu1-O1	161.425	131.071	93.998
N1-Cu1-O1	89.269	89.064	92.317
N1-Cu1-O3	N.A.	N.A.	87.749
O1-Cu1-O3	N.A.	N.A.	87.137
N3-Cu1-O3	N.A.	N.A.	88.427
N4-Cu1-O3	N.A.	N.A.	176.706
N3-Cu1-O2	101.725	N.A.	N.A.
N1-Cu1-O2	171.227	N.A.	N.A.
N4-Cu1-O2	87.975	N.A.	N.A.
O1-Cu1-O2	93.790	N.A.	N.A.
N2-Cu2-N5	86.329	92.168	87.417
N2-Cu2-N6	86.734	86.878	87.417
N5-Cu2-N6	87.113	90.844	88.920
N5-Cu2-O1	107.698	153.425	168.522
N2-Cu2-O1	89.429	90.207	95.870
N6-Cu2-O1	164.439	115.718	102.155
N5-Cu2-O3	95.111	N.A.	N.A.
N2-Cu2-O3	177.035	N.A.	N.A.
N6-Cu2-O3	90.747	N.A.	N.A.
O1-Cu2-O3	92.594	N.A.	N.A.
N7-Cu3-N9	N.A.	92.832	88.961
N7-Cu3-N10	N.A.	89.357	90.470
N9-Cu3-N10	N.A.	91.260	92.300
N9-Cu3-O2	N.A.	137.311	98.349
N10-Cu3-O2	N.A.	131.422	168.918
N7-Cu3-O2	N.A.	88.898	92.773
N8-Cu4-N11	N.A.	86.700	86.648
N8-Cu4-N12	N.A.	92.434	88.146
N11-Cu4-N12	N.A.	90.263	88.536
N11-Cu4-O2	N.A.	112.829	106.302
N8-Cu4-O2	N.A.	89.514	94.526
N12-Cu4-O2	N.A.	156.903	165.036

9.2. Comparison with the crystal structure

Confirmation of the quality of the performed geometry optimizations is also obtained from comparing selected bond length and angles (e.g. Cu-O-Cu) with the obtained crystal structure for the trinuclear mixed-valent complex supported by the **bdptz** ligand (**compound 2**). Here again, the values fit best when the model for the **Cu_2O** species with acetone is compared. On the other hand, the situation in the dicopper(I) precursor complexes are ambiguous regarding the nature of the coordinating solvent. In the solid form two acetonitrile complete the coordination sphere of the dinuclear copper(I) complexes (as synthesized form, proven by use of NMR spectroscopy). In a solution of acetone, the bound acetonitrile seems to be stable and no de-coordination takes place – remaining the coordination sphere in the solid state. Compared to literature, we assign two acetonitrile molecules completing the coordination sphere of the dinuclear copper(I) complexes not only in the as synthesized form but also as the dissolved species in acetone.[20] In addition, the obtained crystal structure reveals the bound acetonitrile completing the coordination sphere in the copper(I) units of the trinuclear complex as well, confirming the assignment.

Table S15: Comparison of the obtained data from the crystal structure of the trinuclear complex based on the ligand **bdptz** (compound 2) and the theoretical data for **1b** (Cu(I) @Precursor) and **2b** (Cu(II) @**Cu_2O** complex). Selected bond lengths (Å) and angles (°) are given for these **bdptz** systems. DFT: RI-PBE-D3(BJ)/def2-SVP.

1b (bdptz)	**Crystal structure**		**DFT**	
	Cu(I)	**Cu(II)**	**Cu(I) @Precursor[a]**	**Cu(II) @Cu_2O[b]**
Bond lengths / Å			**Bond lengths / Å**	
Cu2-N31	1.895(3)	N.A.	1.880(CH_3C**N**)	N.A.
Cu2-N5	2.073(4)	N.A.	2.078	N.A.
Cu2-N2	2.039(3)	N.A.	2.036	N.A.
Cu2-N6	2.121(3)	N.A.	2.080	N.A.
Cu1-N3	N.A.	2.020(3)	N.A.	2.112
Cu1-N3A	N.A.	2.020(3)	N.A.	2.102
Cu1-N4	N.A.	2.007(3)	N.A.	2.057
Cu1-N4A	N.A.	2.007(3)	N.A.	1.861
Cu1-N1	N.A.	2.491(3)	N.A.	2.223
Cu1-N1A	N.A.	2.491(3)	N.A.	N.A.
Bond angles / °			**Bond angles / °**	
N31-Cu2-N6	103.15(15)	N.A.	114.259	N.A.
N2-Cu2-N6	91.49(12)	N.A.	91.717	N.A.
N5-Cu2-N6	89.86(13)	N.A.	90.562	N.A.
N31-Cu2-N2	147.86(14)	N.A.	142.933	N.A.
N31-Cu2-N5	118.08(15)	N.A.	114.381	N.A.
N2-Cu2-N5	89.99(13)	N.A.	90.570	N.A.
N4A-Cu1-N3	N.A.	93.07(12)	N.A.	93.192(**O**,(**O**)s)
N4-Cu1-N3A	N.A.	93.07(12)	N.A.	86.634
N4A-Cu1-N3A	N.A.	86.93(13)	N.A.	89.361(**O**s)
N4-Cu1-N3	N.A.	86.93(12)	N.A.	89.349(O)
N1A-Cu1-N3	N.A.	94.05(11)	N.A.	N.A.
N1A-Cu1-N3A	N.A.	85.95(11)	N.A.	N.A.
N1-Cu1-N4	N.A.	83.36(12)	N.A.	86.876
N1-Cu1-N4A	N.A.	96.64(12)	N.A.	109.351(**O**)
N1-Cu1-N3	N.A.	85.95(11)	N.A.	85.561
N1-Cu1-N3A	N.A.	94.05(11)	N.A.	98.418((**O**)s)
N1A-Cu1-N4	N.A.	96.64(12)	N.A.	N.A.
N1A-Cu1-N4A	N.A.	83.36(12)	N.A.	N.A.

General Remark: N1-Cu1-N1A 180.00(10). N3-Cu1-N3A 180.00(10). N4-Cu1-N4A 180.00(16). The given values for the DFT-obtained bond length and angles are mean values of both copper(I) or copper(II) ions, because of comparing a mononuclear complex unit with the dinuclear complexes. With (O)s being acetone.

[a] The DFT-structure with acetonitrile is used; since the obtained crystal structure shows that one acetonitrile coligand completes the coordination sphere of the copper(I) ions to distorted tetrahedral. [b] The DFT-structure with acetone is used.

9.3. TDDFT: Calculated UV/Vis spectra of the Cu_2O species

In order to obtain further insight into the origin of the electronic transitions observed in our systems, TDDFT was employed (cf. Table S7). TDDFT calculations performed for the putative dicopper μ-oxo species **2a** and **2b** were found to overall reproduce the dominant absorption features, whereby the best agreement with the experimental results was achieved by calculations including one additional acetone per copper(II) center (cf. Scheme S1). The experimentally observed 630 nm band of **2b**-OTf can be fitted by three most intense features around 590 nm. This assignment is reasonable since the position and relative intensity of the observed broad 630 nm absorption band compared with the 370 nm and 421 nm features, fits also with the literature.[48] Furthermore, the two more intense broad shoulders observed at 370 nm and 421 nm can be assigned to calculated peaks in the relevant region as well. We also analyzed the nature of the transitions by use of difference densities. In particular, the broad absorption feature around 421 nm can be assigned as d-d transition of the copper(II) centers bridged by the oxygen ligand. In contrast, the more intense 366 nm band originates from a ligand-to-metal charge transfer (LMCT) with participation of the phthalazine spacer and pyridine moieties since electron density is forwarded to them (cf. Table S7). Moreover, the band at around 630 nm can predominantly be attributed as LMCT feature, whereby the electron density is unequally distributed between the bridging oxygen atom (representing the electron donor atom) and the phthalazine spacer (denoted as final electron acceptor moiety). The theoretically and experimentally obtained data show reasonable agreement given the known limitations of (TD)DFT supporting the **Cu_2O** assignment of **1a** and **1b** and provides in combination with the literature solid evidence.

9.4. BDFE: Theoretical considerations regarding the BDFE of the Cu_2OH species

The bond dissociation free energy (BDFE) of the **bdptz** system is calculated to gain further insight into the reactivity potential of the **Cu_2O** species. To this end, single-point energy calculations were performed for the putative dicopper μ-oxo species **2b** regarding the following reactions (Equation (1)-(3)).

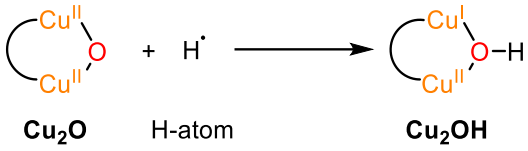

(1)

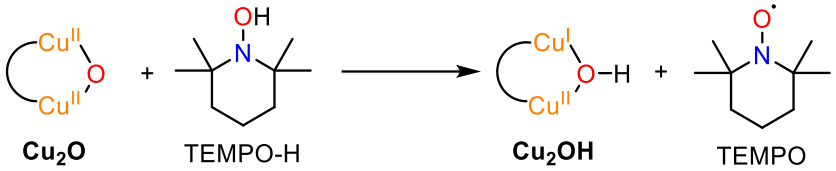

(2)

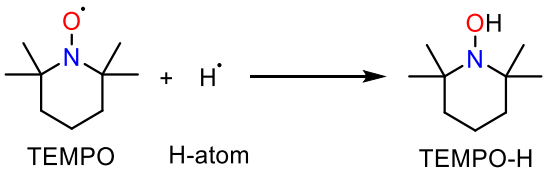

(3)

By adding up equation (2) and (3), (1) results and the BDFE for the **Cu_2O** complex **2b** is obtained. Instead of the transfer of a H-atom (equation (1)), one of the most well studied hydroxylamine/aminoxyl radical pairs, i.e., the TEMPO-H/TEMPO couple (equation (3)) is used, because the $BDFE_{O\text{-}H}$ of TEMPO-H is known (65-71 kcal mol^{-1}, depending on the solvent)[51]. Specifically, a H-atom transfer reaction from 2,2′-6,6′-tetramethylpiperidine-1-ol (TEMPO-H) to **2b**, yielding the 2,2′-6,6′-tetramethyl-piperidine-1-oxyl radical (TEMPO) and the corresponding mixed-valent **Cu_2OH** species **4b** was calculated (equation (2)).

A crude approximation of this O-H bond dissociation free energy can be made, if we assume that the value for the BDFE of TEMPO-H is 66.5 kcal mol^{-1} (in acetonitrile).[51] The resulting BDFE for the Cu(I)-OH-Cu(II) complex **4b** is then calculated to be 110.6 kcal mol^{-1} (see Scheme S6).

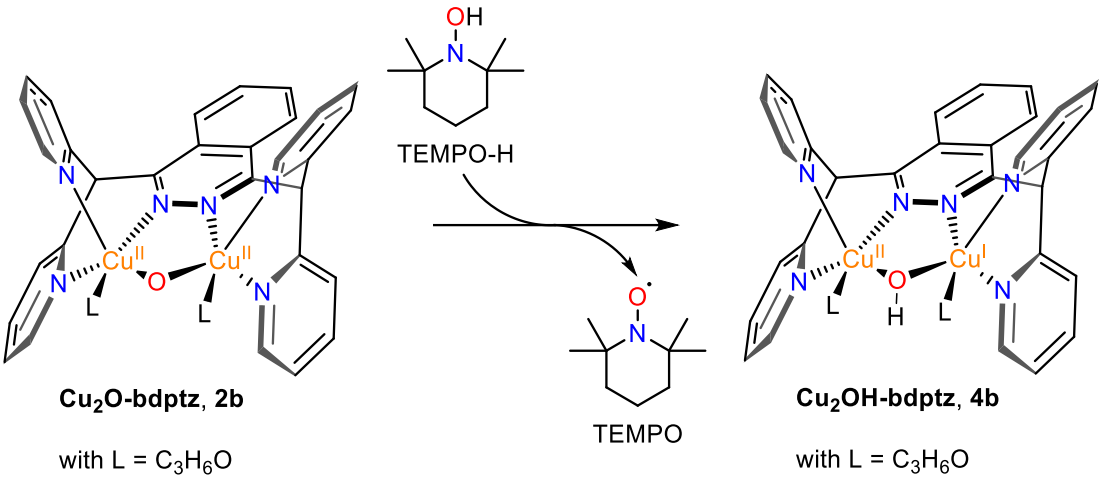

Scheme S6: Reaction of the **Cu$_2$O** complex (**2b**) of the ligand **bdptz** with TEMPO-H to the corresponding mixed-valent mono-μ-hydroxo dicopper(I/II) complex **4b** and the TEMPO radical. The coordinating solvent molecules (acetone) are denoted with L.

This estimated BDFE would suggest that the **Cu$_2$O** complexes should be capable of abstracting a H-atom from even more demanding substrates as the herein tested ones.

Conclusively, the theoretically obtained data support the experimentally observed reactivity against the different hydrocarbons, e.g., DHA and is consistent with the made observations and show reasonable agreement given the known limitations of DFT. Moreover, the BDFE$_{O\text{-}H}$ of the mixed-valent mono-μ-hydroxo dicopper(I/II) complex of the **bdptz** system strongly indicates its ability to convert more demanding substrates like toluene to benzyl alcohol and/or benzaldehyde, cyclohexane to cyclohexanol and/or cyclohexanone or possibly even most challenging methane to methanol.

9.5. Geometry optimization of the mixed-valent Cu_2OH complex

The optimized structure of the mixed-valent mono-μ-hydroxo dicopper(I/II) species (**Cu_2OH**, **4b**) of the ligand **bdptz** is shown in the following figure (see Figure S42).

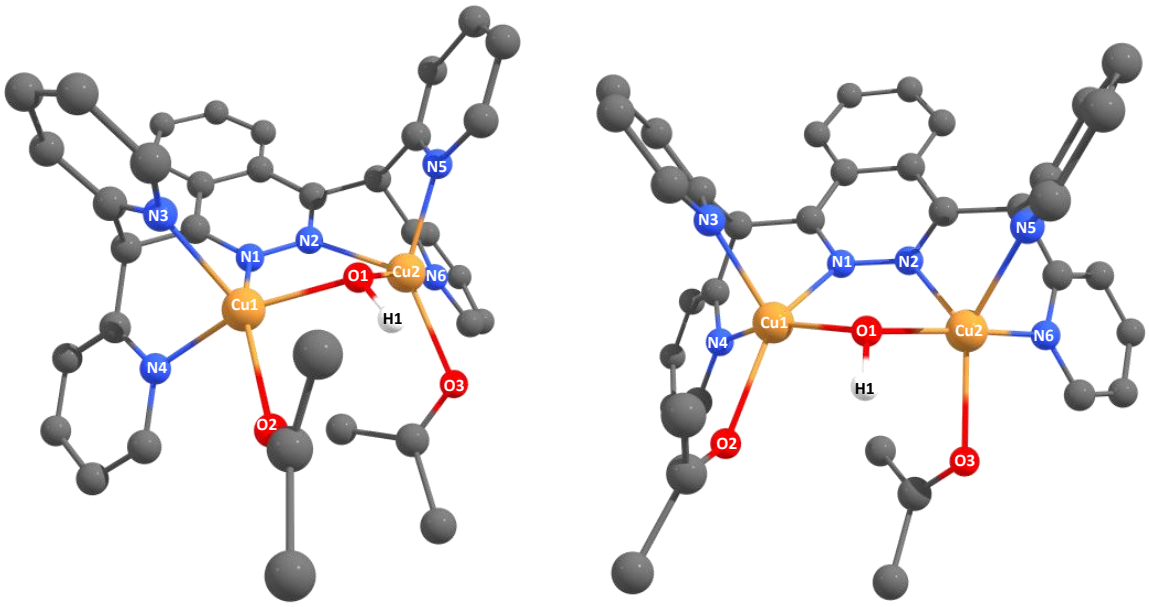

Figure S42: Geometry optimization of the **Cu_2OH** complex of the ligand **bdptz**. In analogy to the corresponding **Cu_2O** species, additional acetone molecules complete the coordination sphere in the mono-μ-hydroxo complex **4b**. All hydrogen atoms bound to carbon atoms have been omitted for clarity. Selected bond lengths and angles are given in the following tables (see below). DFT: RI-PBE-D3(BJ)/def2-SVP.

Selected bond lengths and angles of **4b** are given in Table S16 and compared with the **Cu_2O** species **2b**. The greatest changes in the structure are shown in bold type, i.e., the increased Cu···Cu distance (3.193 Å to 3.382 Å), the reduced Cu1-N1 bond length, causing a more asymmetric 5-ring moiety and the consequently elongated Cu1-O1/Cu2-O1 bond lengths. In addition, several angels have changed, the biggest differences can be observed for the N3-Cu1-O2, N1-Cu1-O2, O1-Cu1-O2, N5-Cu2-O1, N5-Cu2-O3, N2-Cu2-O3 and O1-Cu2-O3 angles.

Table S16: Selected bond lengths (Å), including Cu···Cu distance (Å) and angles (°) for the **bdptz** (**1b**) system for the corresponding **Cu_2O** (**2b**) and **Cu_2OH** (**4b**) complexes obtained by DFT. The most important changes in the bond lengths and angles compared to the **Cu_2O** structure are shown in bold type. DFT: RI-PBE-D3(BJ)/def2-SVP.

bdptz system	**Cu_2O**	**Cu_2OH**
Bond lengths / Å		
Cu1···Cu2	3.193	**3.382**
Cu1-N1	2.114	2.195
Cu1-N3	2.244	**2.126**
Cu1-N4	2.057	2.061
Cu1-O1	1.860	**1.983**
O1-H1	N.A.	**0.976**
Cu1-O2	2.114	**2.280**
Cu2-N2	2.090	2.139
Cu2-N5	2.202	2.112
Cu2-N6	2.057	2.058
Cu2-O1	1.861	**1.986**
Cu2-O3	2.100	2.181
Bond angles / °		
Cu1-O-Cu2	118.205	116.889
N1-Cu1-N3	84.792	87.646
N1-Cu1-N4	86.533	85.537
N3-Cu1-N4	86.639	89.946
N3-Cu1-O1	111.003	111.651
N4-Cu1-O1	161.425	157.071
N1-Cu1-O1	89.269	87.686
Cu1-O1-H1	N.A.	**108.461**
N3-Cu1-O2	101.725	**119.358**
N1-Cu1-O2	171.227	**152.537**
N4-Cu1-O2	87.975	89.335
O1-Cu1-O2	93.790	**86.644**
N2-Cu2-N5	86.329	87.571
N2-Cu2-N6	86.734	87.992
N5-Cu2-N6	87.113	88.420
N5-Cu2-O1	107.698	**97.904**
N2-Cu2-O1	89.429	87.893
N6-Cu2-O1	164.439	172.300
Cu2-O1-H1	N.A.	**106.380**
N5-Cu2-O3	95.111	**139.333**
N2-Cu2-O3	177.035	**133.062**
N6-Cu2-O3	90.747	93.844
O1-Cu2-O3	92.594	**84.240**

10. Reactivity of the Cu_2O Complexes

In order to gain information on the ability of our **Cu_2O** complexes regarding their reactivity towards aliphatic substrates, we established a new procedure and tested the activity of the **Cu_2O** complexes of **1a** and **1b** as catalysts for oxygenation of different hydrocarbon substrates (see Figure S43) .

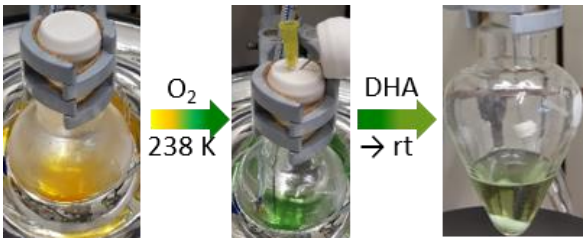

Figure S43: Observed color change during the reactivity studies. Upon reaction with dioxygen, the color changed from yellow to intense green indicating formation of the mono-μ-oxo species. When adding substrate, e.g. DHA the color changed after 2 h at 238 K and additional 2 h at room temperature to pale green. Consequently, when recording the UV/Vis spectra during the reactivity study, we observed the decrease of the characteristic absorption feature around 630 nm.

A three-step protocol was applied in these experiments: (i) the precursor was dissolved in acetone (yellow solution) and reacted with dioxygen at 238 K, leading to the well-characterized green **Cu_2O** species, (ii) the substrate was added at that temperature and reacted for 2 h at 238 K and additional 2 h at room temperature (10 min extra dioxygen were added after 45 min at room temperature), causing a color change to light green; (iii) the reaction mixture was quenched by addition of aqueous Na_2-EDTA solution and the solvent was removed under reduced pressure, followed by quantification with GC-MS (see Section S2.8 for details).

10.1. Overview of the obtained data

The obtained results of the reactivity studies are summarized in the following table (Table S18). The **Cu_2O** complexes of **1a** and **1b** showed reactivity towards different aliphatic substrates, e.g. xanthene (XEN), dihydroanthracene (DHA), fluorene (FEN) and diphenylmethane (DPM). In case of triphenylmethane and fluorene motifs no or barely activity was observed.

In blind experiments, the catalyst was omitted or replaced by $[Cu(CH_3CN)_4]PF_6$ and $[Cu(CH_3CN)_4]OTf$, respectively, leading to no conversion (or poorer results in case of XEN as substrate) .

Table S17: Comparison of the obtained Data for the catalytic activity of the model systems with the different substrates.

Model system	**CuP**[a]		**1a** (bdpdz)		**1b** (bdptz)	
	CuP-PF_6	**CuP**-OTf	**2a**-PF_6	**2a**-OTf	**2b**-PF_6	**2b**-OTf
Substrate	**TON**[b]		**TON**[b]		**TON**[b]	
XEN	0.8	0.6	1.4	2.6	1.4	2.2
DHA[c]	0.0	0.0	3.4	2.2	4.0	4.8
FEN[d]	0.0	0.0	0.6	0.6	0.2	1.0
TPM	N.A.	N.A.	no conv.	no conv.	no conv.	no conv.
DPM[e]	0.0	0.0	2	2	2	2

General remarks: Conditions: 1 equiv. of **1a** or **1b** and 20 equiv. of substrate were applied. O_2 was added via a cannula through the septum with a pressure slightly above 1 atm for a slow gas flow through the sample for 15 min to generate the **Cu_2O** species. The substrate was added and the solution was stirred for 2 h at 238 K without bubbling O_2, but under an O_2 atmosphere. Then the solution was warmed up to room temperature. After 45 min, extra O_2 was added via the cannula for 10 minutes; then, the solution was stirred for another hour at room temperature under O_2 atmosphere. Following abbreviations are used: XEN = xanthene; DHA = dihydroanthracene; FEN = fluorene; TPM = triphenylmethane; DPM = diphenylmethane. The reactivity towards TPM showed no conversion to triphenylmethanol most likely because of its steric demand. Blind reactions were also performed in the same manner without the copper complexes **1a** or **1b**, using $[Cu(CH_3CN)_4]PF_6$ or $[Cu(CH_3CN)_4]OTf$.
[a] $[Cu^{I}(CH_3CN)_4]$ = CuP. [b]TON = Turnover Number; is defined as the equiv. of product made per equiv. of catalyst; the formed **Cu_2O** complex is the catalyst. [c] 10 equiv. of DHA were used; representing 20-fold excess of substrate. The given TON refers to the initially formed disecondary alcohol and does not include the subsequent oxidation. [d] The reactivity towards FEN showed very low conversion to FON; indeed, near the detection limit of the used GC-MS method. [e] 50 equiv. of DPM were used, because of the too small volume when using 20 equiv.

The observation that **1b** containing a phthalazine moiety seems to be catalytically more active towards the monooxygenation of DHA than **1a** exhibiting a pyridazine unit can also be accounted by the fact that the former enables more delocalization of negative charge from the μ-oxo ligand onto the ligand backbone, rendering the Cu-O-Cu unit more electrophilic.

The proposed reaction mechanism for the general conversion of a hydrocarbon (RH) to the corresponding alcohol (ROH) via an O-insertion with participation of the bridging oxygen ligand of the **Cu_2O** complex and the regeneration of the latter species by oxygenation of the dicopper(I) complex is shown in the following figure.

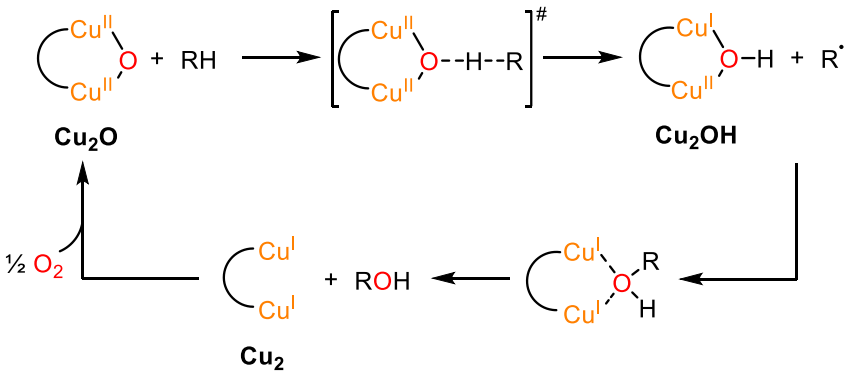

Scheme S7: Proposed reaction mechanism for the hydrocarbon-to-alcohol conversion. Starting from the **Cu_2O** complex and the hydrocarbon (RH), a transition state is proposed leading to the **Cu_2OH** complex. In the next step, the R radical binds to the mixed-valent **Cu_2OH** species and finally the alcohol (ROH) is released. The reaction can proceed again, when the dicopper(I) complex **Cu_2** is reacted with dioxygen.

This proposed reaction mechanism is known for zeolites like Cu-MOR as well.[48, 52] Starting from the **Cu_2O** complex and the hydrocarbon (RH), the approach of R-H leads to the polarization of the Cu-O-bond in the **Cu_2O** species, resulting in a Cu(I)-oxyl-Cu(II) radical, leading to the shown transition state (cf. Scheme S7). This happens, because an electron can be transferred from the oxygen p orbital to the singly-occupied d_{x2-y2} orbital of one copper(II) center and the following H-atom abstraction is enforced by the O-H-bond formation driving the reaction (BDFE of the **Cu_2OH** complex is estimated to be 111 kcal mol^{-1}, see above) leading to a radical and the mixed-valent mono-μ-hydroxo dicopper(I/II) complex. The schematic overlap of the d_{x2-y2} of the two copper centers and the 2p (p_x, p_y and p_z) orbitals of the bridging oxygen within the **Cu_2O** moiety is shown in the following figure (see Figure S44).

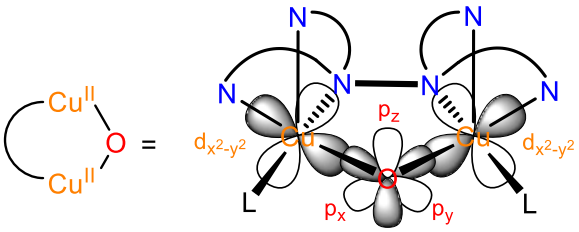

Figure S44: The simplified schematic structure of the **Cu_2O** moiety shows the involved orbitals, i.e., the d_{x2-y2} orbitals of the two copper centers which are the SOMOs (singly occupied molecular orbital(s)) and the three 2p orbitals (p_x, p_y and p_z) of the oxygen ligand representing the HOMOs (highest occupied molecular orbital(s)). With L = coordinating solvent molecule (C_3H_6O).

Finally, another electron is shifted from the p orbital of the bridging O-atom to the other copper(II) center and the R radical is bound, resulting in the formation of the alcohol (ROH) and the dicopper(I) complex **Cu_2**. The reaction can proceed again when dioxygen and RH are added. This kind of O-transfer reaction seems to be a smart way for the oxygenation of organic substrates (maybe no Cu-O-bond cleavage is involved during the proposed reaction sequence until the R radical is bound and product is released; but perhaps the bond between the Cu(I) and the Cu(II)-OH moiety is cleaved before the second step takes place).[53] Since the formed alcohols of the utilized organic substrates in this initial reactivity study are only the primary unstable oxygenation products, they are subsequently converted to the corresponding ketones or quinones (the case for DHA) which is also catalyzed by the **Cu_2O** species.

10.2. Dihydroanthracene

For the calibration we used different ratios of 9,10-dihydroantracene, anthracene and 9,10-anthraquinone with 2 mL of a 2 mM mesitylene solution in dichloromethane (DCM). In all cases 2 µL of the reaction mixtures were injected into the GC-MS.

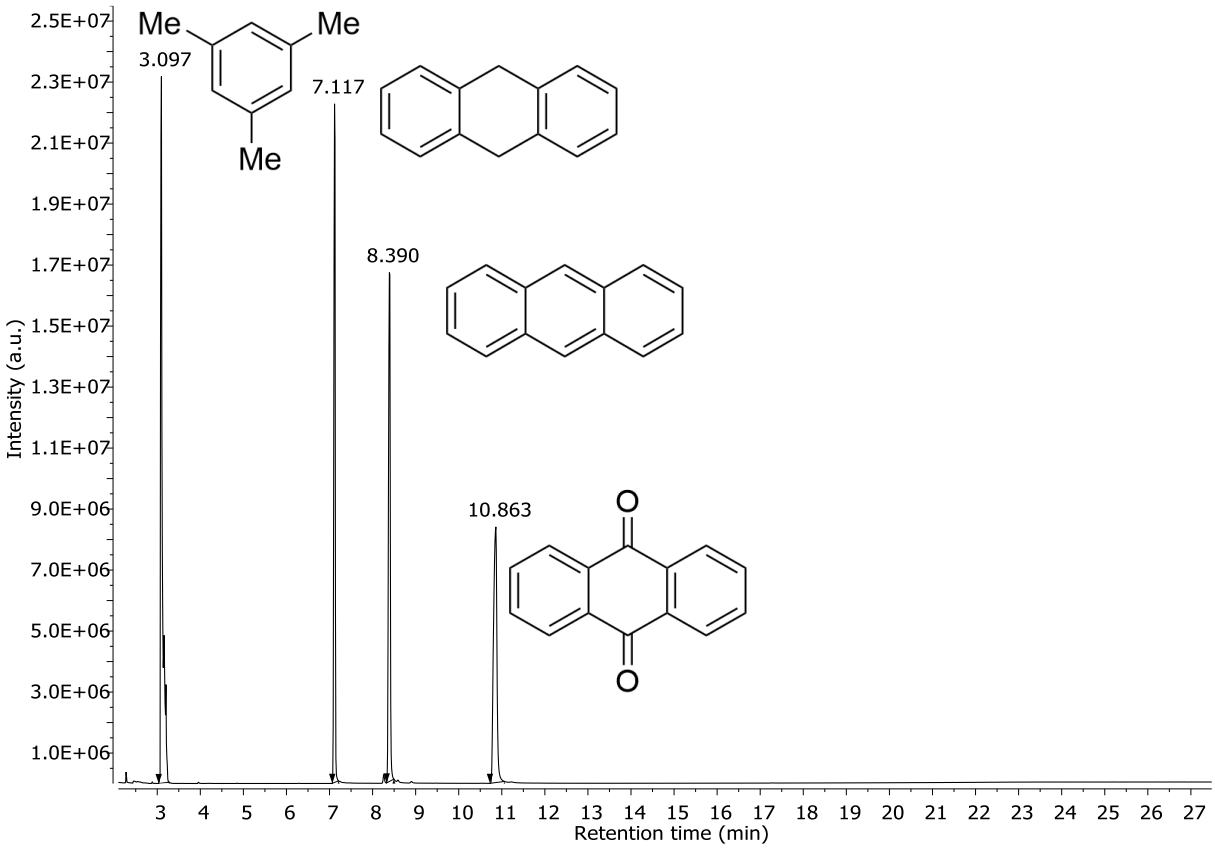

Figure S45: Chromatogram of the calibration for the reactivity towards dihydroanthracene.

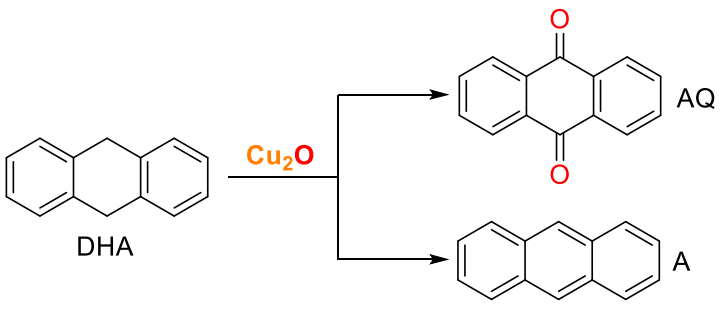

Scheme S8: Reactivity towards DHA leading to A and AQ.

Table S18: Overview of the obtained results for the reactivity towards DHA. 0.5 equiv. (stochiometric) or 10 equiv. (excess) of DHA were used.

System	DHA / %	A / %	AQ / %	TON[c]	TON[d]	Stoichiometric[d] / %
DHA+O_2	98	2	0	N.A.	N.A.	0
CuP-PF_6	94	3	3	N.A.	N.A.	3
CuP-OTf[a]	96	2	2	N.A.	N.A.	2
CuP-OTf	98	2	0	0	0	N.A.
CuP-PF_6	98	2	0	0	0	N.A.
1a-PF_6[b]	1	16	83	N.A.	N.A.	83
1a-OTf[b]	49	22	28	N.A.	N.A.	28
1a-PF_6[b]	68	14	17	2.8	3.4	N.A.
1a-OTf[a]	78	11	11	2.2	2.2	N.A.
1b-PF_6[b]	69	11	20	2.2	4.0	N.A.
1b-OTf[b]	69	6	24	1.2	4.8	N.A.
1b-PF_6[b]	39	14	47	N.A.	N.A.	47
1b-OTf[b]	50	8	41	N.A.	N.A.	41

General remarks: TON = Turnover Number; is defined as the equiv. of product made per equiv. of catalyst; 10 equiv. of DHA were used; representing 20-fold excess.
In some cases, anthrone could be detected as well but was not quantified; [a] significant amounts of anthrone were formed, [b] small amounts of anthrone were formed. [c] Product is anthracene. [d] Product is anthraquinone.

10.3. Reactivity of the $Cu_2{}^{18}O$ complex with DHA

To clearly demonstrate that the **Cu_2O** complexes are the source of the oxygen-atoms which are incorporated into the substrate, we performed reactivity experiments towards 9,10-dihydroanthracene with $^{18}O_2$ instead of $^{16}O_2$. Therefore, not only GC-MS was used, but also HR-EI mass spectrometry was employed. As a control experiment and to confirm the activity of our catalyst and to verify the used method (HR-EI MS), we performed the same experiment again with $^{16}O_2$. The identical three-step protocol was applied as described above (Section S2.8), except of the quenching step. To stop the reaction, the solvent was removed under reduced pressure, dissolved in dry dichloromethane, filtered (via a 0.45 µm syringe filter) and finally the solvent was again removed under reduced pressure. The obtained samples were stored under inert atmosphere (N_2) and measured in solid form or dissolved in dry dichloromethane and were directly injected.

Employing 0.5 equiv. of DHA (stoichiometric amount of DHA) resulted in the conversion to 9,10-anthraquinone. Figure S46 and Figure S47 show the characteristic cutouts of the HR-EI mass spectra obtained upon reaction of **2b**-OTf with DHA using $^{16}O_2$ or $^{18}O_2$ (top), respectively, and the corresponding simulated spectra (middle). The additional GC-MS spectra are shown at the bottom of each figure.

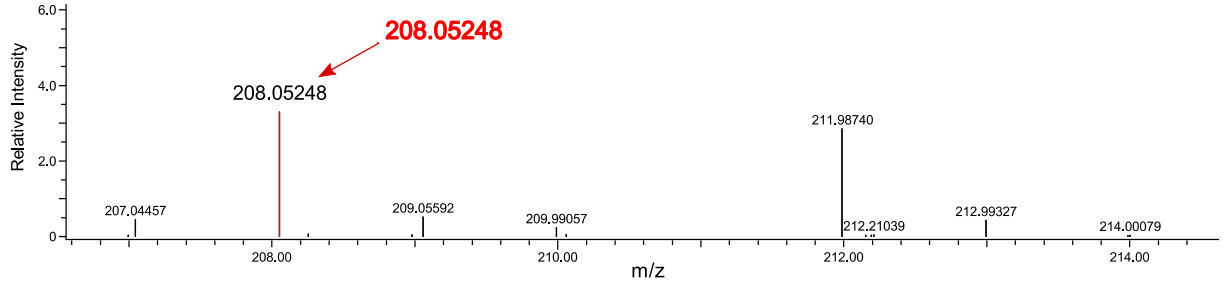

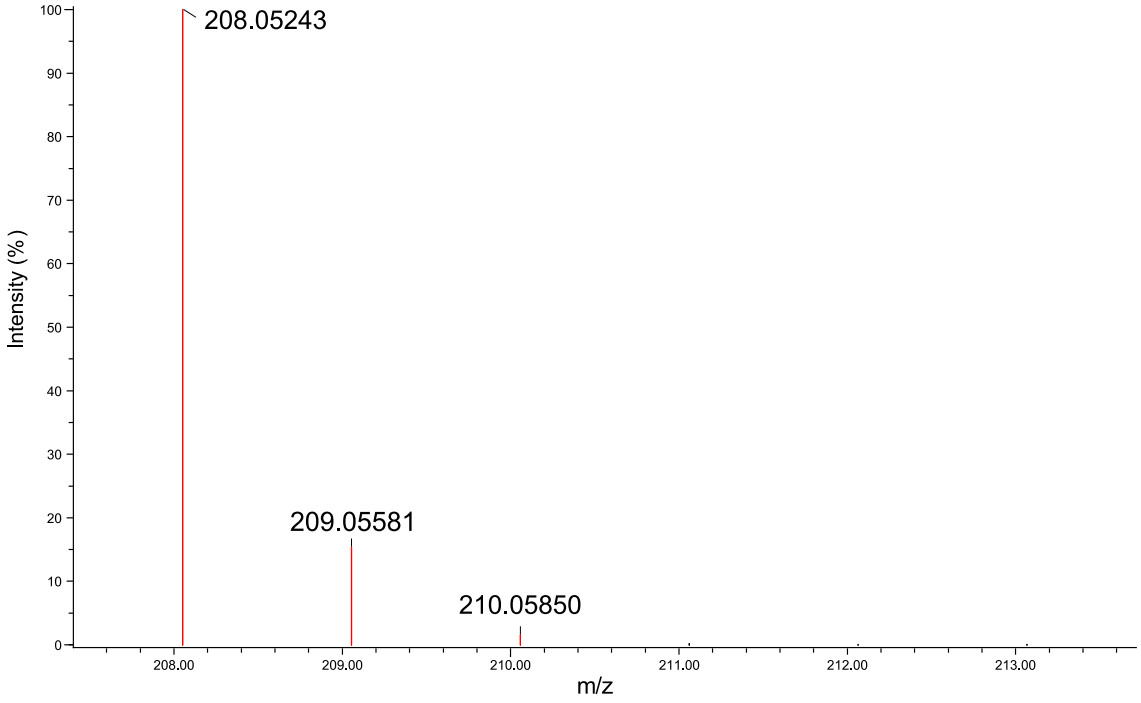

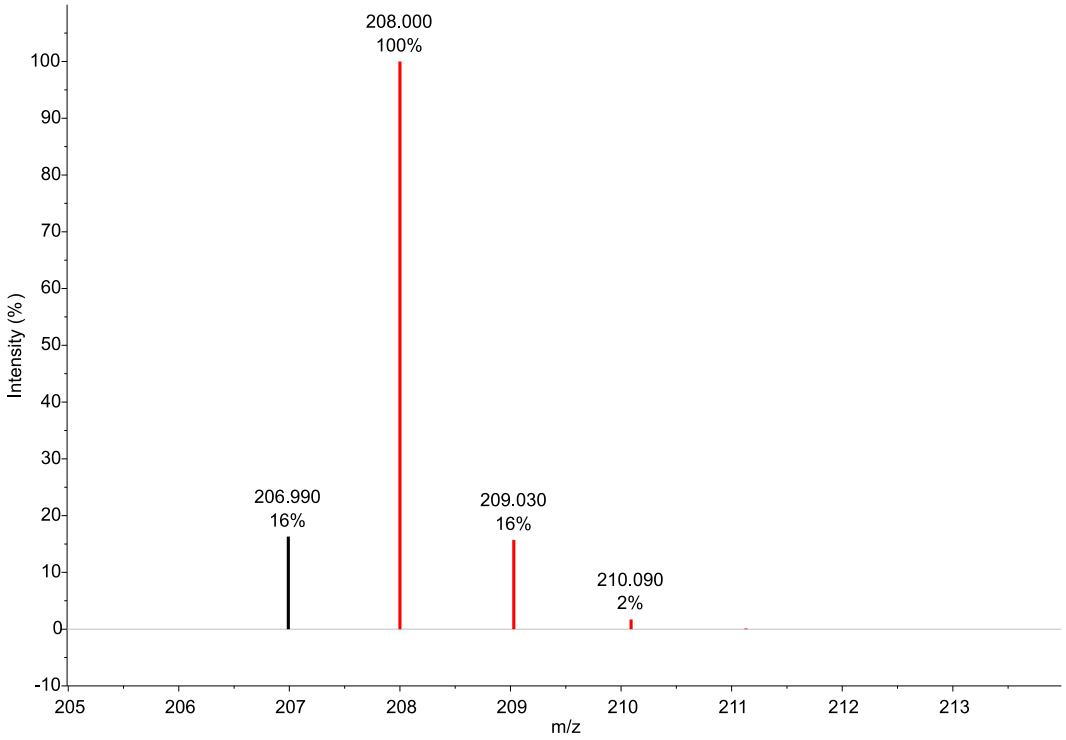

Figure S46: Characteristic cutout of the HR-EI and GC mass spectra of **1b**-OTf after reaction with dioxygen $^{16}O_2$ and addition of DHA **without aqueous workup**. **Top:** The isotopic pattern and corresponding *m/z* value of the HR-EI measurement fit for

AQ containing two ^{16}O-atoms (208.05248). Note: the peak at 211.9874 *m/z* is observed in every sample since it is a mass fragment of the used calibration standard (TCI, perfluorokerosene, C_nF_{2n+2}, P0689). **Middle:** Corresponding simulated spectrum for AQ containing two ^{16}O-atoms (cal. 208.05243). **Bottom:** The GC-MS measurement (red peaks) confirmed the observation made by HR-EI MS.

Upon reaction of an acetone solution of **1b**-OTf with $^{16}O_2$ and addition of DHA, the mass spectrum presented in Figure S45 is obtained, which shows a peak with an isotopic pattern and *m/z* value corresponding to AQ containing two ^{16}O-atoms of 208.05248 (calc. 208.05243 *m/z*; $[C_{14}H_8{}^{16}O_2]^{+\cdot}$ as positively charged mono-radical species), which is also proven by GC-MS (Figure S45, bottom). Upon reaction with $^{18}O_2$, the characteristic peak shifts by 4 mass units and the mass spectrum shown in Figure S46 resulted, which shows a peak with an isotopic pattern and *m/z* value of 212.06099 (calc. 212.06092 *m/z*; $[C_{14}H_8{}^{18}O_2]^{+\cdot}$ as positively charged mono-radical species) corresponding to AQ containing two ^{18}O-atoms. The obtained GC-MS spectrum confirms the HR-EI measurement, specifically the relative intensity of the product $^{18}O_2$-AQ is 100 %. The sample also contains $^{16}O_2$-AQ (14 % relative intensity) and $^{16}O^{18}O$-AQ (27 % relative intensity); maybe resulting from impurities in the bought $^{18}O_2$ and some traces of water in the used solvents for measurements.

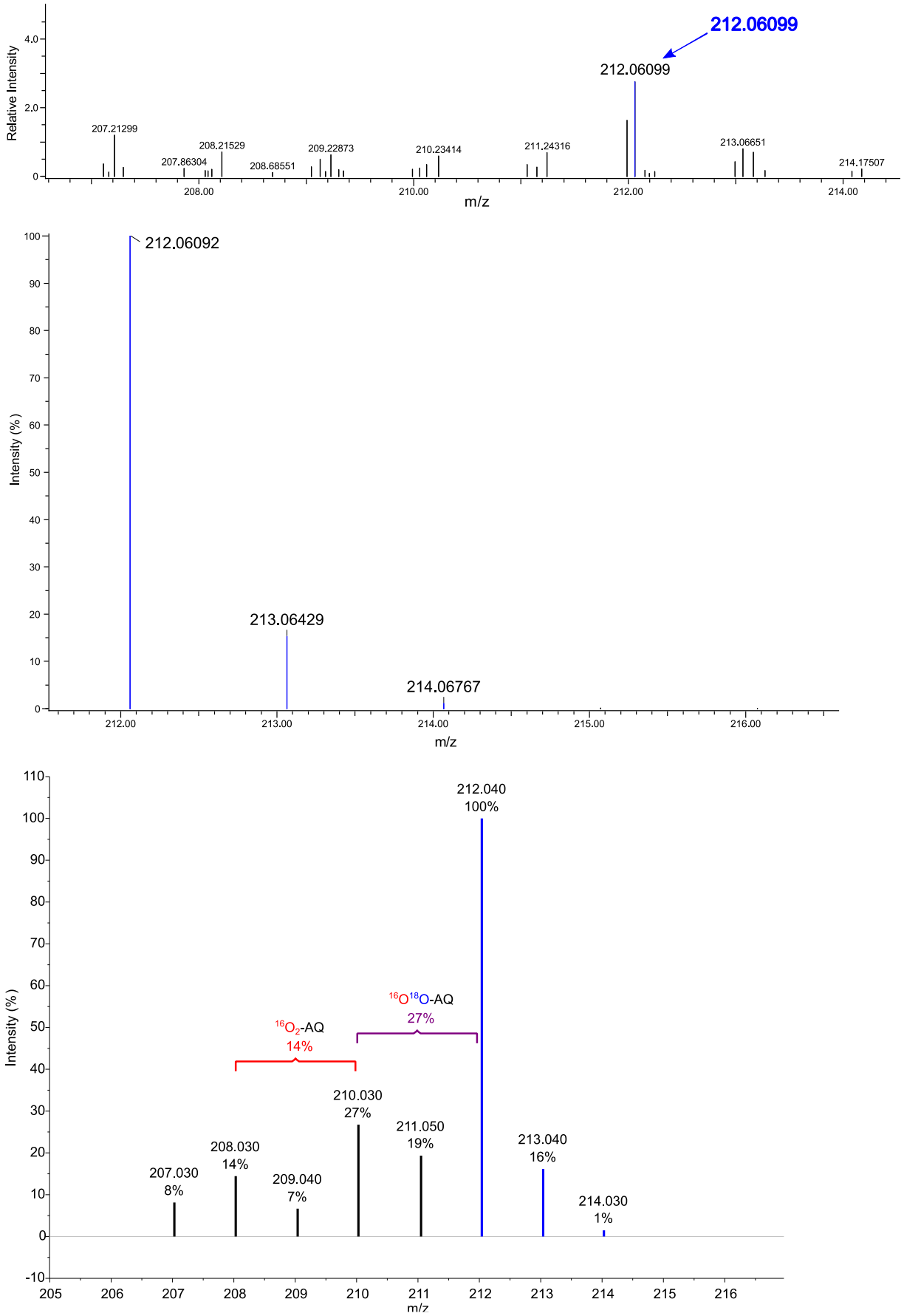

Figure S47: Characteristic cutout of the HR-EI and GC mass spectra of **1b**-OTf after reaction with dioxygen $^{18}O_2$ and addition of DHA **without aqueous workup**. **Top:** The isotopic pattern and corresponding *m/z* value of the HR-EI measurement fit for

AQ containing two ^{18}O-atoms (212.06099), confirming the source of the O-atoms in the product of the reactivity towards DHA. Note: the peak at 211.9874 *m/z* is observed in every sample since it is a mass fragment of the used calibration standard (TCI, perfluorokerosene, C_nF_{2n+2}, P0689). **Middle:** Corresponding simulated spectrum for AQ containing two ^{18}O-atoms (cal. 212.06092). **Bottom:** The GC-MS measurement (blue peaks) confirmed the observation made by HR-EI MS.

The replacement of the aqueous workup in the three-step protocol was the crucial step; if the quenching step in the reactivity protocol is performed with the $^{18}O_2$-sample in the typical way, just a product mixture of $^{16}O_2$-AQ (44 % relative intensity), $^{16}O^{18}O$-AQ (100 % relative intensity) and only a small amount of $^{18}O_2$-AQ (11 % relative intensity) could be detected as proven by HR-EI and GC-MS (Figure S48).

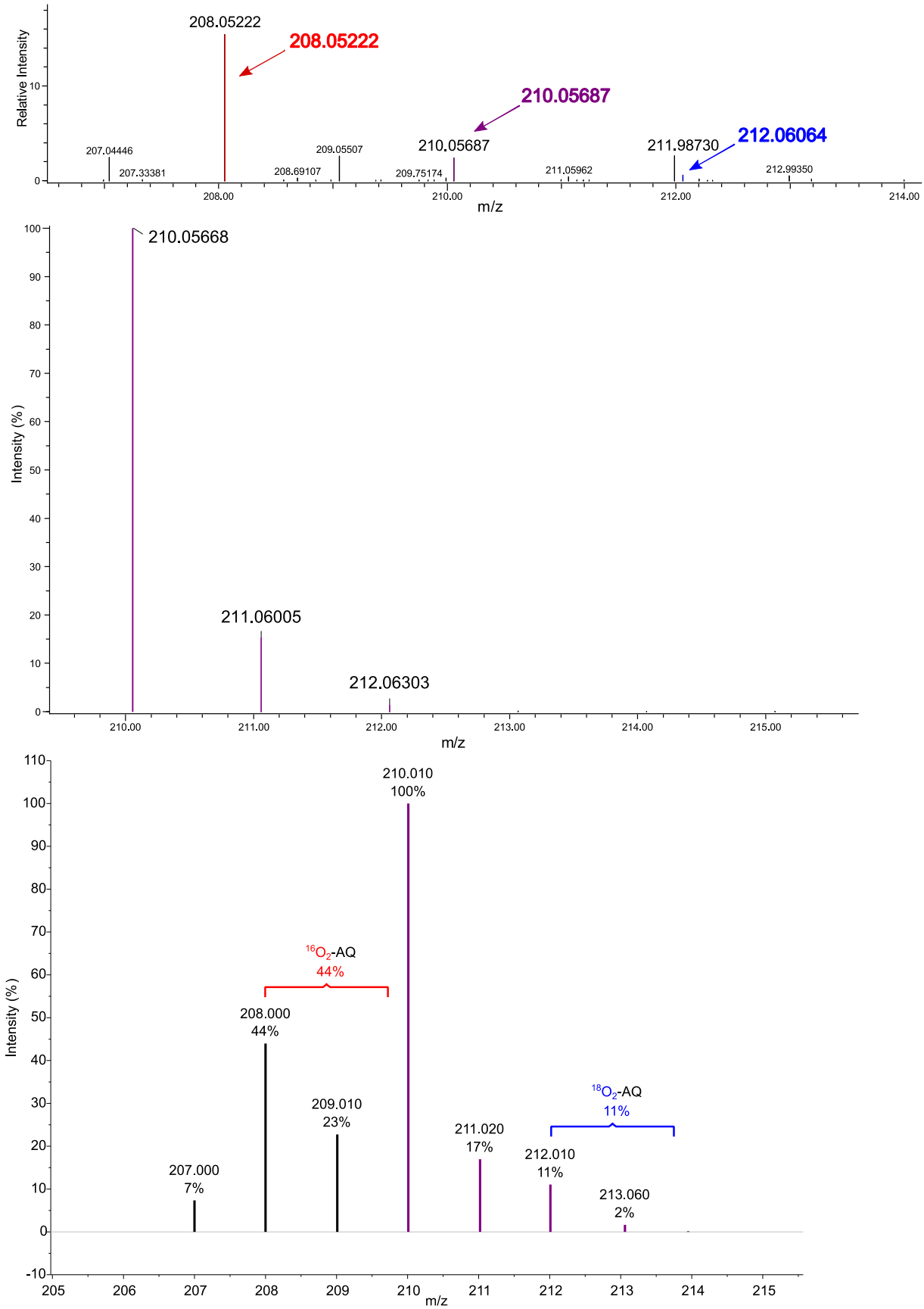

Figure S48: Characteristic cutout of the HR-EI and GC mass spectra of **1b**-OTf after reaction with dioxygen $^{18}O_2$ and addition of DHA **with aqueous workup**. **Top:** The isotopic pattern and corresponding *m/z* value of the HR-EI measurement fit for AQ containing two ^{16}O-atoms (208.05222), one ^{16}O- and one ^{18}O-atom (210.05687) and two ^{18}O-atoms (212.06064). Note: the peak at 211.9873 *m/z* is observed in every sample since it is a mass fragment of the used calibration standard (TCI,

perfluorokerosene, C_nF_{2n+2}, P0689). **Middle:** Corresponding simulated spectrum for AQ containing ^{16}O- and one ^{18}O-atom (cal. 210.05668). The simulated spectra for the other species are shown above. **Bottom:** The GC-MS measurement (violet peaks) confirmed the observation made by HR-EI MS.

This is the result of the formation of hydrates - one of the simplest addition reactions to the carbonyl group, specifically, the exchange of the ^{18}O-atoms of AQ caused by addition of $H_2{}^{16}O$ – followed by the formation of hydrate in an equilibrium reaction. The balance of this reaction is mostly shifted to the side of the ketone since Erlenmeyer's rule does not allow two alcohol functional groups at one carbon (except some stable hydrates, e.g., formaldehyde hydrate) resulting in the elimination of water (here: $H_2{}^{18}O$).[54, 55, 56] In our case, this strongly indicates that the ^{18}O-atoms of the $^{18}O_2$-AQ are exchanged by ^{16}O derived from the addition of water ($H_2{}^{16}O$) following equation (4) and (5).

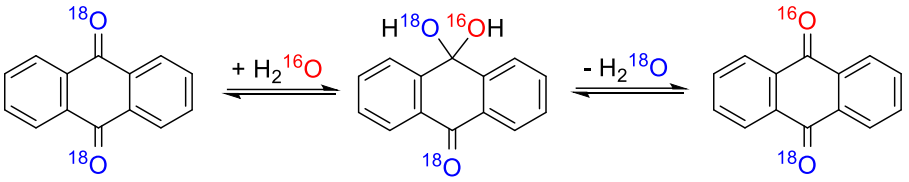

(4)

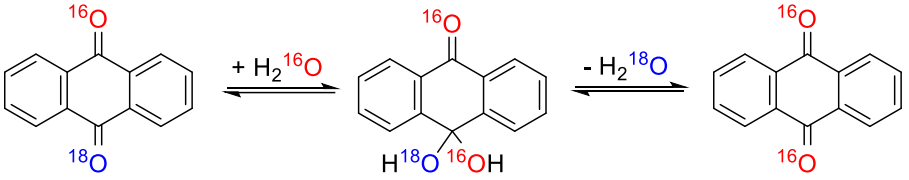

(5)

The hydration of aldehydes and ketones is a nucleophilic reaction which take place under neutral, acidic and basic conditions.[54] As a consequence, we optimized and modified our protocol in the above described manner and we were able to clearly demonstrate that both O-atoms in the AQ have their origin in the oxygen ($^{16}O_2$ or $^{18}O_2$) used to produce the active **$Cu_2{}^{16}O$** or **$Cu_2{}^{18}O$** catalyst which is able to transfer it to DHA to produce $^{16}O_2$-AQ or $^{18}O_2$-AQ, respectively (Figures S46 and S47). The obtained results are summarized in the following table (Table S19).

Table S19: Summary of the obtained results for reactivity towards DHA using $^{16}O_2$ or $^{18}O_2$ confirming that the oxygen atoms in AQ derive from dioxygen.

Reactivity	Formula	Calc. Mass	Mass	Δ / mDa	Δ / ppm	Intensity*
$^{16}O_2$	**$C_{14}H_8{}^{16}O_2$**	208.05243	208.05248	0.05	0.25	100 %
$^{18}O_2$	**$C_{14}H_8{}^{18}O_2$**	**212.06092**	**212.06099**	**0.07**	**0.32**	**100 %**
$^{18}O_2$ with aqueous workup ($H_2{}^{16}O$)	$C_{14}H_8{}^{16}O_2$	208.05243	208.05222	-0.21	-1.01	44 %
	$C_{14}H_8{}^{16}O{}^{18}O$	210.05668	210.05687	0.20	0.93	100 %
	$C_{14}H_8{}^{18}O_2$	212.06092	212.06064	-0.28	-1.34	11 %
* Quantification was done by use of GC-MS; cf. Figures S46, S47 and S48, Insets.						

Conclusively, the presented reactivity with $^{18}O_2$ clearly confirms that the O-atom of the reactive **Cu_2O** species is transferred to the substrate molecule after H-atom abstraction in the initial step leading to the disecondary alcohol as primary oxygenation product (cf. proposed scenario for the reactivity towards DHA in Scheme 3 of the main paper).

10.4. Reactivity of the Cu_2O complex with DHA under anaerobic conditions

To clearly demonstrate that the **Cu_2O** complexes are the source of the oxygen-atoms which are incorporated into the substrate, we performed reactivity experiments towards 9,10-dihydroanthracene under **anaerobic conditions** (under N_2 atmosphere). Moreover, we generated the **Cu_2O** complexes with **N_2O**. As a control experiment, we performed the same experiment again with **excess O_2** (conditions normally used, "standard/conventional" conditions, cf. Section S2.8 and see below).

Experimental setup. **Anaerobic (O_2/N_2):** The copper(I) precursor **1b**-OTf (2.14 mM, 2 eq.) was dissolved in dry acetone (15 mL) under an inert gas atmosphere. O_2 was added at -35 °C (238 K) via a cannula through the septum with a pressure slightly above 1 atm for a slow gas flow through the reaction vessel. Color change to green was observed after 30 seconds. To ensure quantitative formation of the **Cu_2O** complex the addition of O_2 was continued for 15 minutes. Then **O_2 was removed** by bubbling nitrogen through the reaction vessel for 15 minutes. Then the substrate (0.5 eq. DHA; stoichiometric amount) was added under N_2 atmosphere. The reaction mixture was stirred for 2 h at -35 °C. Then the reaction mixture was allowed to reach room temperature (298 K) within 3 h and was stirred at 298 K for additional 2 h under N_2. After treatment with a saturated solution of Na_2-EDTA (10 mL) the reaction was stopped and the organic phase was separated, the aqueous phase was extracted with dichloromethane (2x 15 mL), the combined organic phases were dried with sodium sulfate, filtered and solvents were removed under reduced pressure. The obtained samples were stored under inert atmosphere (N_2). Characterization of the obtained residues was done by means of GC mass spectrometric measurements. In addition, the same experiment was performed using the "standard/conventional" conditions (cf. Section S2.8) with excess dioxygen (1.09 mM, 1 eq. **1b**-OTf and 0.5 eq. DHA). In this case, extra dioxygen was added for 10 min after reaching room temperature. This sample is called **excess O_2 (O_2)**. The reaction time (2 h -35 °C, 3 h reaching room temperature and 2 h at room temperature) was the same in both cases.

Additionally, a third experiment was performed using **N_2O** instead of dioxygen. In this case, the "conventional/standard" conditions were employed using 2 eq. **1b**-OTf (2.12 mM) and 0.5 eq. DHA. The **Cu_2O** catalyst **2b**-OTf was formed by adding N_2O at 238 K via a cannula through the septum with a pressure slightly above 1 atm for a slow gas flow through the reaction vessel for 50 min. Then DHA was added and the reaction was stirred for 2 h at 238 K without bubbling, but under an N_2O/N_2 atmosphere. Then the solution was warmed up to room temperature. After 45 minutes, N_2O was added via the cannula for 10 minutes; then, the solution was stirred for another hour at room temperature under N_2O/N_2 atmosphere. This sample is called **N_2O**.

Result. In both cases (anaerobic conditions (O_2/N_2) and excess O_2 (O_2)) employing 0.5 equiv. of DHA resulted in the conversion to 9,10-anthraquinone (Table S20). Figure S49 shows the characteristic cutouts of the chromatogram obtained upon reaction of **2b**-OTf with DHA under **anaerobic conditions** (top), with **excess O_2** (middle) and with **N_2O** (bottom). Upon reaction of **2b**-OTf with DHA under anaerobic conditions, the chromatogram presented in Figure S49 (top) is obtained, which clearly shows that anthraquinone (AQ) was produced. Therefore, not the excess dioxygen (which is present in the control experiment: **excess O_2**, Figure S49, middle) is the reason for the observed OAT activity, but the presence of the **Cu_2O** complexes.

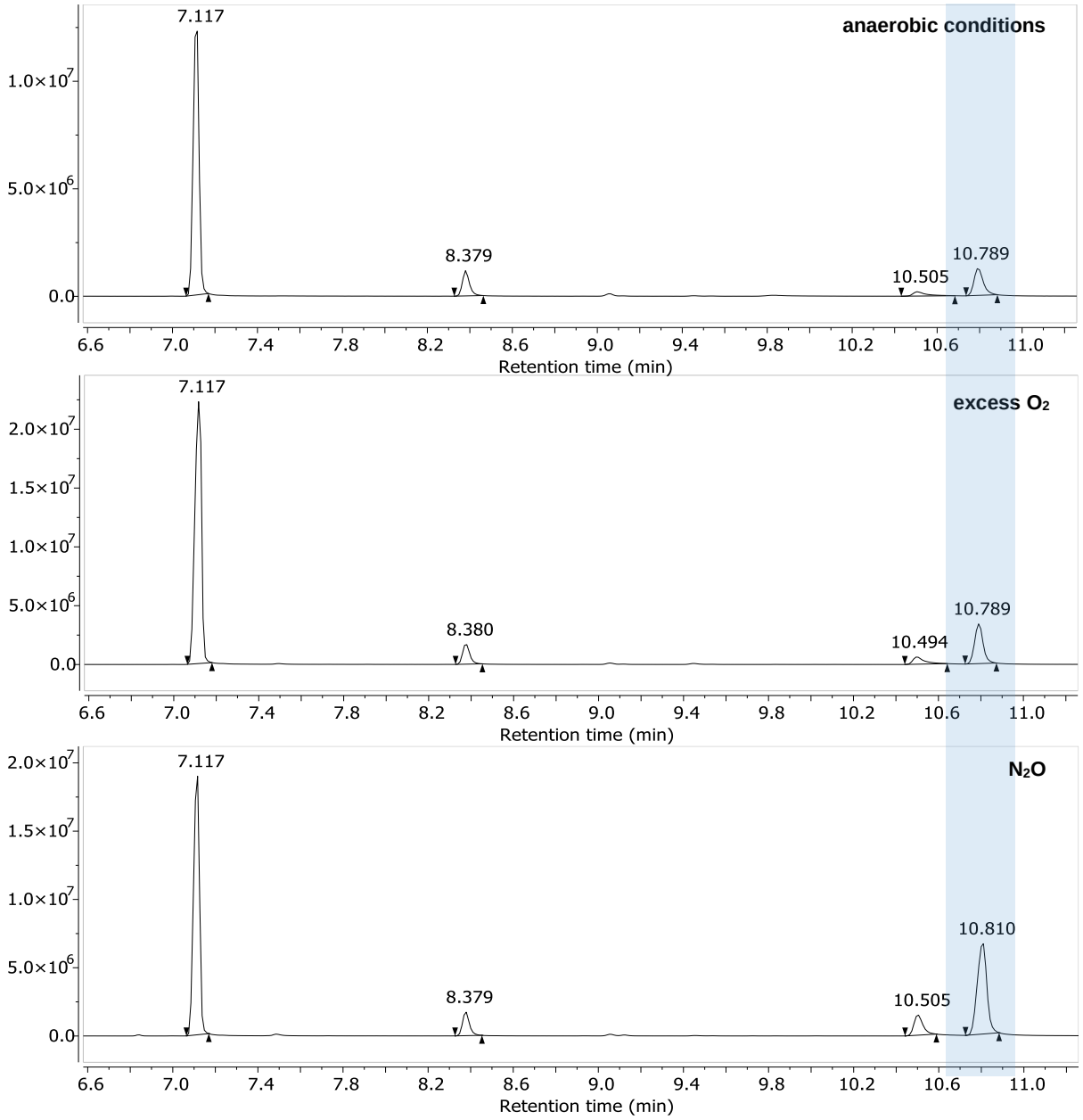

Figure S49: Top: Characteristic cutout of the chromatogram of **2b**-OTf after reaction with DHA under **anaerobic conditions**. **Middle:** Characteristic cutout of the chromatogram of **2b**-OTf after reaction with DHA under **excess of O_2** (conditions usually used and described in Section S2.8). **Bottom:** The retention times are as follows: DHA t_R = 7.12 min, A t_R = 8.38 min and AQ t_R = 10.8 min. Anthrone (t_R = 10.5 min) was also formed in significant amounts.

Importantly, this result is confirmed by using nitrous oxide as reagent to generate the **Cu_2O** catalyst. In this case, **no dioxygen is present during the whole experiment** and only the **Cu_2O** complex (**2b**-OTf) can react with the substrate to produce AQ (Figure S49, bottom). As detected by GC-MS, 57 % AQ was formed from DHA in this case. Again, based on the absence of O_2 in the oxygenation experiment, the oxygen contained in the AQ can only derive from the **Cu_2O** complex and not from O_2, supporting our findings.

Table S20: Overview of the obtained results for the reactivity towards DHA under anaerobic conditions and with excess O_2.

System	**DHA** (t_R = 7.12 min) **/ %**	**A** (t_R = 8.38 min) **/ %**	**AQ** (t_R = 10.8 min) **/ %**
1b-OTf, **anaerobic conditions**	62	11	**27**
1b-OTf, **excess O_2**	60	8	**32**
1b-OTf, **N_2O**	37	6	**57**
Remark: Significant amounts of anthrone were formed.			

The following UV/Vis spectra (Figure S50) show the decrease of the characteristic **Cu_2O** absorption feature (especially the absorption band at 630 nm) upon reaction of the **Cu_2O** complex (**2b**-OTf) under the reaction conditions (0.5 eq. DHA, 238 K to 298 K; **anaerobic conditions**).

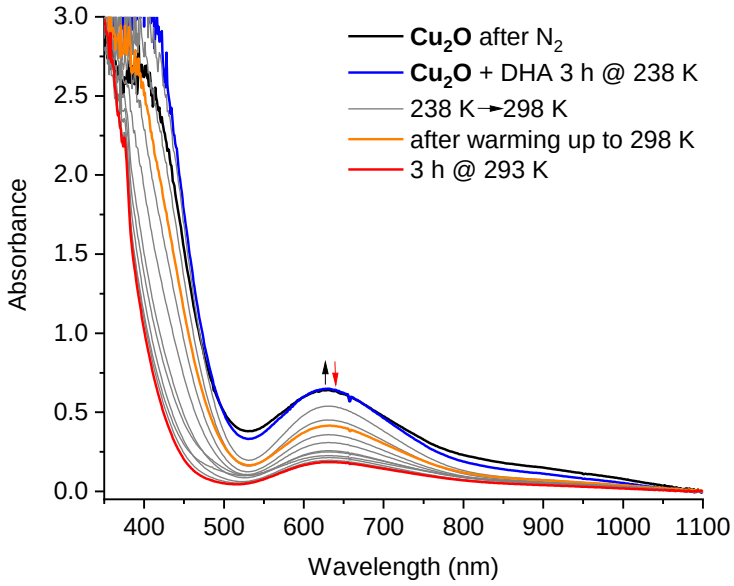

Figure S50: UV/Vis spectra of the reaction of **2b**-OTf with DHA under **anaerobic conditions**. Formation of the mono-μ-oxo species of **1b**-OTf after reaction with dioxygen and removal of excess O_2 (purging with N_2) resulted in the black spectrum (green solution with the characteristic absorption band at 630 nm). Addition of DHA under inert atmosphere (N_2) resulted in the blue spectrum after 3 h at 238 K. Warming up of the reaction mixture (**Cu_2O** species of **1b**-OTf = **2b**-OTf with DHA) under anaerobic conditions was monitored and resulted in the orange spectrum at 298 K. The red spectrum was obtained after 3 h at room temperature, showing a significant decrease of the intensity of the 630 nm band.

10.5. Xanthene

For the calibration we used different ratios of xanthene and xanthone with 2 mL of a 2 mM Mesitylene solution in DCM. In all cases 2 µL of the reaction mixtures were injected into the GC-MS.

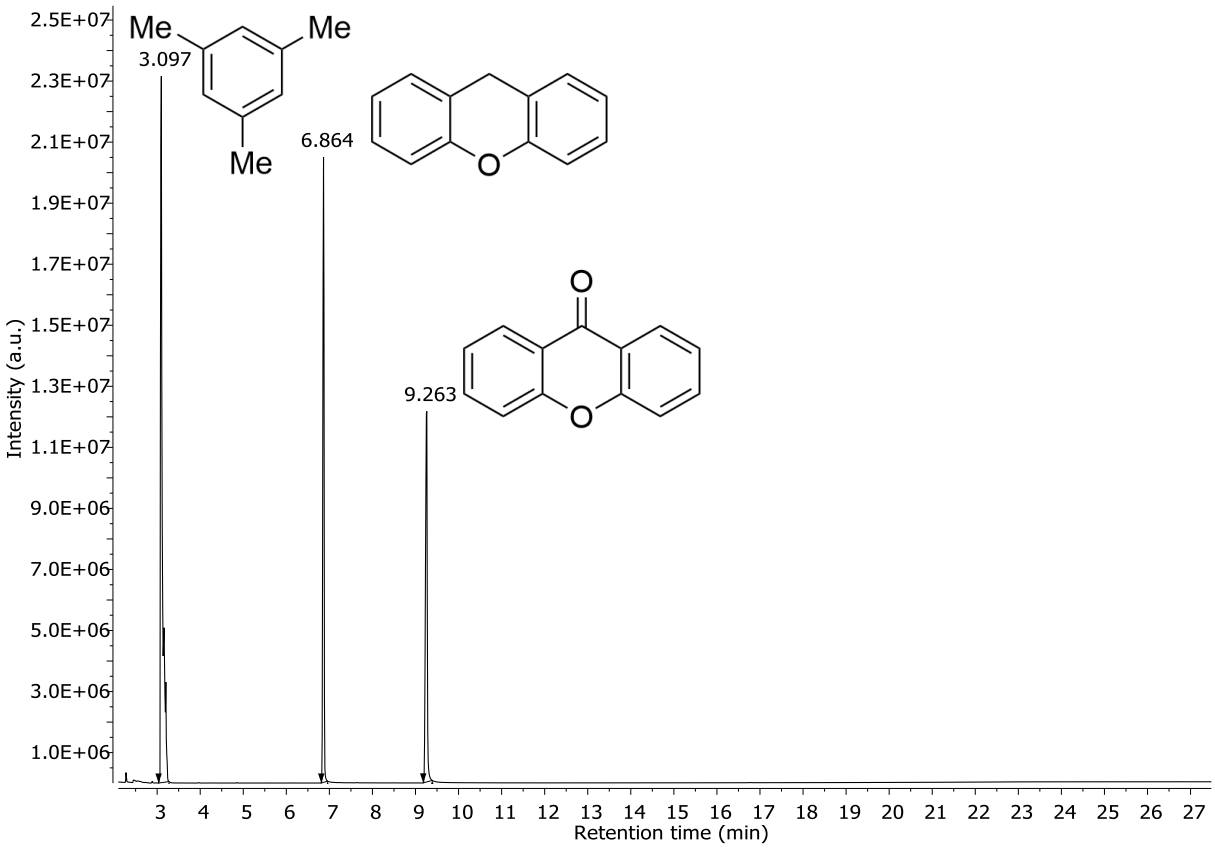

Figure S51: Chromatogram of the calibration for the reactivity towards xanthene.

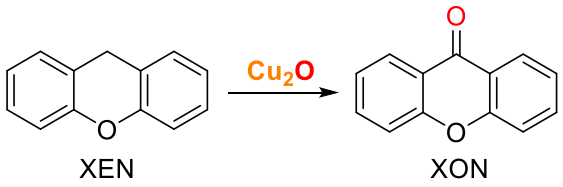

Scheme S9: Reactivity towards xanthene.

Table S21: Overview of the obtained results for the reactivity towards xanthene. 20 equiv. (excess) of XEN were used.

System	XEN / %	XON / %	TON
CuP-OTf	97	3	0.6
CuP-PF_6	96	4	0.8
1a-OTf	87	13	2.6
1a-PF_6	93	7	1.4
1b-PF_6	89	11	2.2
1b-OTf	89	11	2.2
TON = Turnover Number; is defined as the equiv. of product made per equiv. of catalyst; 20 equiv. of xanthene were used.			

10.6. Fluorene

For the calibration we used different ratios of fluorene and fluorenone with 2 mL of a 2 mM mesitylene solution in DCM. In all cases 2 µL of the reaction mixtures were injected into the GC-MS. Fluorene had a low amount of diphenylmethane inside.

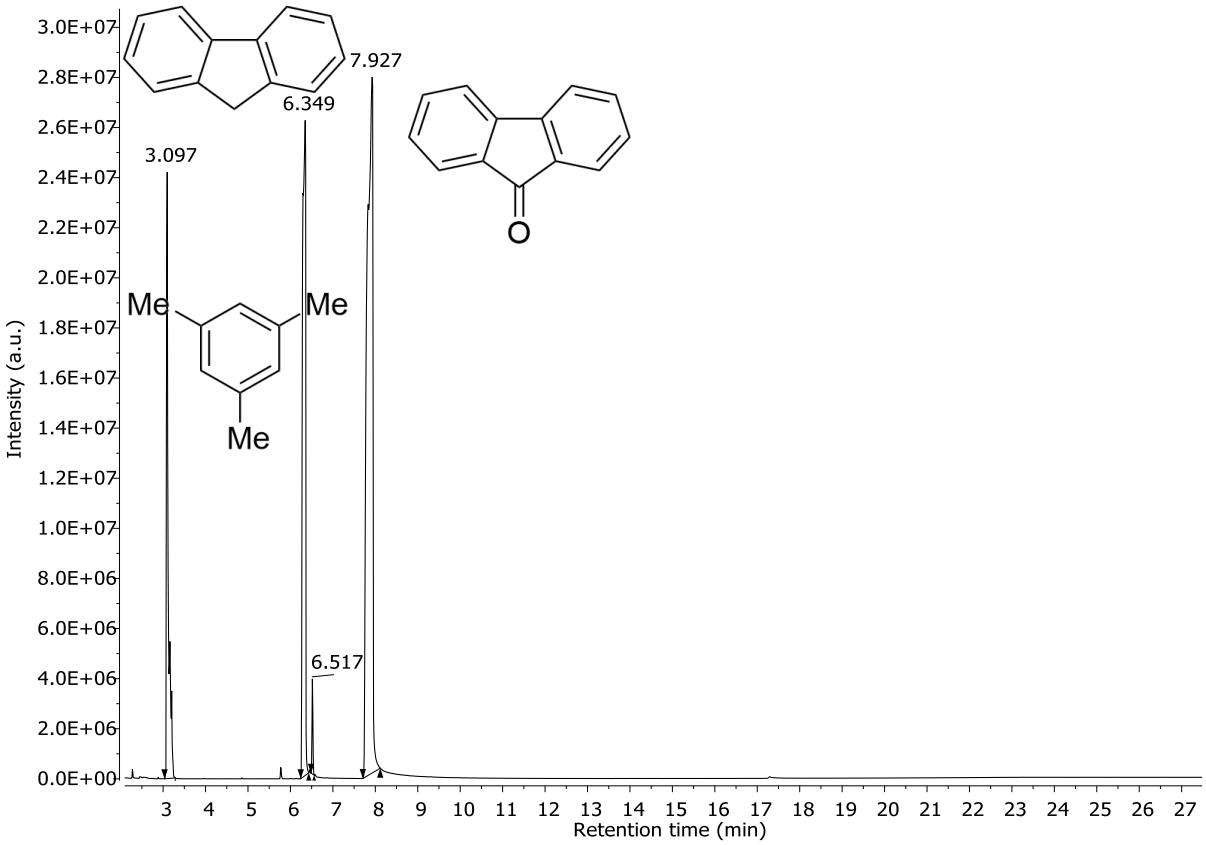

Figure S52: Chromatogram of the calibration for the reactivity towards fluorene.

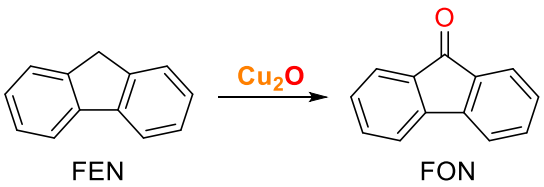

Scheme S10: Reactivity towards fluorene.

Table S22: Overview of the obtained results for the reactivity towards fluorene. 20 equiv. (excess) of FEN were used.

System	FEN / %	FON / %	TON
CuP-OTf	100	0	0
CuP-PF_6	100	0	0
1a-OTf	97	3	0.6
1a-PF_6	97	3	0.6
1b-PF_6	99	1	0.2
1b-OTf	95	5	1
TON = Turnover Number; is defined as the equiv. of product made per equiv. of catalyst; 20 equiv. of fluorene were used.			

10.7. Triphenylmethane

No reaction was observed upon addition of triphenylmethane (81 kcal mol^{-1}) to the **Cu_2O** complexes of **1a** and **1b**, suggesting that the BDE limit of our catalysts has been reached. Alternatively, the lack of conversion of triphenylmethane could also be due to steric reasons.[57, 58] In order to decide this question, the less sterically demanding substrate diphenylmethane was employed (see below).

10.8. Diphenylmethane

For the calibration we used different ratios of diphenylmethane and benzophenone with 2 mL of a 2 mM mesitylene solution in DCM. In all cases 2 µL of the reaction mixtures were injected into the GC-MS.

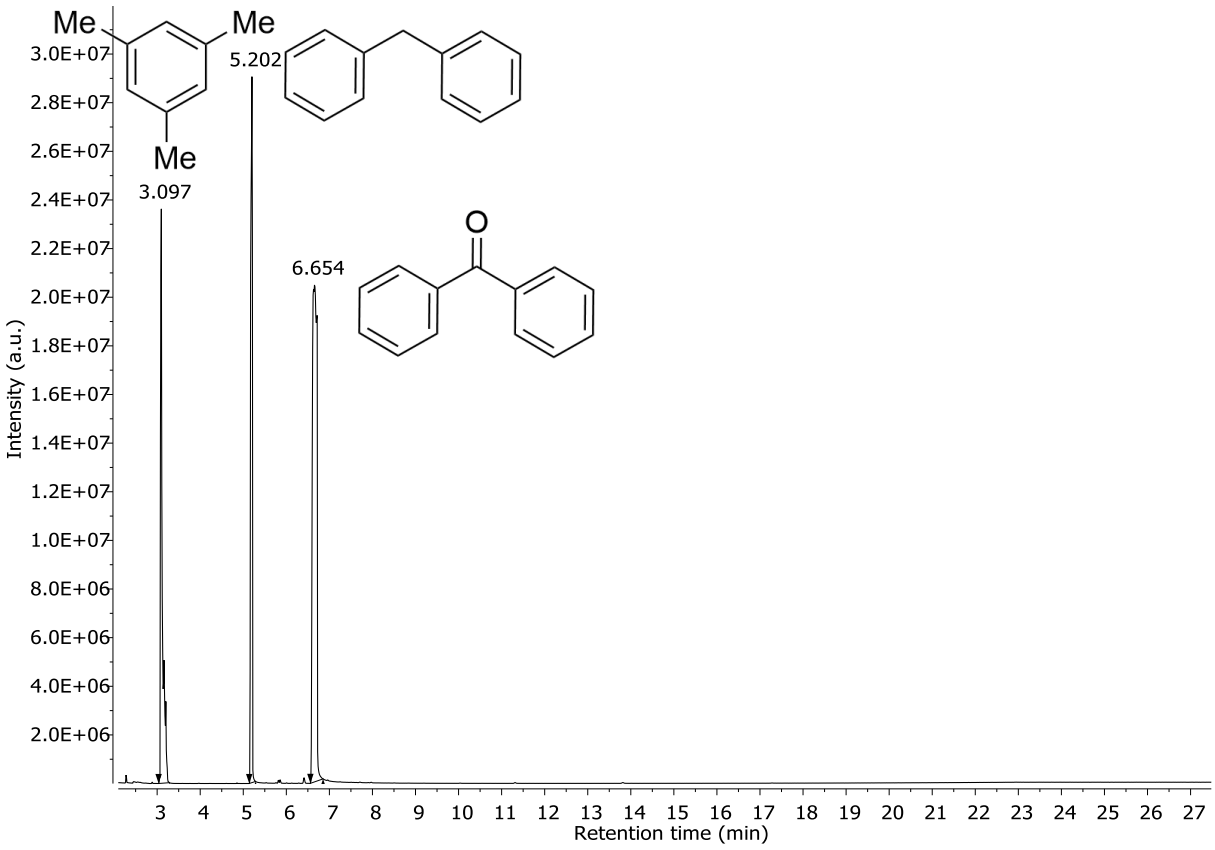

Figure S53: Chromatogram of the calibration for the reactivity towards DPM.

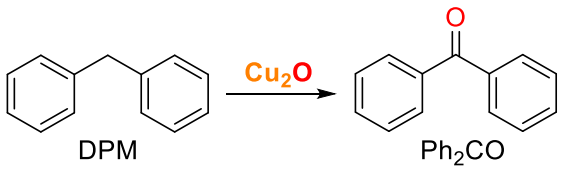

Scheme S11: Reactivity towards diphenylmethane.

Table S23: Overview of the obtained results for the reactivity towards diphenylmethane. 50 equiv. (excess) of DPM were used.

System	DPM / %	Ph_2CO / %	TON
CuP-OTf	100	0	0
CuP-PF_6	100	0	0
1a-OTf	97	3	1.5
1a-PF_6	97	3	1.5
1b-OTf	97	3	1.5
1b-PF_6	96	4	2.0
TON = Turnover Number; is defined as the equiv. of product made per equiv. of catalyst; 50 equiv. of diphenylmethane were used.			

11. Appendix

11.1. Data Availability

All data supporting the findings of this study are available within this article (main paper) and its Supporting Information or are available from the corresponding authors (M. R. or F. T.) upon reasonable requests. Crystallographic data for the structures reported in this article have been deposited at the Cambridge Crystallographic Data Centre, under the following deposition numbers: CCDC-1998203 (**compound 1**) and CCDC-1998204 (**compound 2**), and can be obtained free of charge via http://www.ccdc.cam.ac.uk/data_request/cif.

11.2. Supplementary Video

The **Supplementary Video 1** demonstrates the formation of the **Cu_2O** species with N_2O accompanied by N_2 evolution.

11.3. Author Contributions

F. T. and R. J. planned and executed the synthesis, characterization and reactivity studies. B. M. F. performed the (TD)DFT calculations. Cryo-UHR-ESI mass spectrometry was performed by L. S. and supervised by I. I.-B. The GC-MS measurements were done by J. H. Resonance Raman and XAS measurements were performed by B. G.-L., R. J., M. T. and S. B. and supervised by M. R. The analysis of the XAS data were done by B. G.-L. and M. R. All authors commented on the manuscript. F. T. and R. J. conceived the study and wrote the manuscript together with B. G.-L. and M. R.

References

[1] G. M. Sheldrick, *Acta Cryst. Sect. A: Found. Adv.* **2008**, *64*, 112-122.

[2] G. M. Sheldrick, *Acta Crystallogr. Sec. C: Struct. Chem.* **2015**, ***71***, 3-8.

[3] X-AREA Ver. 1.44, Programm Package for Single Crystal Measurements, STOE & CIE GmbH, Darmstadt, Germany **2008**.

[4] B. Schulz, J. Bäckström, D. Budelmann, R. Maeser, M. Rübhausen, M. V. Klein, E. Schoeffel, A. Mihill and S. Yoon, *Rev. Sci. Instrum.* **2005**, *76*, 073107.

[5] B. Grimm-Lebsanft, C. Brett, F. Strassl, D. Rukser, M. Biednov, F. Biebl, M. Naumova, A. Hoffmann, L. Akinsinde, D. Brueckner, S. Herres-Pawlis, M. Rübhausen, *Inorg. Chim. Acta* **2018**, *481*, 176-180.

[6] E. Welter, R. Chernikov, M. Herrmann, R. Nemausat, *AIP Conference Proceedings* **2019**, *2054*, 040002.

[7] B. Ravel, M. Newville, *J. Synchrotron Rad.* **2005**, *12*, 537-541.

[8] (a) F. Neese, *Wiley Interdisciplinary Reviews: Computational Molecular Science* **2012**, *2*, 73-78. (b) F. Neese, *Wiley Interdisciplinary Reviews: Computational Molecular Science* **2018**, *8*, e1327.

[9] J. P. Perdew, K. Burke, M. Ernzerhof, *Phys. Rev. Lett.* **1996**, *77*, 3865-68.

[10] F. Weigend, R. Ahlrichs, *Phys. Chem. Chem. Phys.* **2005**, *7*, 3297-3305.

[11] (a) S. Grimme, S. Ehrlich, L. Goerigk, *J. Comput. Chem.* **2011**, *32*, 1456-1465. (b) S. Grimme, J. Antony, S. Ehrlich, H. Krieg, *J. Chem. Phys.* **2010**, *132*, 154104-1-154104-19.

[12] (a) K. Eichkorn, H. Treutler, H. Öhm, M. Häser, R. Ahlrichs, *Chem. Phys. Lett.* **1995**, *240*, 283-290. (b) K. Eichkorn, F. Weigend, O. Treutler, R. Ahlrichs, *Theor. Chem. Acc.* **1997**, *97*, 119-124. c) F. Neese, *J. Comput. Chem.* **2003**, *24*, 1740-1747.

[13] F. Weigend, *Phys. Chem. Chem. Phys.* **2006**, *8*, 1057-1065.

[14] A. D. Becke, *J. Chem. Phys.* **1993**, *98*, 5648-5652.

[15] V. Barone, M. Cossi, *J. Phys. Chem. A* **1998**, *102*, 1995-2001.

[16] F. Neese, F. Wennmohs, A. Hansen, U. Becker, *Chem. Phys.* **2009**, *356*, 98-109.

[17] M. Itoh, K.-I. Motoda, K. Shindo, T. Kamiusuki, H. Sakiyama, N. Matsumoto, H. Okawa, *J. Chem. Soc. Dalton Trans.* **1995**, 3635-3641.

[18] J. Manzur, A. M. García, R. Letelier, E. Spodine, O. Peña, D. Grandjean, M. M. Olmstead, B. C. Noll, *J. Chem. Soc., Dalton Trans.* **1993**, 905-911.

[19] A. M Barrios, S. J. Lippard, *J. Am Chem. Soc.* **1999**, *121*, 11751-11757.

[20] J. Kuzelka, S. Mukhopadhyay, B. Spingler, S. J. Lippard, *Inorg. Chem.* **2004**, *43*, 1751-1761.

[21] G. Dyker, O. Muth, *Eur. J. Org. Chem*. **2004**, 4319-4322.

[22] C.-Y. Huang, A. G. Doyle, *J. Am. Chem. Soc.* **2012**, *134*, 9541-9544.

[23] M. Yoosefian, *Appl. Surf. Sci*. 2017, *392*, 225-230.

[24] W. B. Tolman, *Angew. Chem. Int. Ed*. **2010**, *49*, 1018-1024.

[25] W. C. Trogler, *Coord. Chem. Rev.* **1999**, *187*, 303-327.

[26] J. S. Woertink, P. J. Smeets, M. H. Groothaert, M. A. Vance, B. F. Sels, R. A. Schoonheydt, E. I. Solomon, *Proc. Natl. Acad. Sci. USA* **2009**, *106*, 18908-18913.

[27] M. H. Groothaert, P. J. Smeets, B. F. Sels, P. A. Jacobs, R. A. Schoonheydt, *J. Am. Chem. Soc.* **2005**, *127*, 1394-1395.

[28] P. Haack, C. Limberg, K. Ray, B. Braun, U. Kuhlmann, P. Hildebrandt, C. Herwig, *Inorg. Chem.* **2011**, *50*, 2133-2142.

[29] P. Haack, A. Kärgel, C. Greco, J. Dokic, B. Braun, F. F. Pfaff, S. Mebs, K. Ray, C. Limberg, *J. Am. Chem. Soc.* **2013**, *135*, 16148-16160.

[30] G. Davies, M. A. El-Sayed, *Inorg. Chem.* **1983**, *22*, 1257-1266.

[31] M. R. Churchill, G. Davies, M. A. El-Sayed, J. P. Hutchinson, M. W. Rupich, *Inorg. Chem.* **1982**, *21*, 995-1001.

[32] M. R. Churchill, G. Davies, M. A. El-Sayed, J. A. Fournier, J. P. Hutchinson, J. A. Zubieta, *Inorg. Chem.* **1984**, *23*, 783-787.

[33] M. A. El-Sayed, A. El-Toukhy, G. Davies, *Inorg. Chem.* **1985**, *24*, 3387-3390.

[34] G. Davies, M. A. El-Sayed, M. Henary, *Inorg. Chem.* **1987**, *26*, 3266-3272.

[35] H. O. Obias, Y. Lin, N. N. Murthy, E. Pidcock, E. I. Solomon, M. Ralle, N. J. Blackburn, Y.-M. Neuhold, A. D. Zuberbühler, K. D. Karlin, *J. Am. Chem. Soc.* **1998**, *120*, 12960-12961.

[36] N. Kitajima, T. Koda, Y. Moro-oka, *Chem. Lett*. **1988**, *17*, 347-350.

[37] J. Reim, B. Krebs, *Angew. Chem. Int. Ed.* **1994**, *33*, 1969-1971.

[38] J. Reim, R. Werner, W. Haase, B. Krebs, *Chem. Eur. J.* **1998**, *4*, 289-298.

[39] F. Meyer, H. Pritzkow, *Angew. Chem. Int. Ed.* **2000**, *39*, 2112-2115.

[40] W. Micklitz, S. G. Bott, J. G. Bentsen, S. J. Lippard, *J. Am. Chem. Soc*. **1989**, *111*, 372-374.

[41] J. Ling, L. P. Nestor, R. S. Czernuszewicz, T. G. Spiro, R. Fraczkiewicz, K. D. Sharma, T. M. Loehr, J. Sanders-Loehr, *J. Am. Chem. Soc.* **1994**, *116*, 7682-7691.

[42] A. Picchiotti, V. I. Prokhorenko, R. J. D. Miller, *Rev. Sci. Instrum.* **2015**, *86*, 093105.

[43] P. Vanelderen, R. G. Hadt, P. J. Smeets, E. I. Solomon, R. A. Schoonheydt, B. F. Sels, *J. Catal*. **2011**, *284*, 157-164.

[44] C. E. Elwell, N. L. Gagnon, B. D. Neisen, D. Dhar, A. D. Spaeth, G. M. Yee, W. B. Tolman, *Chem. Rev*. **2017**, *117*, 2059-2107.

[45] L. M. Mirica, O. X, T. D. P. Stack, *Chem. Rev*. **2004**, *104*, 1013-1045.

[46] a) K. D. Karlin, R. W. Cruse, Y. Gultneh, *J. Chem. Soc., Chem.Commun*.**1987**, 599-600. b) K. D. Karlin, P. Ghosh, R. W. Cruse, A. Farooq, Y. Gultneh, R. R. Jacobson, N. J. Blackburn, R. W. Strange, J. Zubieta, *J. Am. Chem. Soc*.**1988**,*110*, 6769-6780. c) I. Sanyal, M. Mahrooftahir, M. S. Nasir, P. Ghosh, B. I. Cohen, Y. Gultneh, R. W. Cruse, A. Farooq, K. D. Karlin, S. C. Liu, J. Zubieta, *Inorg. Chem*. **1992**, *31*, 4322-4332.

[47] a) K. E. Dalle, T. Gruene, S. Dechert, S. Demeshko, F. Meyer, *J. Am. Chem. Soc*. **2014**, *136*, 7428-7434. b) N. Kindermann, S. Dechert, S. Demeshko, F. Meyer, *J. Am. Chem. Soc*. **2015**,*137*, 8002-8005.

[48] C. Limberg, P. Haack, *Angew. Chem. Int. Ed.* **2014**, *53*, 4282-4293.

[49] S. H. Strauss, *Chem. Rev.* **1993**, *93*, 927-942.

[50] W. Meyer-Klaucke, W. Gnida, G. Henkel, G. X-Ray Absorption Spectroscopy in Biology. Reference Module in Chemistry, Molecular Sciences and Chemical Engineering, **2014**, Elsevier, pp. 1-27. https://doi.org/10.1016/B978-0-12-409547-2.10774-7.

[51] J. J.Warren, T. A. Tronic, J. M. Mayer, *Chem. Rev.* **2010**, *110*, 6961-7001.

[52] J. Xu, B. Liu, *J. Phys. Chem. C* **2019**, *123*, 10356-10366.

[53] J.-F. Wu, X.-D. Gao, L.-M. Wu, W. D. Wang, S.-M. Yu, S. Bai, *ACS Catal.* **2019**, *9*, 8677-8681.

[54] S. H. Hilal, L. L. Bornander, L. A. Carreira, *QSAR Comb. Sci.* **2005**, *24*, 631-638.

[55] M. Byrn, M. Calvin, *J. Am. Chem. Soc.* **1966**, *88*, 1916-1922.

[56] H. Morishita, H. Tamiaki, *Bioorg. Med. Chem.* **2003**, *11*, 4049-4057.

[57] R. N. Nasirov, S. P. Solodovnikov, *Russ. Chem. Bull.* **1972**, *21*, 2047-2048.

[58] A. Streitwieser, E. Ciuffarin, J. H. Hammons, *J. Am. Chem. Soc.* **1967**, *89*, 63-67.